INFORMATION TO USERS

This manuscript has been reproduced from the microfilm master. UMI films the text directly from the original or copy submitted. Thus, some thesis and dissertation copies are in typewriter face, while others may be from any type of computer printer.

The quality of this reproduction is dependent upon the quality of the copy submitted. Broken or indistinct print, colored or poor quality illustrations and photographs, print bleedthrough, substandard margins, and improper alignment can adversely affect reproduction.

In the unlikely event that the author did not send UMI a complete manuscript and there are missing pages, these will be noted. Also, if unauthorized copyright material had to be removed, a note will indicate the deletion.

Oversize materials (e.g., maps, drawings, charts) are reproduced by sectioning the original, beginning at the upper left-hand corner and continuing from left to right in equal sections with small overlaps. Each original is also photographed in one exposure and is included in reduced form at the back of the book.

Photographs included in the original manuscript have been reproduced xerographically in this copy. Higher quality 6" x 9" black and white photographic prints are available for any photographs or illustrations appearing in this copy for an additional charge. Contact UMI directly to order.

UMI

A Bell & Howell Information Company
300 North Zeeb Road, Ann Arbor MI 48106-1346 USA
313/761-4700 800/521-0600

AN ^{57}Fe MÖSSBAUER SPECTROSCOPY STUDY OF THE EFFECTS OF DIFFERENT EQUILIBRATION TEMPERATURES AND OXYGEN FUGACITY BUFFERS ON THE Fe^{2+} AND Fe^{3+} SITE POPULATIONS IN SYNTHETIC ANNITE MICA

By

Patrick H. J. Mercier

A thesis submitted to
the School of Graduate Studies and Research
in partial fulfillment of the requirements
for the degree of Master of Science

Department of Physics

University of Ottawa
Ottawa, Ontario
12 April 1996

National Library
of Canada

Acquisitions and
Bibliographic Services

395 Wellington Street
Ottawa ON K1A 0N4
Canada

Bibliothèque nationale
du Canada

Acquisitions et
services bibliographiques

395, rue Wellington
Ottawa ON K1A 0N4
Canada

Your file Votre référence

Our file Notre référence

The author has granted a non-exclusive licence allowing the National Library of Canada to reproduce, loan, distribute or sell copies of his/her thesis by any means and in any form or format, making this thesis available to interested persons.

The author retains ownership of the copyright in his/her thesis. Neither the thesis nor substantial extracts from it may be printed or otherwise reproduced with the author's permission.

L'auteur a accordé une licence non exclusive permettant à la Bibliothèque nationale du Canada de reproduire, prêter, distribuer ou vendre des copies de sa thèse de quelque manière et sous quelque forme que ce soit pour mettre des exemplaires de cette thèse à la disposition des personnes intéressées.

L'auteur conserve la propriété du droit d'auteur qui protège sa thèse. Ni la thèse ni des extraits substantiels de celle-ci ne doivent être imprimés ou autrement reproduits sans son autorisation.

0-612-20935-0

Canada

Abstract

Ideal annite has structural formula $\{K^{+}\}[Fe_3^{2+}]<Al^{3+}Si_3^{4+}>O_{10}^{2-}(OH^{-})_2$ where { }, [ ], and < > represent the interlayer, octahedral, and tetrahedral sites, respectively. Simple crystal chemical considerations suggest that ideal annite should exist as do other end-members having Fe replaced by Mg, Ni, Co, etc. However, due to structural constraints involving long range layer misfit and short range bond matching, ideal annite is never synthesized. Instead, the constraints are satisfied by both non-destructive partial oxydation (via H-loss) of the Fe^{2+}, and Fe^{3+}–Al^{3+} exchange. Consequently, real annite must actually contain small fractions of both $[Fe^{3+}]$ and $<Fe^{3+}>$ with an associated amount of hydrogen deficiency. The observed stoichiometry of real annite (assuming no octahedral vacancies) is:

$$\left\{K^{+}\right\}\left[Fe_{1-x-y}^{2+}Fe_{x}^{3+}Al_{y}^{3+}\right]_3 < Al_{1-3y}^{3+}Fe_{3y}^{3+}Si_{3}^{4+} > O_{10+3x+3y}^{2-}(OH^{-})_{2-3x-3y}$$

where $x=\frac{[Fe^{3+}]}{Fe_{tot}}$ and $y=\frac{<Fe^{3+}>}{Fe_{tot}}$.

We measured Fe^{3+} (x and y) and Fe^{2+} site populations in nine annite samples synthesized using the C-CH_4 and Ni-NiO buffers, and various equilibration temperatures. The measurements were performed using the most recent Mössbauer spectroscopy data treatment and spectral analysis methods. These include (1) analytic methods for removing the spectral distortions associated to the effects of absorber thickness and (2) a powerful Voigt-based fitting method that allows arbitrary-shape quadrupole splitting distributions for each site. We obtained site population measurements with precisions of 0.2–1% of Fe_{tot}, whereas the generally accepted limit is 1–5% of Fe_{tot}.

By using temperatures over the entire stability range for annite, we have traced the evolution of $[Fe^{3+}]$ and $<Fe^{3+}>$ site populations and have obtained an experimental lower bound on $\frac{Fe^{3+}}{Fe_{tot}}$. Temperature is seen to have a systematic effect that is understood in terms of differential thermal expansion between the octahedral and tetrahedral layers. To explain this effect, we propose a structural misfit model for annite mica that gives definite predictions on the $[Fe^{3+}]$ and $<Fe^{3+}>$ site populations and includes a cation size dependant octahedral flattening and the effect of octahedral/tetrahedral sheet differential thermal expansion.

Acknowledgements

I would like to begin by thanking my supervisor Dr. Denis G. Rancourt for collecting the spectra and for suggesting the project. His patience, the generosity of his financial support, the thoughtfullness of his advice, and the excellence of his instruction have all been very much appreciated. I have learned a great deal about research from working under his direction.

This thesis could not have been completed without the contributions of many important collaborators. I owe a debt of gratitude to Dr. R.G. Berman for the syntheses of most of the samples, for the equilibration of annite IKO-Ann (or HK-NNO) at different temperatures, and for his invaluable help in understanding the background of hydrothermal experiments. I am also very greatful to Dr. A.E. Lalonde for providing considerable assistance and knowledge in the powder X-ray diffraction measurements and the scanning electron microscopy of all samples. I would also like to thank Dr. E. Murad and and Dr. S. Guggenheim for performing independent X-ray diffraction studies of some samples, and Dr. J.–L. Robert who synthesized annite HK-NNO in this study.

In addition, I would like to express my sincere appreciation to my fellow graduate student and friend Ms. Mei-Zhen Dang with whom I shared office space. I benefited enormously of your camaraderie, happiness, explanations and useful discussions.

Finalement, et non les moindres, je tiens à remercier tous ceux qui de près ou de loin ont contribué à mon bien-être moral tout au long de ce projet. En particulier, je remercie affectueusement mon père, ma mère et mon frère pour leur support constant.

List of Abbreviations and Symbols

[ ]	Denotes an octahedral site.
< >	Denotes a tetrahedral site.
{ }	Denotes an interlayer site.
α	Tetrahedral rotation angle.
α_o	Thermal expansion coefficient for octahedral bonds.
α_t	Thermal expansion coefficient for tetrahedral bonds.
γ	Lorentzian full width at half maximum.
Γ_o	Natural linewidth full width of the Mössbauer transition.
δ	Center shift.
δE_e	Energy shift of the excited state.
δE_g	Energy shift of the ground state.
δ_0	Value of δ when the distributed hyperfine parameter has a value of zero or, depending on context, center of a Gaussian component of a δ-distribution.
δ_1	Coupling of δ to distributed hyperfine parameter.
Δ	Quadrupole splitting.
Δ_0	Center of a Gaussian component of a quadrupole splitting distribution.
η	Asymmetry parameter.
η_M	Part of the background that is both from recoilless and nonrecoilless Mössbauer γ-rays.
θ_D	Debye temperature.
ν	Frequency detected by the observer.
ν_o	Frequency emitted by the source.
σ_Δ	Standard deviation of a QSD.

σ_{Δ_i}	Gaussian width of a Gaussian component in a QSD.
$\sigma_a^{'}$	Total resonant absorber cross section.
$\sigma_{a,i}^{'}(E)$	Site-specific absorber resonant cross section.
$\sigma_{a,i}(E)$	Site-specific intrinsic absorber resonant cross section.
σ_o	Cross section at resonance for the Mössbauer transition.
v	Number of degrees of freedom.
χ^2, χ^2_{red}	Chi-squared, reduced chi-squared.
ψ	γ-ray energy, velocity channel, or octahedral layer flattening angle.
$\|\Psi(0)\|^2$	Electron density at the nucleus.
a	Lattice parameter.
A	Intercept for the b as a function of $[R]$ relationship.
A_i	Subspectral area corresponding to the i-th site.
A_k	Area of the k-th Voigt line.
Ann	Mineral symbol for annite.
b	Lattice parameter.
B	Slope for the b as a function of $[R]$ relationship.
BG	Background.
c	Lattice parameter.
C-CH_4	Graphite-methane (buffer).
CS	Center shift.
d_o	Average octahedral bond length.
d_t	Average tetrahedral bond length.
$D(\psi)$	Elemental doublet spectrum.
e	Proton charge.
$\vec{E}$	Electric field.
E_γ	Energy of the emitted γ-radiation.
EDS	Energy dispersive spectrometer.
EFG	Electric field gradient.
$\bar{f}$	Average recoilles fraction.

f_a	Recoilless fraction of the absorber.
$f_{a,i}$	Site-specific absorber recoilles fraction.
f_i	Recoilless fraction of the i-th site.
f_s	Recoilless fraction of the single-line thin source.
Fa	Mineral symbol for fayalite.
FWHM	Full width at half maximum.
h_i, h_k	Lorentzian height of the i-th/k-th Lorentzian or Voigt line.
$\hbar$	Planck's constant divided by 2π.
$\hat{H}_Q$	Hamiltonian associated to the interaction between the electric nuclear quadrupole moment and the electronic electric field gradient at the nucleus.
I	Nuclear spin quantum number.
ICDD	International Center for Diffraction Data.
$I(E)$	Mössbauer transition intensity as a function of transition energy.
$\hat{I}$	Nuclear spin operator.
$\hat{I}_\pm$	Raising/lowering operators.
$\hat{I}_x$, $\hat{I}_y$, $\hat{I}_z$	Nuclear spin projections onto the principal axes.
IS	Isomer shift.
k_B	Boltzman's connstant.
m_I	Magnetic spin quantum number.
MCS	Multichannel scalar.
MS	Mössbauer spectroscopy.
n_a	Number of ^{57}Fe nuclei per unit surface area in the absorber.
$n_{a,i}$	Number of ^{57}Fe nuclei per unit surface area in the i-th site of the absorber.
$n_G(E)$	Gaussian noise.
$N(E)$	Measured absorption spectrum.
Ni-NiO	Nickel-nickel oxyde (buffer).
$N_{th}(E)$	Thin absorber expression for the measured spectrum.
O	Octahedral.

p_i	Population of the i-th site.
$P(\delta)$, $P(\Delta)$	Static hyperfine parameter distribution of center shifts and quadrupole splittings, respectively.
QS	Quadrupole splitting.
QSD	Quadrupole splitting distribution.
R_a	Average RT anion radius.
R_e	Radius of the excited state.
R_g	Radius of the ground state.
$[R]$	Average octahedral cation radius calculated from stoichiometry and tabulated radii.
RT	Room temperature.
Sa	Mineral symbol for sanidine.
SEM	Scanning electron microscopy.
SCA	Single channel analyser.
SOD	Second order Doppler shift.
Syl	Mineral symbol for sylvite.
$t_{\frac{1}{2}}$	Half-life.
T	Tetrahedral.
T	Temperature or equilibration/synthesis temperature.
v	Relative velocity.
V	Electric potential.
V_{ij}	Components of the EFG tensor.
XRD	X-ray diffraction.
Z	Atomic number.

Contents

Abstract ii

Acknowledgements iv

List of Abbreviations and Symbols v

1. Introduction 1

2. Mössbauer Spectroscopy Background 2

- 2.1 The Mössbauer effect 2
- 2.2 Relevant hyperfine interactions 3
  - 2.2.1 Center shift 4
  - 2.2.2 Quadrupole splitting 6
- 2.3 Physical origin of the quadrupole splitting distributions 9
- 2.4 Experimental artifacts and other factors altering the lineshape of a Mössbauer spectrum 11
- 2.5 Treating effects due to absorber thickness 12
- 2.6 Accurate site populations 13

3. Structure and Crystal Chemistry of Annite 15

- 3.1 Micas: structure and nomenclature 15
- 3.2 Structure and crystal chemistry of annite 17
  - 3.2.1 Ideal structure of annite 17
  - 3.2.2 Structural distortions and the real structure of annite 18
  - 3.2.3 Mössbauer spectrum of a typical annite sample 22

4. Structural Misfit Model for the Annite Mica 24

5. Sample Characterization 26
5.1 Synthesis description 26
5.2 Scanning electron microscopy 28
5.3 X-ray diffraction 38

6. Experimental Methods for Mössbauer Spectroscopy 49
6.1 Equipment 49
6.2 Absorber preparation 50

7. Data Treatment and Spectral Analysis Methods 52
7.1 Calibration and folding procedures 52
7.2 Thickness corrections 52
7.2.1 Intrinsic resonant absorber cross section and the measured spectrum 52
7.2.2 Obtaining the intrinsic resonant absorber cross section by deconvolution methods 55
7.2.3 Generating a thin-limit spectrum 56
7.3 Fitting model used for the determination of accurate site populations 57
7.3.1 Fitting model for arbitrary-shape quadrupole splitting distributions 57
7.3.2 Relevance of a given fitting model 59
7.3.3 Accurate site populations 60

8. Results of the Mössbauer Analysis 62
8.1 QSD analysis of raw spectra 62
8.2 Obtaining thin-limit spectra 71
8.3 QSD analysis of thin-limit spectra 73
8.4 Site populations 83
8.5 Summary 96

9. Comparison of Population Results with the Misfit Model 97

10.Conclusion **106**

10.1 Summary 106

10.2 Suggestions for future work 107

Note added in proof **108**

A. Parameters of the Voigt Fits Used for Thickness-corrections **111**

B. Analysis of the XRD diffractograms **116**

References **137**

List of Tables

5.1 Synthesis condition for our annite samples. 26

5.2 (a) ICDD patterns of other phases which might have occurred in the run products. (b) Stoichiometric formulae of other possible phases. . 47

5.3 Summary of the XRD analysis. 48

6.1 Amounts of sample used for each of the holder and associated thicknesses. 51

8.1 Fit parameters of raw ^{57}Fe Mössbauer spectra for the HK-NNO C-CH_4 annealed samples. 63

8.2 Fit parameters of raw ^{57}Fe Mössbauer spectra for the samples synthesized straight from stoichiometric mixtures. 64

8.3 QSD characteristic parameters for raw spectra. 71

8.4 Fe^{2+} QSD characteristic parameters for thin-limit spectra. 74

8.5 Fit parameters of thin-limit spectra for the HK-NNO C-CH_4 annealed samples. 75

8.6 Fit parameters of thin-limit spectra for the samples synthesized straight from stoichiometric mixtures. 76

8.7 Site populations obtained from the QSD analysis of raw and thin-limit spectra. 84

8.8 Lower and upper bounds on site populations obtained from the solution domains. 86

8.9 Results of the cross section method. 89

8.10 Fit parameters of thin-limit spectra (HK-550,. . . , HK-750) in which we impose a minimum $<Fe^{3+}>$ contribution. 92

8.11 Fit parameters of thin-limit spectra (HK-NNO, RB-. . .) in which we impose a minimum $<Fe^{3+}>$ contribution. 93

8.12 Fit parameters of thin-limit spectra (HK-550,...,HK-750) in which we impose a maximum <Fe^{3+}> contribution. 94
8.13 Fit parameters of thin-limit spectra (HK-NNO, RB-...) in which we impose a maximum <Fe^{3+}> contribution. 95
9.1 Results of the fitting process used to compare the site population measurements with the structural misfit model. 103
A.1 Voigt fit parameters for sample HK-550. 111
A.2 Voigt fit parameters for samples HK-596 and HK-650. 112
A.3 Voigt fit parameters for samples HK-700 and HK-750. 113
A.4 Voigt fit parameters for samples HK-NNO and RB-22. 114
A.5 Voigt fit parameters for samples RB-25 and RB-7. 115
B.1 XRD peaks observed for annite HK-550. 118
B.2 (cont'd) XRD peaks observed for annite HK-550. 119
B.3 XRD peaks observed for annite HK-596. 120
B.4 (cont'd) XRD peaks observed for annite HK-596. 121
B.5 XRD peaks observed for annite HK-650. 122
B.6 (cont'd) XRD peaks observed for annite HK-650. 123
B.7 XRD peaks observed for annite HK-700. 124
B.8 (cont'd)XRD peaks observed for annite HK-700. 125
B.9 XRD peaks observed for annite HK-750. 126
B.10 (cont'd) XRD peaks observed for annite HK-750. 127
B.11 XRD peaks observed for annite HK-NNO. 128
B.12 (cont'd) XRD peaks observed for annite HK-NNO. 129
B.13 XRD peaks observed for annite RB-25. 130
B.14 (cont'd) XRD peaks observed for annite RB-25. 131
B.15 XRD peaks observed for annite RB-7. 132
B.16 (cont'd) XRD peaks observed for annite RB-7. 133
B.17 (cont'd) XRD peaks observed for annite RB-7. 134
B.18 XRD peaks observed for annite RB-22. The intensities were estimated visually from the film produced by the Gandolfi camera. 135

B.19 (cont'd) XRD peaks observed for annite RB-22. The intensities were estimated visually from the film produced by the Gandolfi camera. . . 136

List of Figures

2.1 (a) Quadrupole splitting in ^{57}Fe nuclear level diagram with . (b) Resultant elemental quadrupole doublet spectrum (schematic). 8

3.1 Mica structure. Large full circles are cations in O sites, small filled circles are cations in T sites, and open circles are oxygens. K^+ represents the interlayer cation content between adjacent TOT layer. . . 16

3.2 Expansion of the octahedral 001 projection by octahedral layer compression. From Hazen and Wones [16]. 19

3.3 Contraction of the tetrahedral 001 projection by tetrahedral layer rotation. From Hazen and Wones [16]. 20

3.4 The Mössbauer spectrum of an annite at RT showing the approximate positions of the [Fe^{2+}], [Fe^{3+}], and <Fe^{3+}> sites. 23

5.1 Hydrogen and oxygen fugacity values of the C-CH_4 [21] and Ni-NiO [22] buffers. 27

5.2 SEM photomicrograph of sample HK-550. Scale is as indicated by the white horizontal bar. 29

5.3 SEM photomicrograph of sample HK-596. Scale is as indicated by the white horizontal bar. 30

5.4 SEM photomicrograph of sample HK-650. Scale is as indicated by the white horizontal bar. 31

5.5 SEM photomicrograph of sample HK-700. Scale is as indicated by the white horizontal bar. 32

5.6 SEM photomicrograph of sample HK-750. Scale is as indicated by the white horizontal bar. 33

5.7 SEM photomicrograph of sample HK-NNO. Scale is as indicated by the white horizontal bar. 34

5.8 SEM photomicrograph of sample RB-22. Scale is as indicated by the white horizontal bar. 35
5.9 SEM photomicrograph of sample RB-25. Scale is as indicated by the white horizontal bar. 36
5.10 SEM photomicrograph of sample RB-7. Scale is as indicated by the white horizontal bar. 37
5.11 XRD powder diffractogram of sample HK-550. 39
5.12 XRD powder diffractogram of sample HK-596. 40
5.13 XRD powder diffractogram of sample HK-650. 41
5.14 XRD powder diffractogram of sample HK-700. 42
5.15 XRD powder diffractogram of sample HK-750. 43
5.16 XRD powder diffractogram of sample HK-NNO. 44
5.17 XRD powder diffractogram of sample RB-25. 45
5.18 XRD powder diffractogram of sample RB-7. 46
8.1 Raw spectra of synthetic annite HK-550 (top) and HK-596 (bottom) with fits and residuals. 65
8.2 Raw spectra of synthetic annite HK-NNO (top) and HK-650 (bottom) with fits and residuals. 66
8.3 Raw spectra of synthetic annite HK-700 (top) and HK-750 (bottom) with fits and residuals. 67
8.4 Raw spectra of synthetic annite RB-25 (top) and RB-22 (bottom) with fits and residuals. 68
8.5 Raw spectrum of synthetic annite RB-7 with fit and residual. 69
8.6 Fe^{2+} QSDs for all raw spectra: HK-samples, solid lines; RB-7, close-dots; RB-22, spaced-dots; and RB-25, dashes. 70
8.7 Thickness correction for the RT spectrum of annite HK-596. (a) Raw folded spectrum with ideal Voigt line fit and difference spectrum. (b) Extracted dimensionless intrinsic absorber resonance cross section. (c) Thin-limit spectrum with simulated Gaussian noise. 72
8.8 Thin-limit spectra of synthetic annite HK-550 (top) and HK-596 (bottom) with fits and residuals. 77

8.9 Thin-limit spectra of synthetic annite HK-NNO (top) and HK-650 (bottom) with fits and residuals. 78

8.10 Thin-limit spectra of synthetic annite HK-700 (top) and HK-750 (bottom) with fits and residuals. 79

8.11 Thin-limit spectra of synthetic annite RB-25 (top) and RB-22 (bottom) with fits and residuals. 80

8.12 Thin-limit spectrum of synthetic annite RB-7 with fit and residual. . 81

8.13 Fe^{2+} QSDs for all thin-limit spectra: HK-samples, solid lines; RB-7, close-dots; RB-22, spaced-dots; and RB-25, dashes. 82

8.14 The <Fe^{3+}> (circles) and [Fe^{3+}] (squares) site populations. The upper and lower bounds of the acceptable range for each population are shown. The uncertainty of each measurement is a result of trade-off problems. 87

8.15 The total Fe^{3+} contribution. The QSD analysis gives an upper-limit (triangle-up) and a lower-limit (triangle-down) for the Fe^{3+}/Fe_{tot}, as a result of trade-off problems. The line made of hollow circles represents the results of the cross section method. 91

9.1 Measured [Fe^{3+}] and <Fe^{3+}> site populations compared to the structural misfit model: (a) $T = RT$ and (A, B) = (8.17Å, 1.46) (dashed line), (7.64Å, 2.19) (dotted line), (7.39Å, 2.52) (solid line); (b) T = 550 and 750°C with (A,B) = (8.17Å, 1.46) (dashed lines), (7.39Å, 2.52) (solid lines). Samples are 1=HK-NNO, 2-6=HK-550-750, 7=RB-7, 8=RB-25, 9=RB-22. 99

9.2 The effect of changing the (A,B) parameters: (a) (A,B) = (7.640 Å, 2.188), and (b) (A,B) = (8.166 Å, 1.457). The values of the other parameters are as follows: α_t=0 and α_o = 10×10^{-6} °C^{-1} (dotted lines), 25×10^{-6} °C^{-1} (dashed lines), 40×10^{-6} °C^{-1} (solid lines). . . . 100

9.3 The effect of changing the α_o and α_t parameters (A = 7.640 Å, B = 2.188): (a) α_t=0 and α_o= 10×10^{-6} °C^{-1} (dotted lines), 25×10^{-6} °C^{-1} (dashed lines), 40×10^{-6} °C^{-1} (solid lines); (b) α_t=10×10^{-6} °C^{-1} and α_o = 10×10^{-6} °C^{-1} (dotted lines), 20×10^{-6} °C^{-1} (short-dashed lines: T=550 °C, filled triangles; T=750 °C, open circles), 35×10^{-6} °C^{-1} (dashed lines), 50×10^{-6} °C^{-1} (solid lines). 101

9.4 Range of acceptable (A,B) values (see note added in proof) that are consistent with the data of Hazen and Wones [17]. Dots are fitted (A,B) values obtained for the various imposed α_t coefficients. 104

9.5 Theoretical predictions corresponding to fitted values of (A,B) and α_o for the lowest (top) and highest (bottom) χ^2 values obtained (see note added to proof). Samples are: 1 = HK-596, 2 = HK-650, 3 = HK-700. 105

10.1 Revised range of acceptable (A,B) values that are consistent with the data of Hazen and Wones [17]. Squares represent examples of (A,B) values that give acceptable fits to the data of Hazen and Wones. Dots are fitted (A,B) values obtained from our structural misfit model. . . 109

10.2 Reproduction of Hazen and Wones' data [17] (filled circles) along with our evaluation of the lattice parameter b and average octahedral cation radius [R] for our annite specimens (filled triangles). The solid lines arise from the fitted values of (A,B) from our structural misfit model. 110

Chapter 1. Introduction

This thesis reports Fe^{3+} and Fe^{2+} site population measurements in nine annite specimens synthesized at different equilibration temperatures and oxygen fugacity buffers. The Mössbauer spectroscopy analysis methods, which involved full thickness effect corrections and quadrupole splitting distribution analysis, have been described in a recent series of papers [1, 2, 3].

Micas are a large class of materials which have long been important to geologists as probes of rock formation conditions. Annite is the Fe end-member of a Mg-Fe solid solution of trioctahedral micas having phlogopite as its Mg end-member. The Fe-rich member of this solid solution is called biotite and represents one of the most common rock-forming minerals, present in assemblages of diverse bulk compositions and origins. The ratio Fe^{3+} to Fe^{2+} in a mica is the basis of an oxygen fugacity scale widely used in the study of igneous and metamormophic rocks [4]. Furthermore, biotite has recently been the basis of a classification scheme established to distinguish the diverse tectonic origin of granitic rocks.

The chemical complexity of biotite is manifested by a wide range of both cationic and anionic substitutions. Further understanding of the crystal chemistry of biotite could enable us to yield much more information about rock equilibration conditions. The present study of annite represents a logical starting point in this direction.

In the present work, by using temperatures over the entire stability range for annite, we have traced the evolution of tetrahedral and octahedral Fe^{3+} and have obtained an experimental lower bound on the total Fe^{3+} content. In light of our experimental results, temperature has a systematic effect that is understood in terms of differential thermal expansion between the tetrahedral and octahedral sheets.

Chapter 2. Mössbauer Spectroscopy Background

2.1 The Mössbauer effect

The phenomenon of the emission (or absorption) of a γ-ray photon without loss of energy due to recoil of the nucleus and without thermal broadening is known as the Mössbauer effect. It corresponds to a nuclear transition from an excited state to a ground state (or vice-versa). Mössbauer spectroscopy (MS) is therefore a nuclear spectroscopy. It relies on recoilless emission and subsequent recoilless resonant absorption of a γ-ray.

An excited state of mean lifetime τ can never be assigned a sharp energy value. Instead the energy level spreads over a certain energy range of width ΔE, which correlates with the Heisenberg uncertainty principle:

$$\Delta E \Delta t \geq \hbar \tag{2.1}$$

($\hbar$ = Planck's constant divided by 2π). Δt, also considered as the time interval available to measure the energy, is in the order of the mean lifetime. We may then calculate the natural linewidth (Γ_o) of the γ-radiation on the basis of the Heisenberg relation:

$$\Gamma_o = \frac{\hbar}{\tau}. \tag{2.2}$$

Here, Γ_o is more precisely the natural full width at half maximum (FWHM) of the energy distribution. The transition intensity as a function of the transition energy, $I(E)$, yields a spectral line centered around the most probable energy, E_o. The spectral line has a Breit-Wigner Lorentzian type profile:

$$I(E) = const. \frac{\Gamma_o}{2\pi} \frac{1}{(E - E_o)^2 + (\Gamma_o/2)^2}. \tag{2.3}$$

In the case of ^{57}Fe MS, the 14.4 keV Mössbauer transition has a measured half-life, ($t_{\frac{1}{2}}$), of 97.7 ns ($\tau = \ln 2 \times t_{\frac{1}{2}}$). This results in a very narrowly defined emission (or absorption) line having a theoretical value of $\Gamma_o = 4.67 \times 10^{-9}$ eV (or 0.097 mm/s).

By Doppler shifting the energy of the thus emitted photons, it is possible to scan a certain range of photon energies. Exposing a material that contains the same Mössbauer nuclei as the emitter to this energy scan produces an absorption spectrum for this sample. It is in general enough to apply a small Doppler velocity to the source (or the absorber) to sweep over the resonance. In such an experiment, an emission of natural line width Γ_o is moved over an absorption of the same line width, thus producing a spectrum in which we will observe the sum of both resonance widths ($2\Gamma_o$).

2.2 Relevant hyperfine interactions

Given that the width of the resonance line is small, a Mössbauer spectrum is very sensitive to even quite small energy changes. Such changes occur in the energy state of the nucleus as a result of interaction with the external environment (the electron shell and other atoms in the crystal).

The hyperfine interactions consist of interactions between the nucleus and extra-nuclear electric and magnetic fields that are due to the surrounding electrons. The hyperfine interactions which manifest themselves in MS are:

1. the center shift,
2. the electric quadrupole interaction, and
3. the magnetic hyperfine interaction.

The third one is the interaction between the nuclear magnetic dipole moment and the hyperfine field. Since there are no effective hyperfine fields present in our samples, we are not concerned with describing the effect of such an interaction.

2.2.1 Center shift

The center shift (CS) is the combination of two terms,

$$CS = IS + SOD, \tag{2.4}$$

the isomer shift (IS) and the second order Doppler shift (SOD).

The first term arises from the interaction between the positive nuclear charge (which occupies a small but finite volume) and the electric charge of the surrounding electrons. This interaction leads to a shift of the nuclear energy levels compared to those for a bare nucleus: the magnitude of the shift is a function of the electronic charge density at the nucleus, that is sensitive to the local electronic structure. Thus similar nuclei in different environments will have energy levels that are shifted by different amounts according to the specific details of the nuclear environments. Also, a nucleus is generally of different sizes in its ground and excited states: consequently the monopole interaction causes both a change in the absolute energies of the ground and excited state plus a relative change in the energy levels, a change that stems from this size difference. This relative change may be expressed as [5]:

$$IS = \delta E_e - \delta E_g = \frac{2\pi}{5} \mathcal{Z} e^2 |\Psi(0)|^2 |R_e{}^2 - R_g{}^2| \tag{2.5}$$

where

- δE_e is the energy shift of the excited state,
- δE_g is the energy shift of the ground state,
- e is the proton charge,
- $\mathcal{Z}$ is the atomic number,
- $|\Psi(0)|^2$ is the electron density at the nucleus,
- R_e and R_g are the radii of the excited and ground states, respectively.

The second term which composes the CS is the SOD. It arises from the relativistic Doppler effect [6, 7]. The SOD is caused by the vibrations of the emitting and absorbing atoms on their lattice sites. In general the vibrating atoms in a solid make many oscillations during the lifetime of the excited nuclear state, thus the average velocity is zero and a first-order Doppler shift cannot be observed. However, the average squared velocity of the oscillating atoms causes a shift of the resonance line from the second-order Doppler term.

The relativistic Doppler equation is written as [5]:

$$\nu = \nu_o \frac{1 - \vec{v} \cdot \vec{r} r/c}{\sqrt{1 - v^2/c^2}} \tag{2.6}$$

where ν_o is the frequency emitted by the source, ν is the frequency detected by the observer, $\vec{v}$ is the relative velocity, $\vec{r}$ is the unit vector in direction of advance of the photons and c is the velocity of light. The mean value in time of the term vr/c is zero, and so [5]

$$\nu = \nu_o \frac{1}{\sqrt{1 - v^2/c^2}} \approx \nu_o \left(1 + \frac{1}{2}\frac{v^2}{c^2}\right). \tag{2.7}$$

Thus the energy change is

$$SOD = h(\nu - \nu_o) = \frac{h\nu_o}{2}\frac{v^2}{c^2} = \frac{1}{2}E_\gamma \frac{v^2}{c^2} \tag{2.8}$$

where E_γ is the energy of the emitted γ-radiation. The mean value of v^2 depends on the temperature of the substance. This shift is termed the SOD.

Calculation of the SOD requires the choice of a particular phonon model for the solid. In the case of the Debye model, the SOD is given by [8, 9]:

$$\frac{<\nu^2>}{2c} = -\frac{3k_B\theta_D}{2mc}\left[\frac{3}{8} + 3\left(\frac{T}{\theta_D}\right)^4 \int_0^{\theta_D/T} \frac{x^3}{(e^x - 1)}dx\right] \tag{2.9}$$

where ν is the nuclear vibration velocity, k_B is the Boltzman constant, θ_D is the Debye temperature and T is the temperature.

In MS one measures the CS of the absorber (a) relative to that of some chosen standard (s) absorber at a specific temperature. Our chosen standard absorber, which defines the zero in absorber CS, is metallic α-Fe at room temperature (RT=

$22°C$). The resulting energy difference is called the total center shift, δ, and can thus be written as

$$\delta = CS_a - CS_s = [IS_a - IS_s] + [SOD_a - SOD_s]. \qquad (2.10)$$

We may also express the IS contribution as in Equation 2.5. Putting $R_e - R_g = \Delta R$ and $R_e + R_g = 2R$ (R_e and R_g differ only slightly from each other), we then find the more frequently encountered expression:

$$\delta = \frac{4\pi}{5} Ze^2R^2 \left(\frac{\Delta R}{R}\right) \left[|\Psi(0)|^2_a - |\Psi(0)|^2_s\right] + [SOD_a - SOD_s]. \qquad (2.11)$$

The prefactors in the IS difference are constant for a given nucleus and the electron density of the standard is expected to be weakly temperature dependant for a given standard. As for the SOD difference, it is more strongly temperature dependant. Consequently, the temperature of the standard or reference absorber must be specified.

2.2.2 Quadrupole splitting

The second relevant hyperfine interaction arises from the interaction of the nuclear quadrupole moment and the electric field gradient (EFG) on the site of the atomic nucleus. When a nucleus has a quadrupole moment, it may interact with any component of the electric field gradient. This leads to a splitting of nuclear energy levels called the quadrupole splitting.

The magnitude of the quadrupole splitting is a function of the EFG. The electric field ($\vec{E}$) is the negative gradient of the potential V and the EFG is the gradient of $\vec{E}$, so we have:

$$EFG = \vec{\nabla}\vec{E} = -\vec{\nabla}\vec{\nabla}V \qquad (2.12)$$

and

$$\frac{\partial^2 V}{\partial x_i \partial x_j} = V_{ij} \quad ; \quad \{x_i, x_j = x, y, z\} \qquad (2.13)$$

where V_{ij} are the nine components of the EFG tensor.

The EFG tensor is symmetrical, and can always be diagonalised by an appropriate choice of (electric field gradient) axes, whereupon all off-diagonal elements are zero.

Furthermore, because of Laplace's equation, which requires the EFG to be a traceless tensor, we have:

$$V_{xx} + V_{yy} + V_{zz} = 0 \tag{2.14}$$

If we choose the principal axes such that the ordering [10]

$$|V_{zz}| \geq |V_{yy}| \geq |V_{xx}| \tag{2.15}$$

holds, we can specify the EFG by two independent parameters:

1. V_{zz}, sometimes denoted as eq (e = proton charge, q = a certain number that reflects the maximum value of the EFG)
2. the asymmetry parameter η, defined as

$$\eta = \frac{V_{xx} - V_{yy}}{V_{zz}} \tag{2.16}$$

With (2.15), the value of η is constrained to lie between 0 and 1.

Given the above definitions, one may calculate the splitting associated to the interaction between the electric quadrupole moment, eQ, and the EFG at the nucleus (which is described by V_{zz} and η). This interaction, in the principal axes system with z-axis as axis of quantization, may be expressed by the Hamiltonian [11]

$$\hat{H}_Q = \frac{eQV_{zz}}{4I(2I-1)}\left[3\hat{I}_z^2 - \hat{I}^2 + \eta(\hat{I}_+^2 + \hat{I}_-^2)/2\right]. \tag{2.17}$$

I is the nuclear spin quantum number, $\hat{I}$ is the nuclear spin operator,$\hat{I}_\pm = \hat{I}_x \pm \hat{I}_y$ are the raising/lowering operators, and $\hat{I}_x$, $\hat{I}_y$, $\hat{I}_z$ are the nuclear spin projections onto the principal axes. By diagonalisation of the matrix of $\hat{H}_Q$, one finds the eigenvalues E_Q:

$$E_Q = \frac{eQV_{zz}}{4I(2I-1)}\left[3m_I^2 - I(I+1)\right](1 + \frac{\eta^2}{3})^{\frac{1}{2}}, \tag{2.18}$$

where $m_I = I, I-1, \ldots, -I$ is the nuclear magnetic spin quantum number.

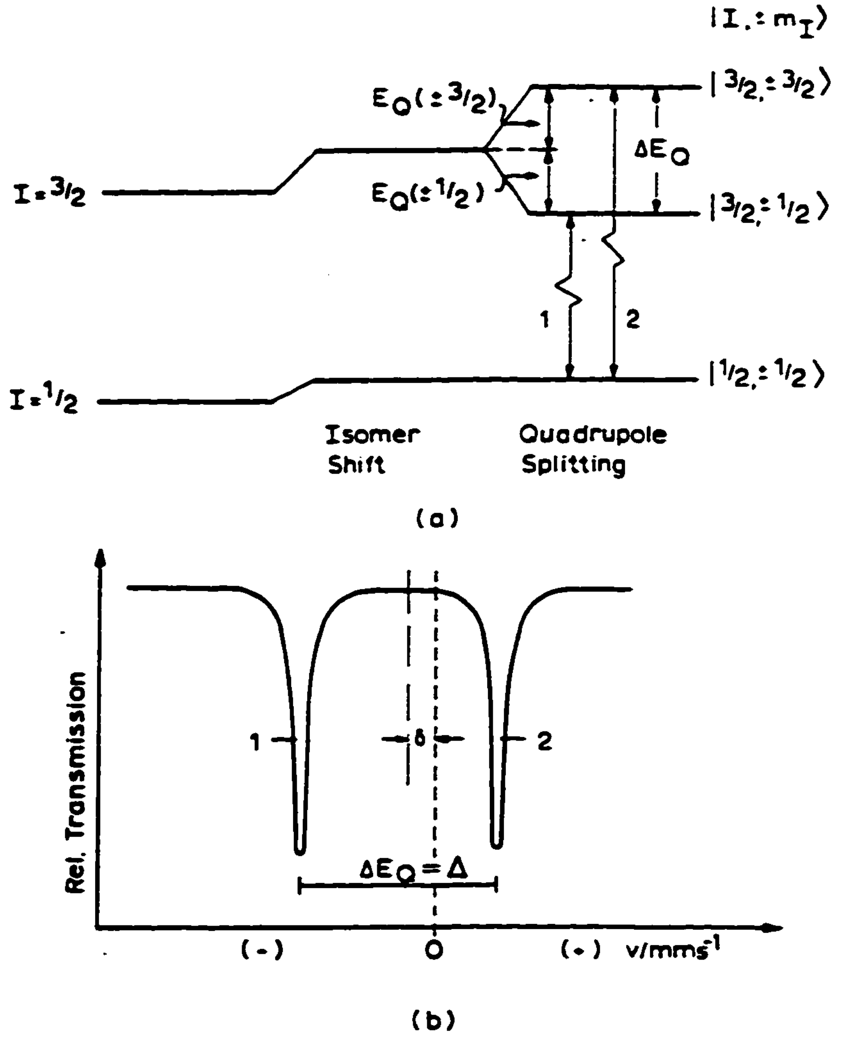

Figure 2.1: (a) Quadrupole splitting in ^{57}Fe nuclear level diagram with . (b) Resultant elemental quadrupole doublet spectrum (schematic).

As an example, the effect of electric quadrupole interaction in ^{57}Fe with $I = \frac{3}{2}$ is shown in Fig.2.1. The nuclear ground state is not split, because there is no nuclear quadrupole moment with $I = 0, \frac{1}{2}$. The excited state with $I = \frac{3}{2}$ splits into two doubly degenerate states substates $|\frac{3}{2}, \pm\frac{3}{2}>$ and $|\frac{3}{2}, \pm\frac{1}{2}>$. Using 2.18, the energies can be calculated and in doing so, we see that the level of the baricenter of the $I = \frac{3}{2}$ level is not affected by the electric quadrupole interaction.

In the spectrum (Fig.2.1), there are two peaks, corresponding to the two transitions $(\pm\frac{3}{2} \rightarrow \pm\frac{1}{2}, \pm\frac{1}{2} \rightarrow \pm\frac{1}{2})$. The energy separation between these two peaks is the quadrupole splitting Δ:

$$\Delta = \frac{e^2qQ}{2}(1+\frac{\eta^2}{3})^{\frac{1}{2}} \tag{2.19}$$

which is a measure of the energy splitting of the excited state $(V_{zz} \equiv eq)$.

2.3 Physical origin of the quadrupole splitting distributions

In the preceeding section, we defined what we may call an elemental contribution to the Mössbauer spectrum. For a non-magnetically ordered material and in the absence of dynamic effects, the elemental spectrum corresponding to the 14.4 keV transition in ^{57}Fe must consist of a doublet.

The lineshape of an elemental doublet spectrum is the sum of two Lorentzian lines (see Fig.2.1), which can be written as [12]:

$$D(\psi) = BG - \sum_{k=-1,1} L(\delta + k\frac{\Delta}{2}, \gamma, h_k; \psi) \tag{2.20}$$

where ψ is the γ-ray energy (in mm/s) and BG is the background as observed far away from all Mössbauer transitions. The Lorentzian function has the following form:

$$L(\delta + k\frac{\Delta}{2}, \gamma, h_k; \psi) = \frac{h_k\frac{\gamma^2}{4}}{\left\{\psi - \left[\delta + k\frac{\Delta}{2}\right]\right\}^2 + \frac{\gamma^2}{4}} \tag{2.21}$$

This describes a single Lorentzian line with height h_k, full width at half maximum (FWHM) γ, and centered on $\left[\delta + k\frac{\Delta}{2}\right]$.

Since most minerals and materials have many non-equivalent crystallographic sites or local environments that are occupied by the Mössbauer nuclei, the Mössbauer spectrum of a non-magnetically-ordered material in general, consists of a superposition of elemental doublets. Although elemental lines that are due to single groups of identical probe environments must, in the absence of experimental artifacts, be Lorentzian in shape, absorption lines that are made up of several overlapping Lorentzians having a spread in positions are not Lorentzian in shape.

A given species in a given anion coordination has many different local environments that are defined by local distortions (defects, vacancies,...), local charge distributions, local compositions, the types and positions of the next near neighbour cations, etc. Each local environment gives rise to a single elemental quadrupole doublet such that a continuous distribution of quadrupole splittings can be used to model the Mössbauer spectrum.

A powerful new method for fitting with quadrupole splitting distributions (QSDs) has been developed [13] and is explained in section 7.3. We use this method here to study annite specimens synthesized under different temperatures and oxygen fugacities. Although the individual elemental quadrupole doublets in the Mössbauer spectrum of these materials cannot be resolved, it is possible to model the spectrum such that distinct sets of hyperfine parameters are determined.

The hyperfine parameters of a given set are the characteristics of a particular group of probe ions which have similar environments. We refer to such a group as a generalized site. Each generalized site has its own QSD and its own set of certain hyperfine parameters (e.g., center shifts). In the present application, it turns out that three such generalized sites with independent QSDs are required and that these corresponds to Fe^{3+} in octahedral and tetrahedral coordination, and Fe^{2+} in octahedral coordination.

Thus, by (generalized) site, we mean here a particular valence state of the ion and a particular anion coordination that give rise to a distinct spectral component. Each such site is therefore an entire family of crystallographic sites that differ only by such characteristics as local structural and local chemical features.

2.4 Experimental artifacts and other factors altering the lineshape of a Mössbauer spectrum

Several experimental artifacts can, under particular circumstances, cause significant spectral distortions. The most important of all are the effects related to finite absorber thickness, which is the only unavoidable experimental artifact. A formal treatment of these effects alone will be the subject of the next section. We will now discuss the rest of the factors and explain how they can usually be avoided by obvious precautions.

We first consider the effects associated to the experimental set-up itself. External vibrations and non-ideal motion, which causes line broadening, are made neglible by proper support of the spectrometer. Finite channel size effects are avoided by having a channel width much larger than the natural FWHM. Electronic dead time (or saturation) effects occur when the relevant count rate is larger than or the order of the reciprocal of the smallest instrumental dead time [14]; these would have seriously distorted our spectra if they were encountered. Given transducer motion, effective source proximity varies and nonflat backgrounds result. Folding procedures give flat backgrounds and we will detail the one we used later in Section 7.1. Source proximity also implies non-parallel incident γ-ray directions which, in turn, imply a spread of Doppler velocities for any given transducer velocity. The associated spectral distortions can sometimes be accounted for. Our analysis assumes parallel incident rays and uniform absorber thickness. Polarisation effects can be ignored on the basis that they become non-negligible only when somewhat thick monocrystal absorbers are used; all our experiments were conducted using random orientation powder absorbers.

Next comes the effects due to more fundamental reasons pertaining to the solid state. These are texture effects, static hyperfine parameter distributions (inhomogeneous broadening) and dynamic effects (homogeneous broadening). Texture effects are most often the principal source of quadrupole doublet asymmetry. They occur when the EFG principle axes are not randomly oriented with respect to the γ-ray direction. Texture does not affect the line positions and widths such that, with texture alone, the lines remain Lorentzian. We remove this source of quadrupole doublet asymmetry by using random orientation powder absorbers.

Dynamic effects are present in Mössbauer spectra when the hyperfine interactions vary on a time scale comparable to the intrinsic measurement time. The latter is the mean time during which the Mössbauer γ-ray interacts with the nucleus and is approximately equal to the natural FWHM divided by Planck's constant. Such effects are caused when hyperfine parameters fluctuate between those corresponding to different states. The Mössbauer spectra of a sample showing dynamic effects displays line broadening on all lines and intensity asymmetries of all quadrupole doublets. Spectra of this kind were not observed for any of our samples. We therefore assumed that the intrinsic measurement time was much larger than the hyperfine interaction fluctuation time. Thus dynamic effects could not be observed.

A situation with no dynamic effects corresponds to the case of static hyperfine parameter distributions. We believe this situation is most representative of a large class of material, including the silicate minerals which are the object of the present study. When static distributions of both quadrupole splittings and isomer shift occur and are correlated, as is most often the case, unequal line depths and widths result. From this effect alone, however, equality of the spectral area of the the two doublet lines is preserved in nontextured absorbers. Also, the lineshape of each line in the doublet will not only be not Lorentzian but will also, in general, be nonsymmetric about its minimum.

2.5 Treating effects due to absorber thickness

As γ-rays pass through an absorber, some are scattered, some are absorbed. So nuclei deeper within the absorber see a smaller γ-ray flux and hence absorb proportionately fewer photons. Furthermore, this effect is not uniform across a spectrum: the corresponding reduction in γ-ray flux is most important at energies corresponding to deep peaks in a spectrum and the areas of the deep peaks in a spectrum will be more attenuated than those of small peaks [15].

A complete discussion of the effects of absorber thickness on a spectrum is provided by Rancourt [14]. Within his article, Rancourt illustrates the effects of finite absorber thickness and shows that they must be considered if physical meaning is to be ascribed to area or intensity ratios.

In order to remove thickness effects from a spectrum, we can extract the total resonant absorber cross section from that spectrum. Since this cross section is free of the effects of absorber thickness, the process of obtaining it for a spectrum will be called "thickness-correction" as these cross sections appear to be thickness-corrected emission spectra. We describe this process in section 7.2 of this thesis. For consistency with fitting models developed in our laboratory, we then use these cross sections to generate thin-limit spectra that actually resemble absorption spectra. We also describe this procedure in section 7.2. Once we have obtained thin-limit spectra, we must then fit them with a correct model by solving the problems discussed in the previous section.

2.6 Accurate site populations

To measure the population of each (generalized) site in an absorber, we require a proper fitting model. Rancourt and Ping [13] developed a powerful approach for obtaining arbitrary-shape static hyperfine parameter distributions from thickness-corrected Mössbauer spectra. Each site has its own set of hyperfine parameters from which we can calculate the spectral area corresponding to it. We describe the above fitting model in section 7.3 of this thesis.

The resulting subspectral areas, A_i, are proportional to the product of their populations, p_i, with corresponding site-specific recoilless fractions (f-factors), f_i, such that:

$$Total\ \ Area = \sum_i A_i \propto \sum_i \ f_i\ p_i. \tag{2.22}$$

Royer [15] and Rancourt et al. [16] have made an extensive study of site-specific recoilless fractions in Fe-bearing trioctahedral micas. They found that synthetic annite samples as studied here had recoilless fractions equal for all sites. Consequently, the subspectral area of a given site is a direct measure of its population.

The uncertainty in the calculated populations is a result of the fitting procedure used to obtain statistically good fits. The fundamental problem resides in the fact that the solution obtained by least-squared minimization is usually not unique. This problem is particularly severe in cases like the present one, where considerable line (subspectral) overlap occurs.

Since we are mainly concerned with subspectral (i.e. site-specific) areas to obtain site populations, we must examine how these area trade off with each other. The surface of equivalent fits, in the space of dependant hyperfine parameters, represents the Mössbauer solution. Such a solution can always be mapped out completely by imposing fixed value on some of the dependant parameters. The latter process enables us to determine the uncertainty of each site population.

Chapter 3. Structure and Crystal Chemistry of Annite

3.1 Micas: structure and nomenclature

Micas are a large family of layer silicates. A common feature found in all micas is the basic composite layer (or TOT layer) composed of one octahedral (O) sheet sandwiched between two tetrahedral (T) sheets (see Figure 3.1). Within a T sheet, each individual tetrahedron is linked with neighbouring tetrahedra by sharing three corners (the basal oxygens) to form a hexagonal mesh pattern. The fourth tetrahedral corner (the apical oxygen) points in a direction normal to the sheet and is shared with an octahedron. The unshared O apices are individually occupied with single hydroxyl groups that are located below or above the center of the 6-fold T-rings. Normally, four oxygen ions and two hydroxyl groups form the apices of each individual octahedron. The octahedra are linked laterally by sharing octahedral edges.

Adjacent composite TOT layers are electrostatically bound to each other by the interlayer cations. The interlayer chemistry is dictated by the requirements of an overall charge balance. In micas, which have a relatively large negative layer charge, the interlayer consists of singly or doubly valent cations.

Various cations are found within both the octahedral and tetrahedral cages. The tetrahedral cages, being small, will hold nothing larger than Fe^{3+} ions. The cations which usually occupy the tetrahedral cages are: Si^{4+}, Al^{3+}, and Fe^{3+}. Every tetrahedral cage contains a cation.

Such is not necessarily the case with the octahedral cages. Dioctahedral micas have cations in two thirds of the cages, trioctahedral micas have cations in every octahedral cage. Cations which usually occupy the octahedral cages include Fe^{2+}, Fe^{3+}, Mg^{2+}, Al^{3+}, and others. Only trioctahedral micas were studied in this work,

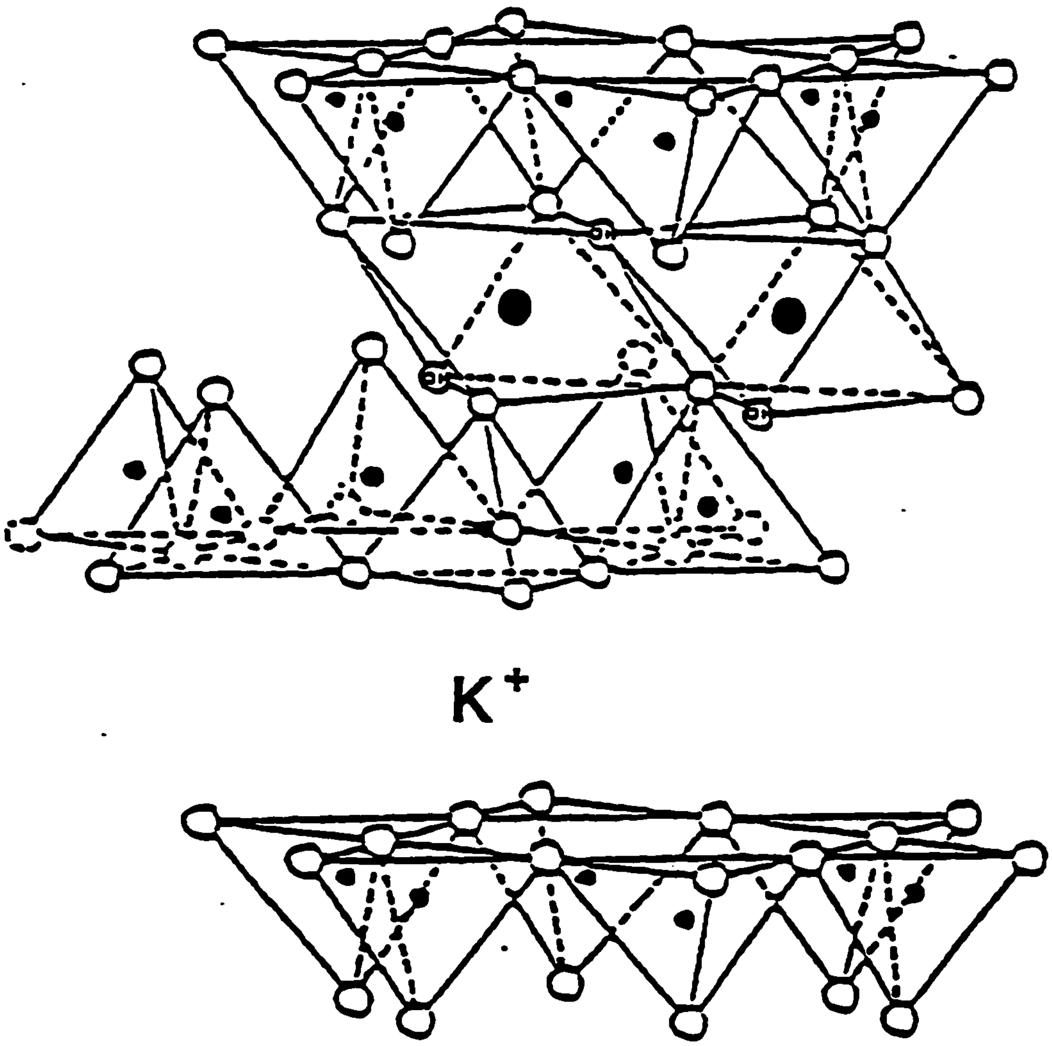

Figure 3.1: Mica structure. Large full circles are cations in O sites, small filled circles are cations in T sites, and open circles are oxygens. K^+ represents the interlayer cation content between adjacent TOT layer.

though the methods used could be applied to dioctahedral micas as well.

The field of trioctahedral micas with mostly Fe^{2+} and Mg^{2+} octahedral cations, mostly K^{+} interlayer cations, and tetrahedral stoichiometry of essentially Al^{3+}Si$_3^{4+}$, can be divided into species, based upon the iron content in the octahedral cages. Iron-deficient mica, Fe/(Fe+Mg)<0.33, are called phlogopite. Phlogopite may also refer to the end-member of this Fe-Mg field with only Mg in the octahedral cages. Biotite is the Fe-rich member of this iron solid solution, with Fe/(Fe+Mg)>0.33. The end-member, annite, should only contain Fe^{2+} in the octahedral cages, and Si and Al in the tetrahedral cages. For structural reasons this mineral cannot exist — to obtain a stable structure some of the iron content must be Fe^{3+} in either tetrahedral or octahedral cages (or both) and a corresponding number of hydrogen atoms must be lost. Such mica, which differs from ideal annite in this way, is called annite nonetheless.

3.2 Structure and crystal chemistry of annite

3.2.1 Ideal structure of annite

Annite is the Fe-rich end-member of the phlogopite-biotite-annite family. The structural formula of the solid solution is:

$$\{K^+\}\left[(Fe_x^{2+}Mg_{1-x}^{2+})_3\right]\left\langle Al^{3+}Si_3^{4+}\right\rangle O_{10}^{2-}(OH^-)_2 \tag{3.1}$$

where { }, [ ], and < > represent the interlayer, octahedral, and tetrahedral sites respectively.

Therefore, the ideal structural formula of annite is:

$$\{K^+\}\left[Fe_3^{2+}\right]\left\langle Al^{3+}Si_3^{4+}\right\rangle O_{10}^{2-}(OH^-)_2 \tag{3.2}$$

The ideal annite structure consists of an octahedral sheet completely filled with Fe^{2+} and a tetrahedral sheet filled at random with Al^{3+} and Si^{4+} in a 1:3 ratio.

3.2.2 Structural distortions and the real structure of annite

Because the apical oxygens of the tetrahedral sheets are shared with the octahedral sheet, the size matching of the two sheets is of critical importance in the formation of a stable composite layer structure. In a study of cation substitution in micas, Hazen and Wones [17] describe four structural distortions which can compensate for a size mismatch between the octahedral and tetrahedral sheets.

Of these mechanisms, the two which predominate are: (1) the compression of octahedra along the c-axis which stretches the octahedral sheet (Figure 3.2); and (2) the rotation of tetrahedra about their apex oxygens, which contracts the tetrahedral sheets (Figure 3.3). By geometrical considerations, we may relate both of these mechanisms to the in-plane b lattice parameter (denoted as b_m on Figures 3.2 and 3.3). We express the octahedral layer flattening and the tetrahedral sheet rotation, in terms of b, by the following equations [17]:

$$b = 4\sqrt{2} d_t \cos(\alpha) \tag{3.3}$$

$$b = 3\sqrt{3} d_o \sin(\psi) \tag{3.4}$$

where d_t is the average tetrahedral bond length, α is the tetrahedral rotation angle, d_o is the average octahedral bond length, and ψ is the octahedral layer flattening angle.

For the $AlSi_3$ tetrahedral sheet at RT it has been shown that d_t=1.643 Å [17]. This corresponds to a maximum value of b=9.294 Å. Hazen and Wones have also shown that since b depends on the average size of the octahedral cation, $AlSi_3$ tetrahedral sheets do not form stable compounds with octahedral sheets in which the average cation radius is greater that a certain critical radius, 0.76 Å. Since the radius of [Fe^{2+}] is 0.78 Å (which corresponds to b=9.35 Å), it is not possible to form the ideal annite structure.

It is however possible to form a structure with near-ideal annite stoichiometry by replacing some of the [Fe^{2+}] by [Fe^{3+}]. When substituted directly for Fe^{2+} in the octahedral sheet, Fe^{3+} (which has a radius of 0.63 Å in octahedral coordination) reduces the average b. If the Fe^{3+} is also exchanged with Al^{3+} in the tetrahedral

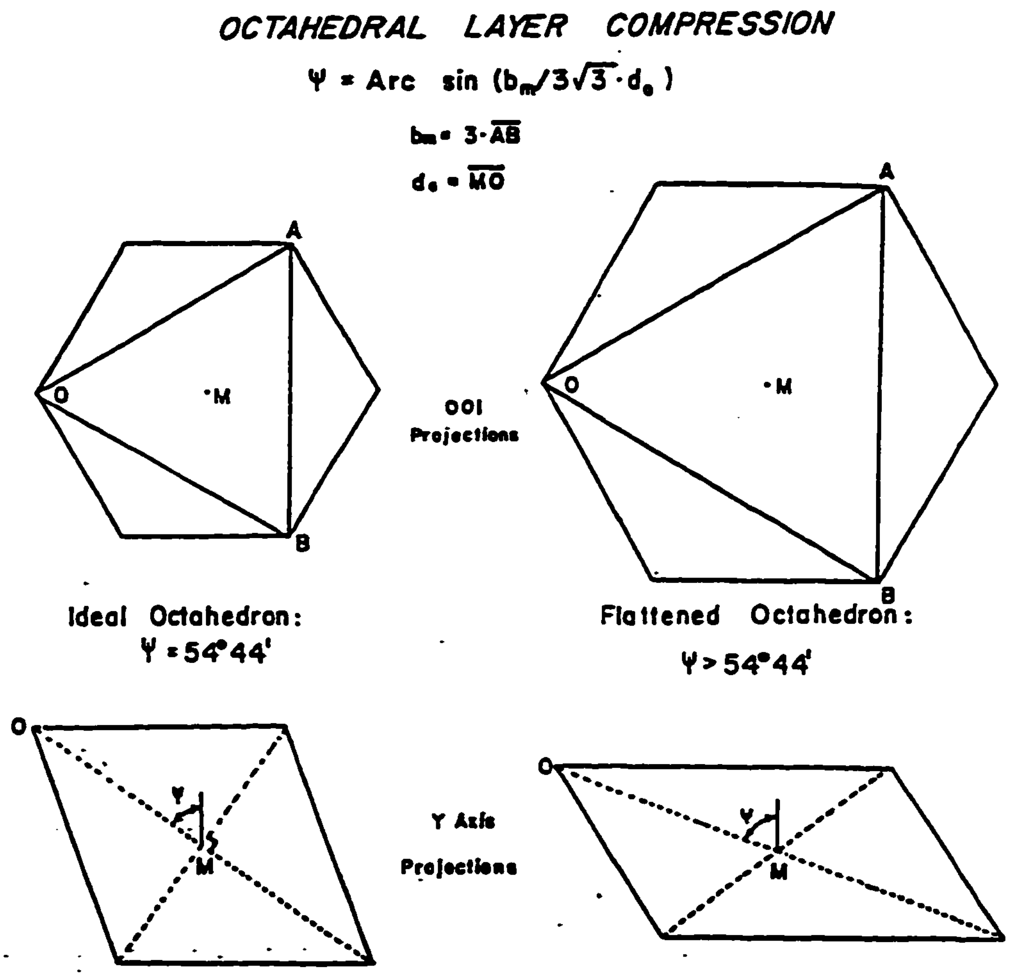

Figure 3.2: Expansion of the octahedral 001 projection by octahedral layer compression. From Hazen and Wones [17].

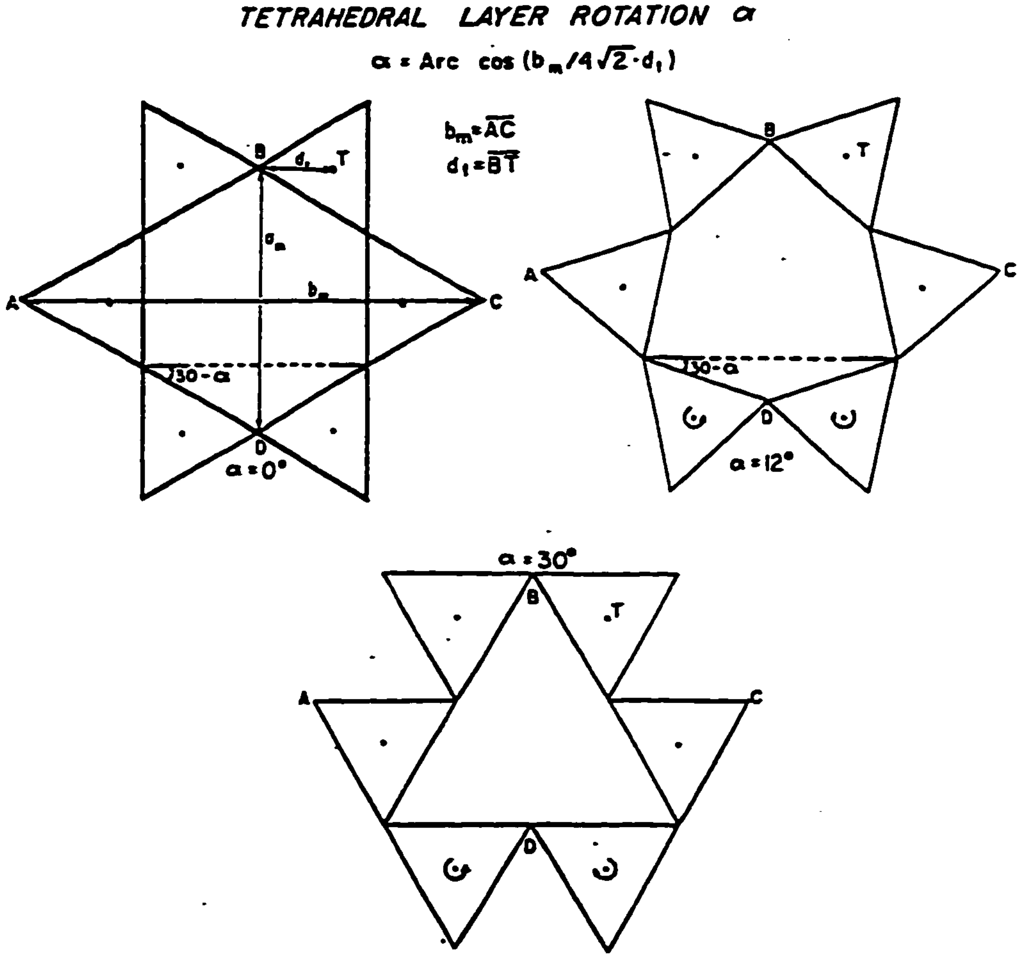

Figure 3.3: Contraction of the tetrahedral 001 projection by tetrahedral layer rotation. From Hazen and Wones [17].

sheet the average value of d_t is increased ($Fe^{3+}Si_3$ tetrahedral have d_t= 1.68 Å) and b is further reduced (since the radius of $[Al^{3+}]$ is 0.55 Å). Thus, if we assume no octahedral vacancies, the structural formula of real annite will be of the form:

$$K^+ \left[Fe^{2+}_{1-x-y} Fe^{3+}_{x} Al^{3+}_{y}\right]_3 < Al^{3+}_{1-3y} Fe^{3+}_{3y} Si^{4+}_{3} > O^{2-}_{10+3x+3y} (OH^-)_{2-3x-3y} \qquad (3.5)$$

The values of x and y are determined by the synthesis conditions. The matching of the tetrahedral and octahedral sheet places minimum values on x and y.

There are some important differences between the ideal annite structure and the real annite structure. The most obvious of these is the changing valence of some of the octahedral cages. This in turn results in changing anion stoichiometry as each octahedral cage occupied by a triply valent ion has one of its coordinating hydroxyl groups lose a hydrogen atom (to become O^{2-}) in order to maintain local charge balance, assuming no octahedral vacancies.

Another structural effect is the distortion of octahedra and tetrahedra to accomadate ions of differing sizes and valences. To illustrate the effect of these changes, let us consider the case of an octahedron occupied by an Fe^{3+} ion. The combined effect of the smaller ionic radius and larger valence of the Fe^{3+} ion cause the anions to contract around it. This distortion in turn causes slight expansion of the neighbouring octahedral cages containing Fe^{2+} ions. Thus, even small amounts of Fe^{3+} can affect the local environments of a large proportion of the Fe^{2+} ions.

Similarly, there will be some distortion of the tetrahedral layer to accomodate different sized cations. These distortions will be transmitted to the octahedral layer through the shared apex oxygens. In fact, such distortions would occur even in the ideal structure since Al^{3+} and Si^{4+} are also of different sizes and randomly distributed.

In summary, the net effect of cation substitutions necessary to form the real annite structure is that there are variations of the local environments in the octahedral and tetrahedral sheets throughout the crystal structure. It is these variations which are the physical origin of the quadrupole splitting distributions in each of the generalized sites. Each local environment gives rise to a single elemental quadrupole doublet such that the overall absorption lines are intrinsically broader. In the present work, we use a continuous distribution of quadrupole splittings to model the overall absorption doublets corresponding to each of the generalized sites. We believe the latter corresponds to the best physical model we can justify.

3.2.3 Mössbauer spectrum of a typical annite sample

As metioned above, Fe^{3+} can be found in either the tetrahedral cages, $<Fe^{3+}>$, or in the octahedral cages, $[Fe^{3+}]$. Fe^{2+} can only be found in the octahedral cages, $[Fe^{2+}]$. These are the three generalized sites of trioctahedral micas that can be distinguished by MS. To each site corresponds a quadrupole splitting distribution (QSD) that arises from the particular characteristics of the different local environments (anion positions, next near-neighbour postions, next near-neighbour ion types, etc.).

A Mössbauer spectrum illustrating the three generalised sites that are resolved by MS is shown below. Each site contributes two peaks to the spectrum. The corresponding subspectrum is therefore termed a doublet.

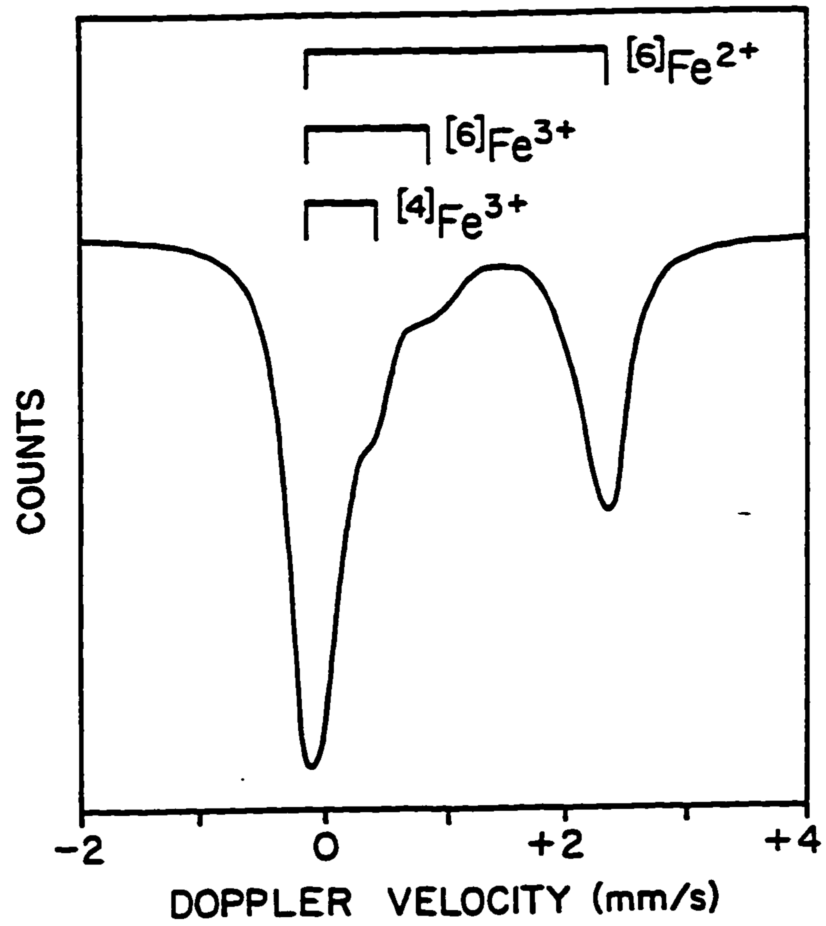

Figure 3.4: The Mössbauer spectrum of an annite at RT showing the approximate positions of the [Fe^{2+}], [Fe^{3+}], and <Fe^{3+}> sites.

Chapter 4. Structural Misfit Model for the Annite Mica

Simple structural crystal chemical models have a wide range of application in mineralogy. Hazen and Wones showed that this approach is needed to understand annite, where ferric ions occur to alleviate the octahedral sheet to tetrahedral sheet lateral mismatch that would destroy the structure if the large Fe^{2+} cations completely filled the octahedral cages [17]. Here, we generalize the lateral mismatch model to include: definite predictions on the individual $[Fe^{3+}]$ and $<Fe^{3+}>$ populations, cation size dependant octahedral flattening, and the effect of octahedral/tetrahedral sheet differential thermal expansion.

The in-plane b lattice parameter is a convenient measure of lateral extension and is given by the equations 3.3 and 3.4 of the preceeding chapter. In addition, RT values of b are found experimentally to be given by [17]:

$$b = A + B[R] \tag{4.1}$$

where A and B are constants and $[R]$ is the average octahedral cation radius calculated from the stoichiometry and tabulated radii [18]. Equation 4.1 can also be written as:

$$b = (A - BR_a) + Bd_o \tag{4.2}$$

where $R_a = 1.367$Å is the average RT anion radius for anions (4-coordinated O^{2-} and 3-coordinated OH^-) in the octahedral sheet.

In order to make equations 3.4 and 4.2 compatible with each other, we propose that slight octahedral flattening adjustments occur in a degree that depends on d_o as:

$$\sin(\psi) = \gamma/d_o + \beta \tag{4.3}$$

where $\gamma = (A - BR_a)/3\sqrt{3}$ and $\beta = B/3\sqrt{3}$. This is the lowest order Taylor expansion that makes equation 4.2 compatible with observation.

Also, the bond lengths vary with temperature as:

$$d_o(T) = d_{o_{RT}}(1 + \alpha_o(T - RT)) \tag{4.4}$$

where $d_{o_{RT}}$ is the average octahedral bond length, α_o is the thermal expansion coefficient for octahedral bonds, T is the synthesis temperature, and an analogous relation holds for the tetrahedral bonds. Here, $d_{o_{RT}}$ is given in terms of the real annite structural formula (equation 3.5) and tabulated RT bond lengths as:

$$d_{o_{RT}} = (1 - x - y)d_{o_{RT}}(Fe^{2+}) + xd_{o_{RT}}(Fe^{3+}) + yd_{o_{RT}}(Al^{3+}) \tag{4.5}$$

with an analogous expression for $d_{t_{RT}}$.

By substitution of equations 4.4 and 4.5 (and corresponding expressions for $d_t(T)$ and $d_{t_{RT}}$) and 4.3 into equations 4.1 and 4.2 and by equating 4.1 and 4.2, we obtain a linear relation between compositional parameters x and y that must be satisfied to achieve octahedral/tetrahedral sheet matching and bond sharing. The line defined by their relationship is given as:

$$\begin{aligned} x \;=\; & \left[\frac{\xi\cos(\alpha)\left(\frac{3}{4}d_{t_{RT}}(Si^{4+}) + \frac{1}{4}d_{t_{RT}}(Al^{3+})\right) - \gamma - \beta d_{o_{RT}}(Fe^{2+})}{\beta d_{o_{RT}}(Fe^{3+}) - \beta d_{o_{RT}}(Fe^{2+})}\right] + \\ & \left[\frac{\frac{3}{4}\xi\cos(\alpha)d_{t_{RT}}(Fe^{3+}) + \beta d_{o_{RT}}(Fe^{2+}) - \beta d_{o_{RT}}(Al^{3+}) - \frac{3}{4}\xi\cos(\alpha)d_{t_{RT}}(Al^{3+})}{\beta d_{o_{RT}}(Fe^{3+}) - \beta d_{o_{RT}}(Fe^{2+})}\right] y \end{aligned} \tag{4.6}$$

where $\xi = \frac{4\sqrt{2}}{3\sqrt{3}}$, $x = \frac{[Fe^{3+}]}{Fe_{tot}}$, and $y = \frac{<Fe^{3+}>}{Fe_{tot}}$. When $T > RT$, we renormalize as follows:

$$\begin{aligned} \beta &\mapsto \beta\,[1 + \alpha_o(T - RT)] \\ \xi &\mapsto \xi\,[1 + \alpha_t(T - RT)]. \end{aligned}$$

This relation (4.6) depends on the equilibration (or synthesis) temperature T, the tetrahedral rotation angle α (at T), and the thermal expansion coefficients α_o and α_t. In Chapter 9, we compare this relationship with the site population measurements we performed on nine synthetic annites equilibrated at different conditions.

Chapter 5. Sample Characterization

5.1 Synthesis description

In this study, measurements were made on nine synthetic annites crystallized under different equilibration temperatures and oxygen fugacity buffers (either graphite-methane (C-CH_4), or nickel-nickel oxide (Ni-NiO); see Table 5.1). Apart from sample HK-NNO, all equilibrations/syntheses were performed by R.G.Berman at the Geological Survey of Canada.

Sample	Temperature (°C)	P_{H_2O} (kbar)	Days	Mix	Buffer
HK-550	550	2	11	HK-NNO + H_2O	C-CH_4
HK-596	596	2	9	HK-NNO + H_2O	C-CH_4
HK-650	650	2	8	HK-NNO + H_2O	C-CH_4
HK-700	700	2	8	HK-NNO + H_2O	C-CH_4
HK-750	750	2	13	HK-NNO + H_2O	C-CH_4
HK-NNO	600	2	21	Robert	Ni-NiO
RB-25	700	2	14	Berman	C-CH_4
RB-22	750	2	14	Berman	C-CH_4
RB-7	700	2	7	Berman	Ni-NiO

Table 5.1: Synthesis condition for our annite samples.

Samples HK-550 to HK-750 are treated versions of sample HK-NNO — the starting mixture was composed of sample HK-NNO equilibrated by the C-CH_4 buffer at 2 kbar and 550, 596, 650, 700, and 750 °C, respectively. As for the other samples (RB-22, RB-25, RB-7), they were synthesized straight from stoichiometric mixtures of $KSi_3O_{6.5}$ glass, prepared by the method Schairer and Bowen [19], with iron oxalate ($FeC_2O_4 \cdot 2H_2O$), and γ-Al_2O_3 (denoted as mix Berman in Table 5.1).

The synthesis of HK-NNO was done by J.-L. Robert at Orléans by starting from a fine mechanical mixture of a specifically prepared silicate gel and a metallic

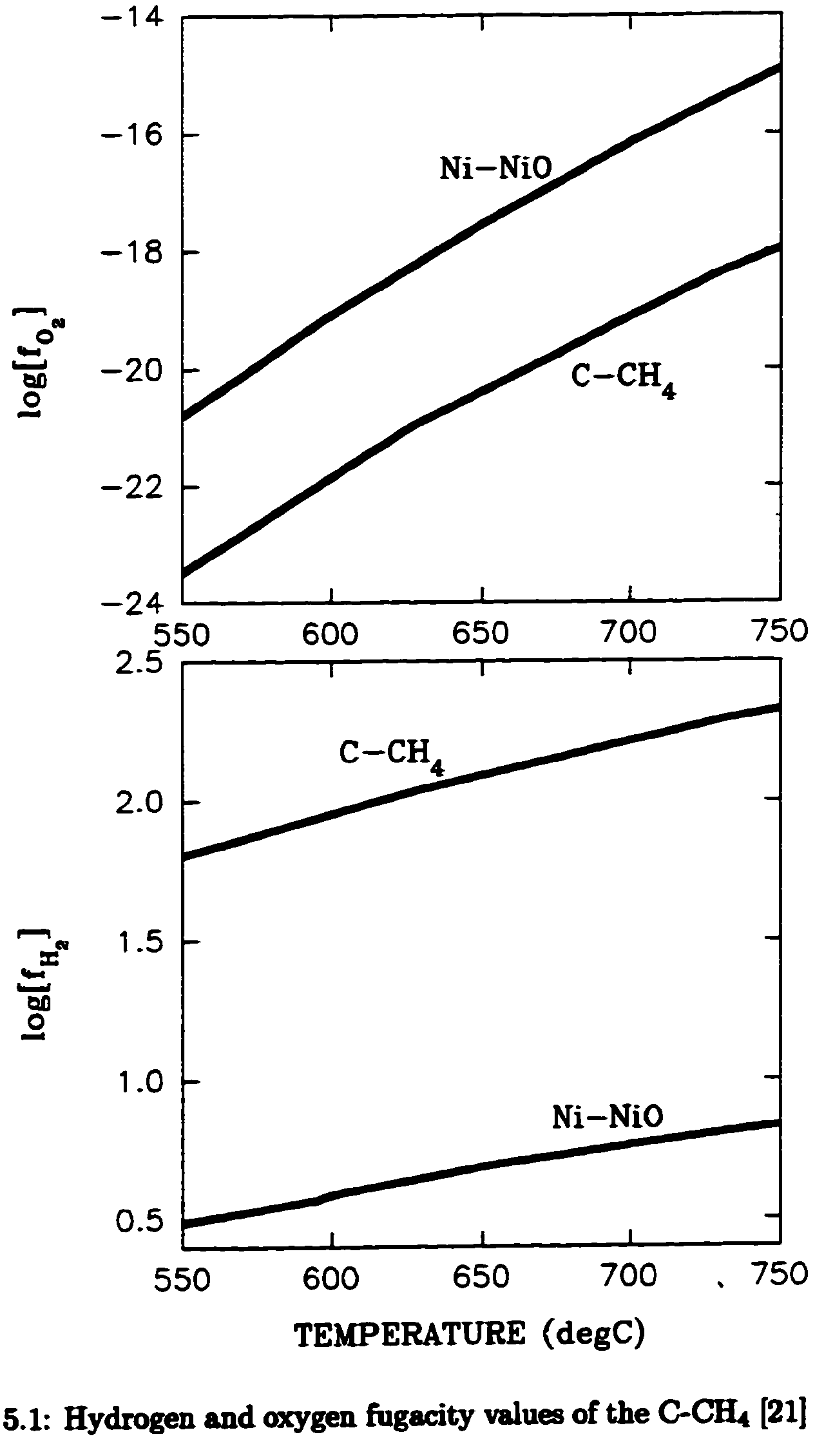

Figure 5.1: Hydrogen and oxygen fugacity values of the C-CH$_4$ [21] and Ni-NiO [22] buffers.

iron powder. The gel contained half of the Fe_{tot} and was prepared by the method of Hamilton and Anderson [20] using the following reagents: high-grade K_2CO_3 transformed into KNO_3 by reaction with HNO_3, a titrated nitrate solution of Al, a titrated nitrate solution of Fe, and tetraethylorthosillicate (T.E.O.S.) for silica. The starting mixture (denoted as mix Robert in Table 5.1) and 20% of distilled H_2O were sealed in a Pt tube by arc-welding. Full details concerning the synthesis of annite HK-NNO can be found elsewhere [16].

Hydrogen fugacity was buffered by the C-CH_4 [21] and Ni-NiO [22, 23] assemblages. No attempt was made to ascertain the attained hydrogen fugacity values which depend on the rate of H_2 diffusion out of the pressure vessels [24]. Under our experimental conditions, the C-CH_4 buffer sets higher hydrogen fugacities than the Ni-NiO buffer, at all temperatures (see Figure 5.1). Thus more reducing conditions are achieved by the C-CH_4 assemblage. In synthesizing annite, it is important to have the most reducing conditions possible in order to obtain the highest amount of Fe^{2+}.

However, due to structural constraints, there is nonetheless some Fe^{3+} that will be present in the sample. The reducing conditions vary with the equilibration temperature because the hydrogen fugacity of a given buffer is temperature dependent. In Figure 5.1, we present both the hydrogen and oxygen fugacity values of the buffers that we used as a function of the equilibration temperature.

Considering the increase in oxygen fugacity as temperature increases, one might expect an increase in the total Fe^{3+} content. Alternatively, the exact opposite is expected if we consider the behaviour of the hydrogen fugacity. Given that the hydrogen fugacities are ~20 orders of magnitude larger than the oxygen fugacities, we may conclude that the hydrogen fugacity is actually controlling the synthesis.

5.2 Scanning electron microscopy

The products of all runs were examined with a scanning electron microscope (SEM) to document the crystal size and form, and also to search for other phases. The SEM photomicrographs are shown in Figure 5.2 to 5.10.

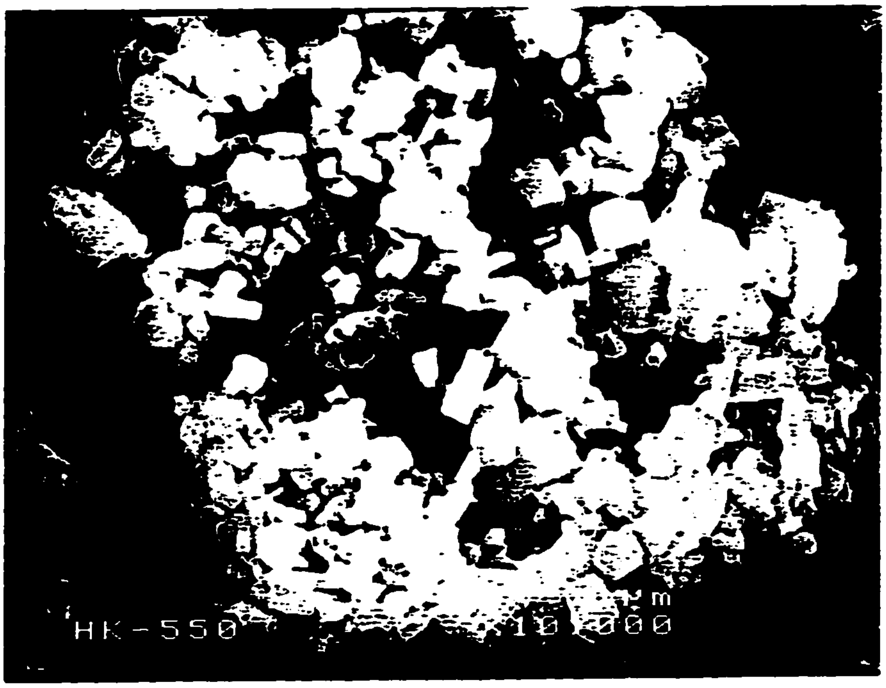

Figure 5.2: SEM photomicrograph of sample HK-550. Scale is as indicated by the white horizontal bar.

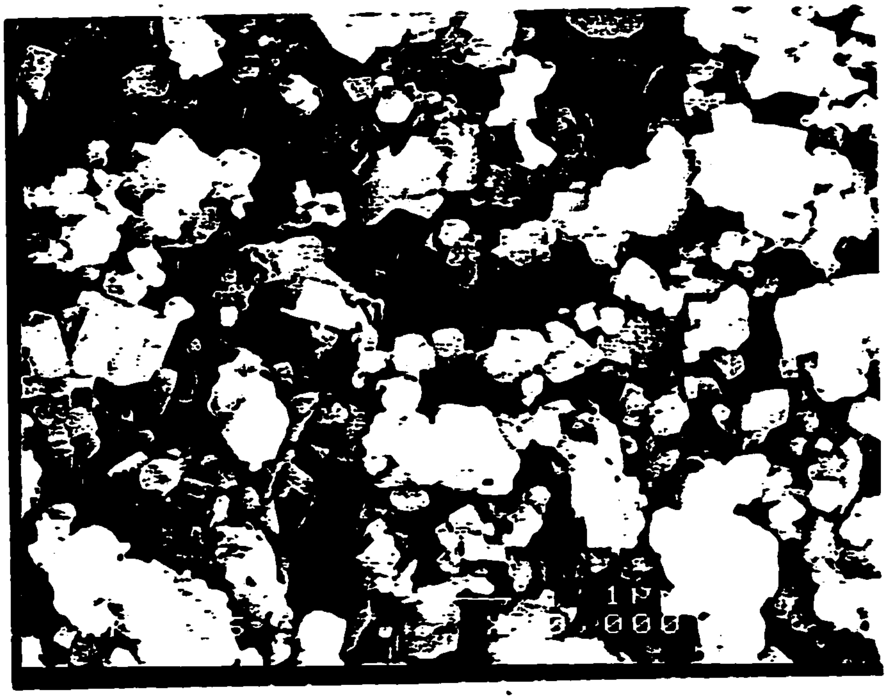

Figure 5.3: SEM photomicrograph of sample HK-596. Scale is as indicated by the white horizontal bar.

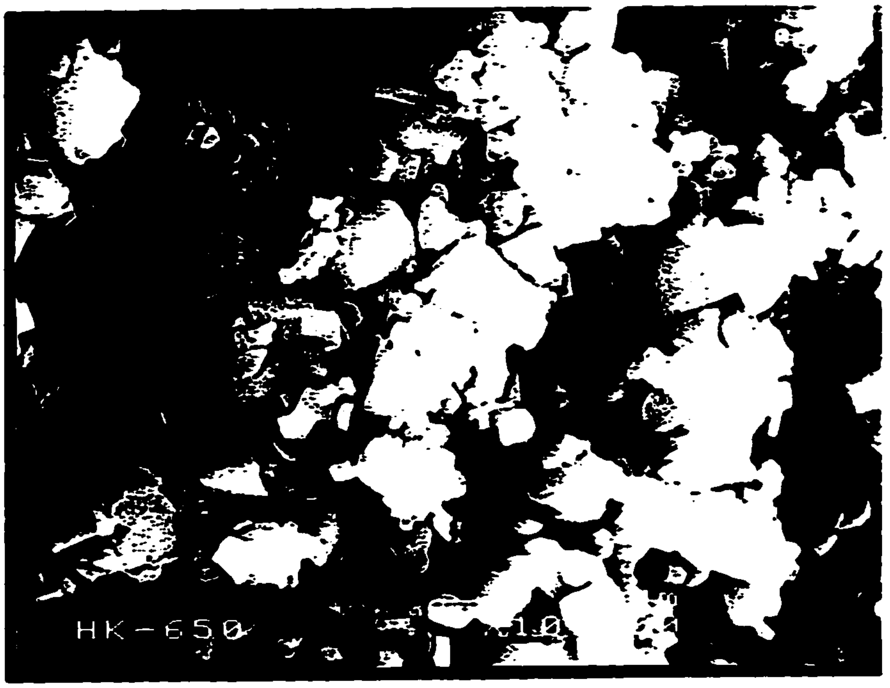

Figure 5.4: SEM photomicrograph of sample HK-650. Scale is as indicated by the white horizontal bar.

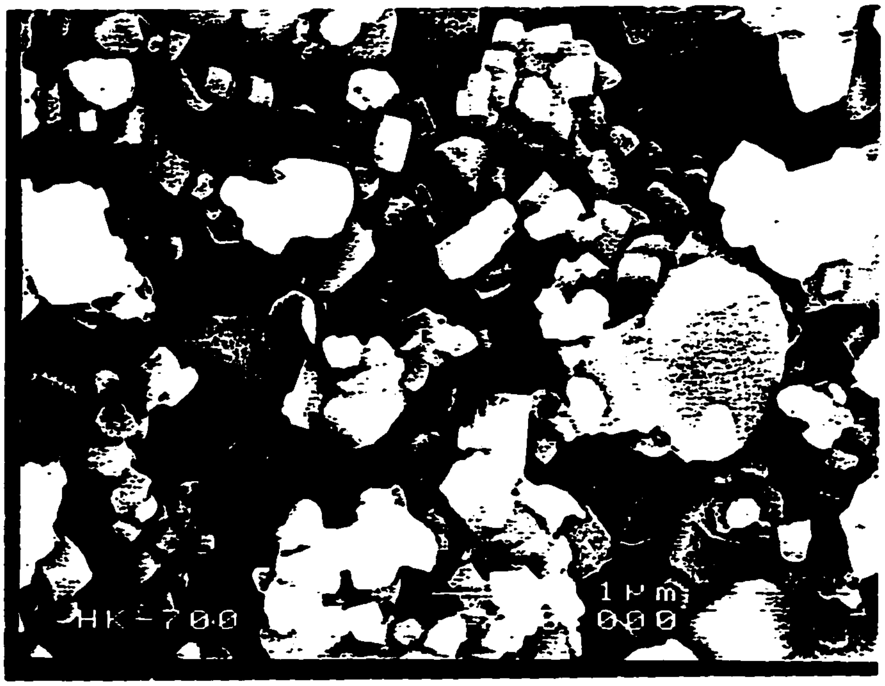

Figure 5.5: SEM photomicrograph of sample HK-700. Scale is as indicated by the white horizontal bar.

Figure 5.6: SEM photomicrograph of sample HK-750. Scale is as indicated by the white horizontal bar.

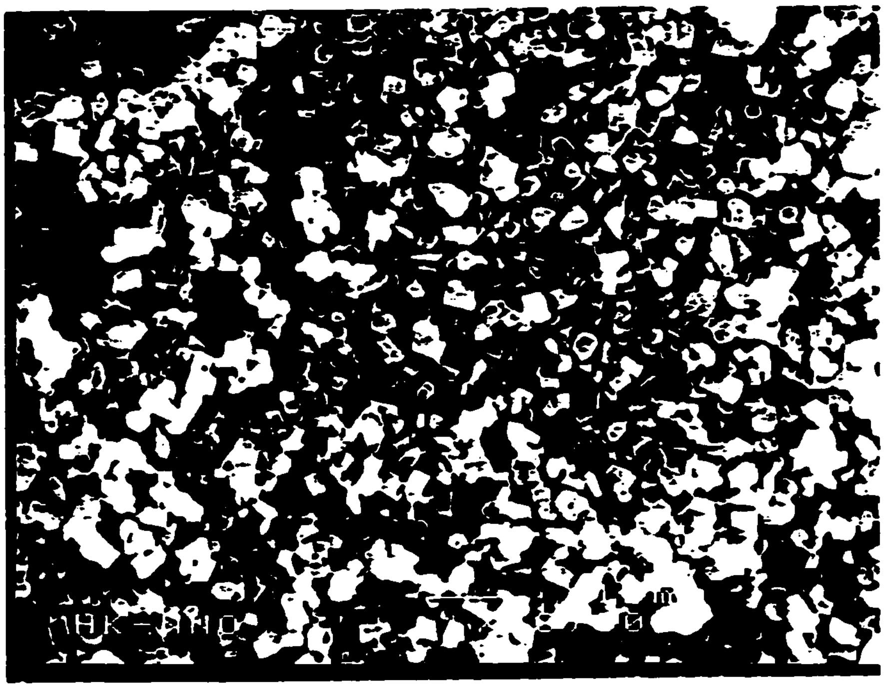

Figure 5.7: SEM photomicrograph of sample HK-NNO. Scale is as indicated by the white horizontal bar.

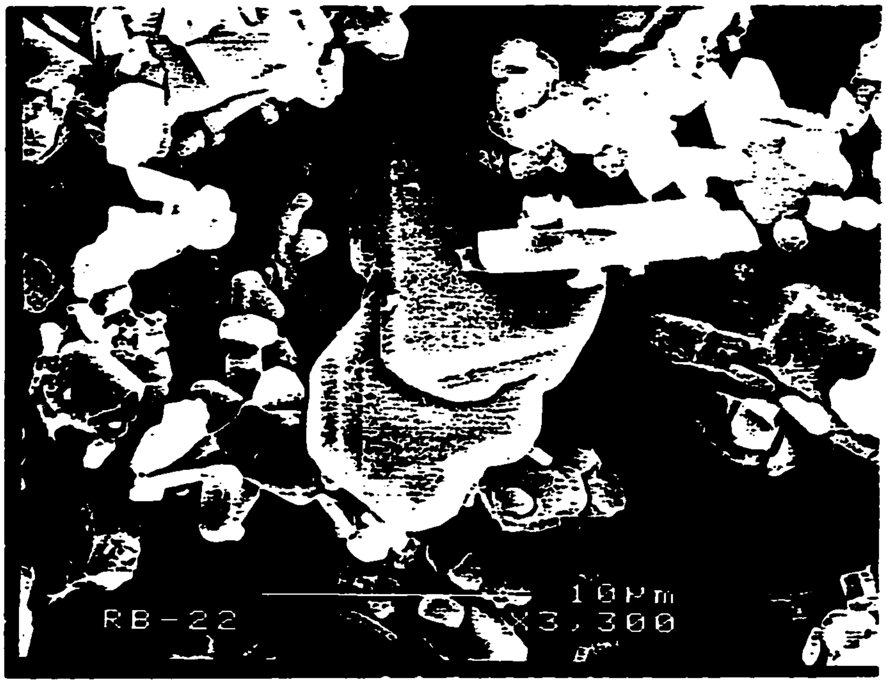

Figure 5.8: SEM photomicrograph of sample RB-22. Scale is as indicated by the white horizontal bar.

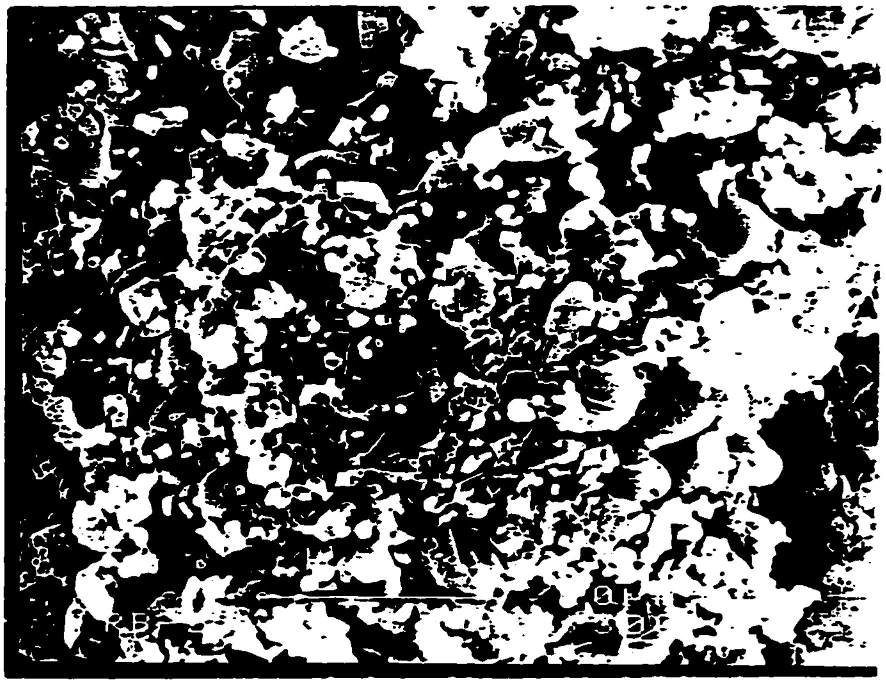

Figure 5.9: SEM photomicrograph of sample RB-25. Scale is as indicated by the white horizontal bar.

Figure 5.10: SEM photomicrograph of sample RB-7. Scale is as indicated by the white horizontal bar.

For samples HK-550 to HK-750, the average grain size increases with the equilibration temperature. The approximate grain size is 0.1–2 μm for sample HK-550 and of 0.4–5 μm for sample HK-750. This is consistent with diffusion increasing as the synthesis temperature increases.

Sample HK-NNO is very fine grained, with the largest crystals being typically 1–2μm across and the smallest being typically ~0.1 μm. As seen from the photomicrographs, the average grain size for sample HK-NNO is smaller compared to the rest of the HK-samples. This is as expected since sample HK-NNO was the starting material for equilibrations HK-550 to HK-750.

In the RB-samples we observe a bimodal distribution of grain size. There are grains with sizes ranging between ~0.2 and ~2 μm, others extend from ~3 to ~10 μm.

Using the energy dispersive spectrometer (EDS) available on the SEM, we were able to identify traces of sylvite (Syl), KCl, in the HK-samples and of fayalite (Fa), Fe_2SiO_4, and sanidine (Sa), $K(Si_3Al)O_8$, in the RB-samples. A better characterization of the associated phases will be provided by X-ray diffraction (Section 5.3).

5.3 X-ray diffraction

Powder X-ray diffraction (XRD) patterns were collected with a Philips X'Pert PW3710 automated powder diffractometer (CuK_α radiation, 40 kV/30 mA) for all the samples, except for sample RB-22 which was collected with a 114.5 mm Gandolfi camera using CoK_α radiation. The diffractograms are shown in Figures 5.11-5.18.

In the production of synthetic annite samples, it is important to ascertain whether the run product is a single phase. All diffractograms were searched for the presence of peaks from other phases that are known to occur or that can occur for the bulk starting conditions. The peaks belonging to these phases were indexed according to the International Center for Diffraction Data (ICDD) patterns listed in Table 5.2.

A detailed analysis of the XRD diffractograms of all samples was carried out to determine the amount of other phases present in the samples. The results of this analysis are tabulated in Appendix B of the present work. Table 5.3 summarizes

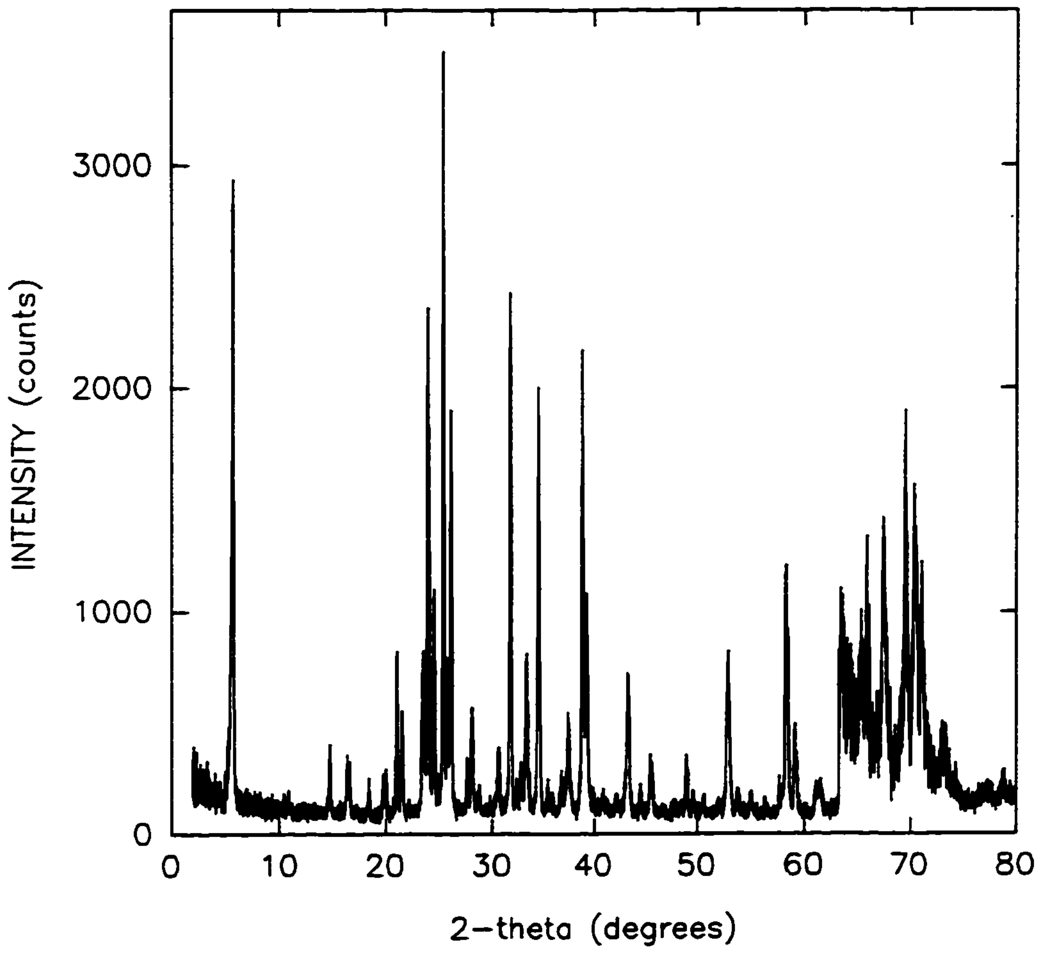

Figure 5.11: XRD powder diffractogram of sample HK-550.

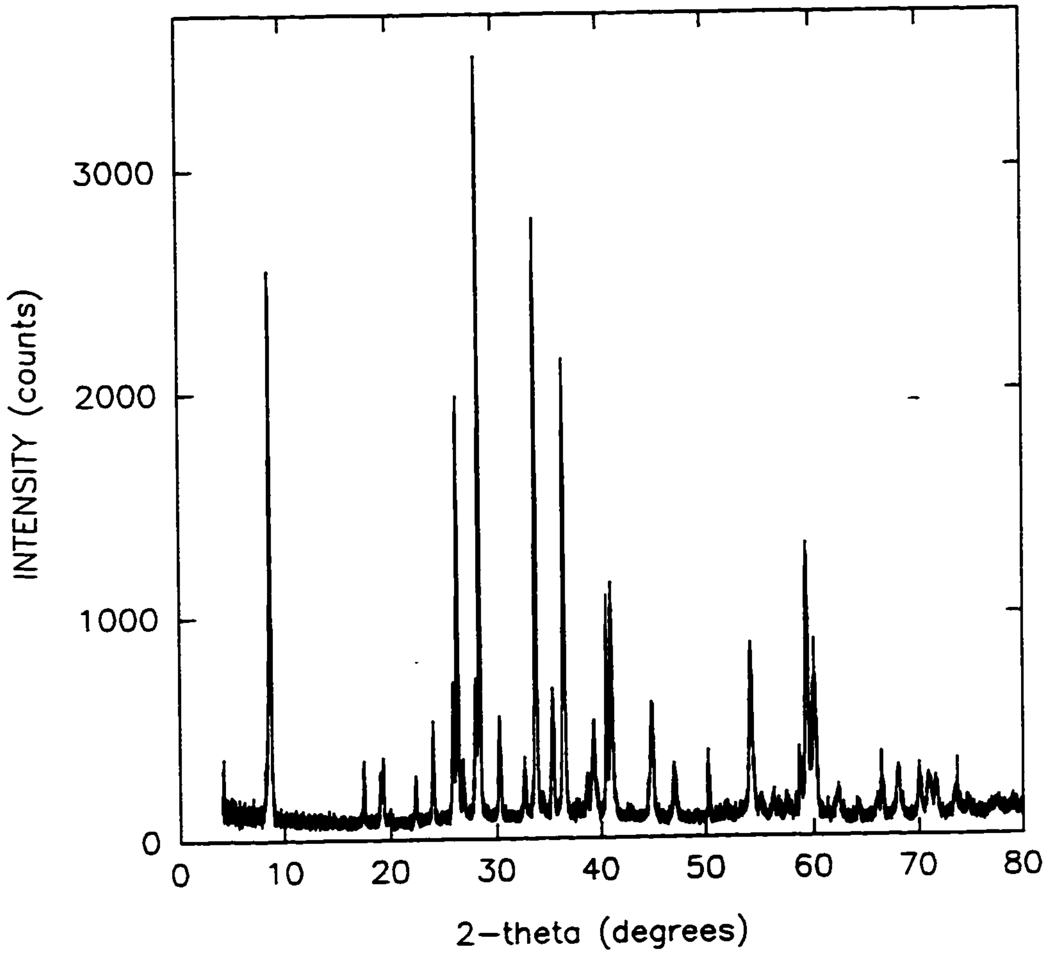

Figure 5.12: XRD powder diffractogram of sample HK-596.

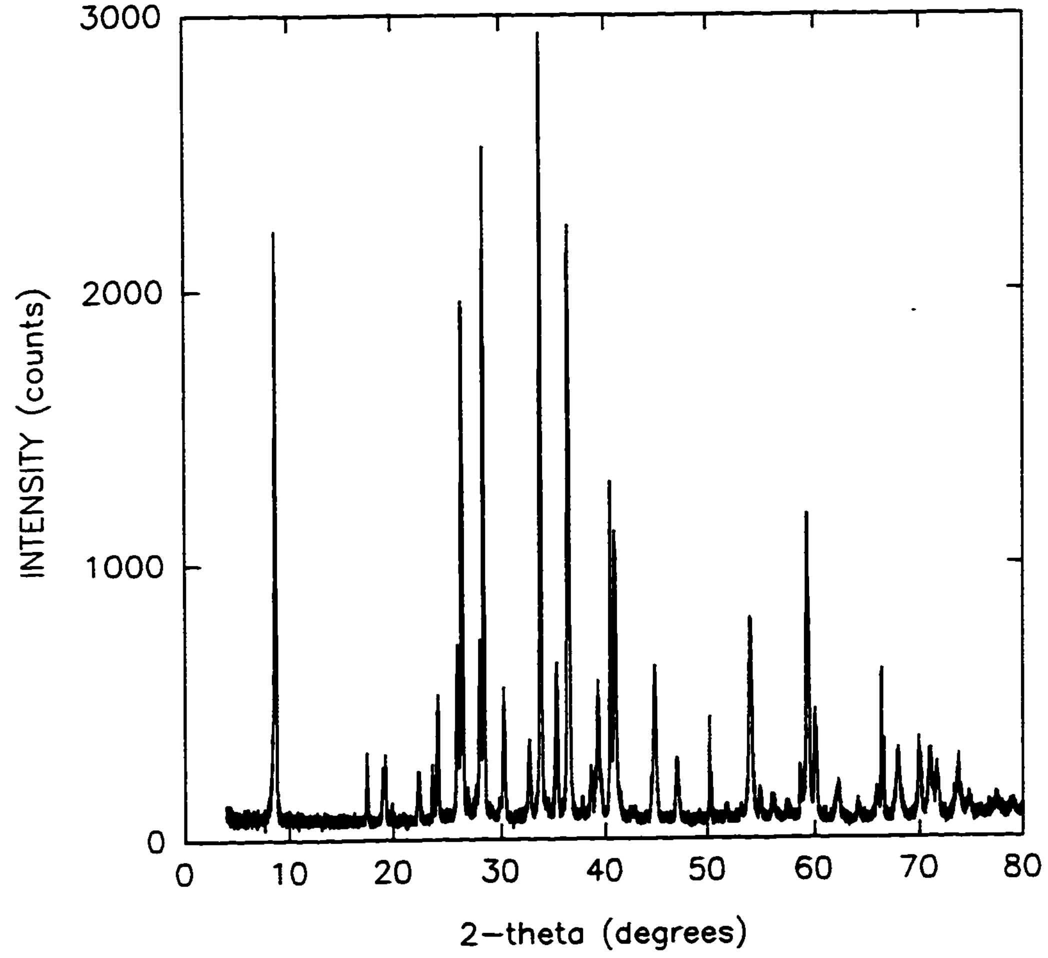

Figure 5.13: XRD powder diffractogram of sample HK-650.

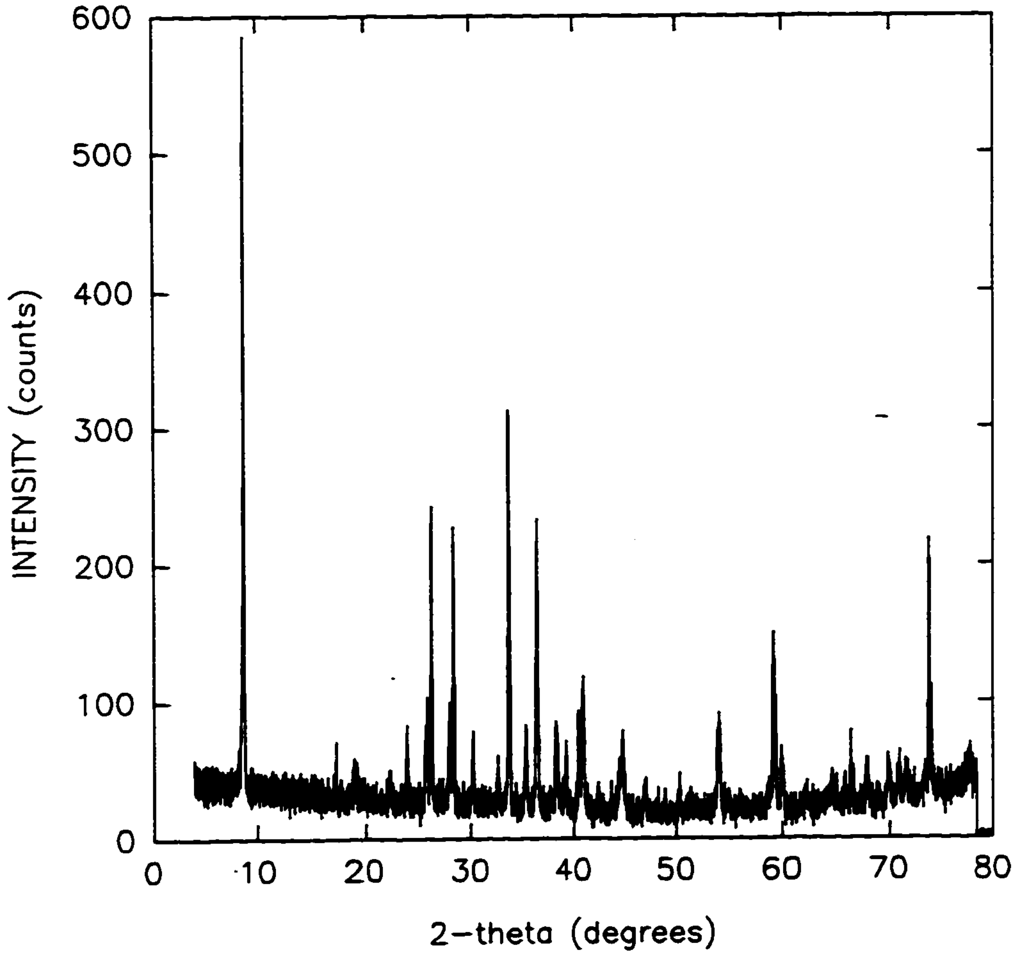

Figure 5.14: XRD powder diffractogram of sample HK-700.

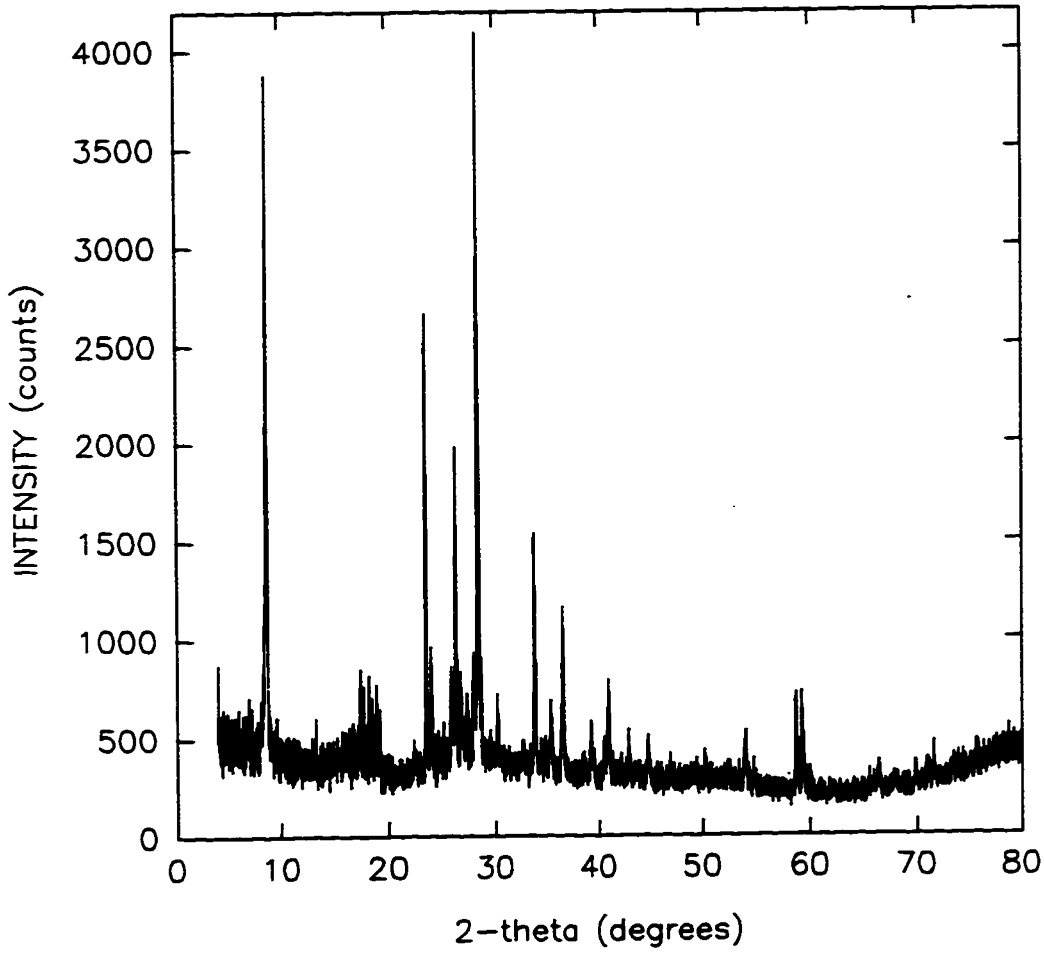

Figure 5.15: XRD powder diffractogram of sample HK-750.

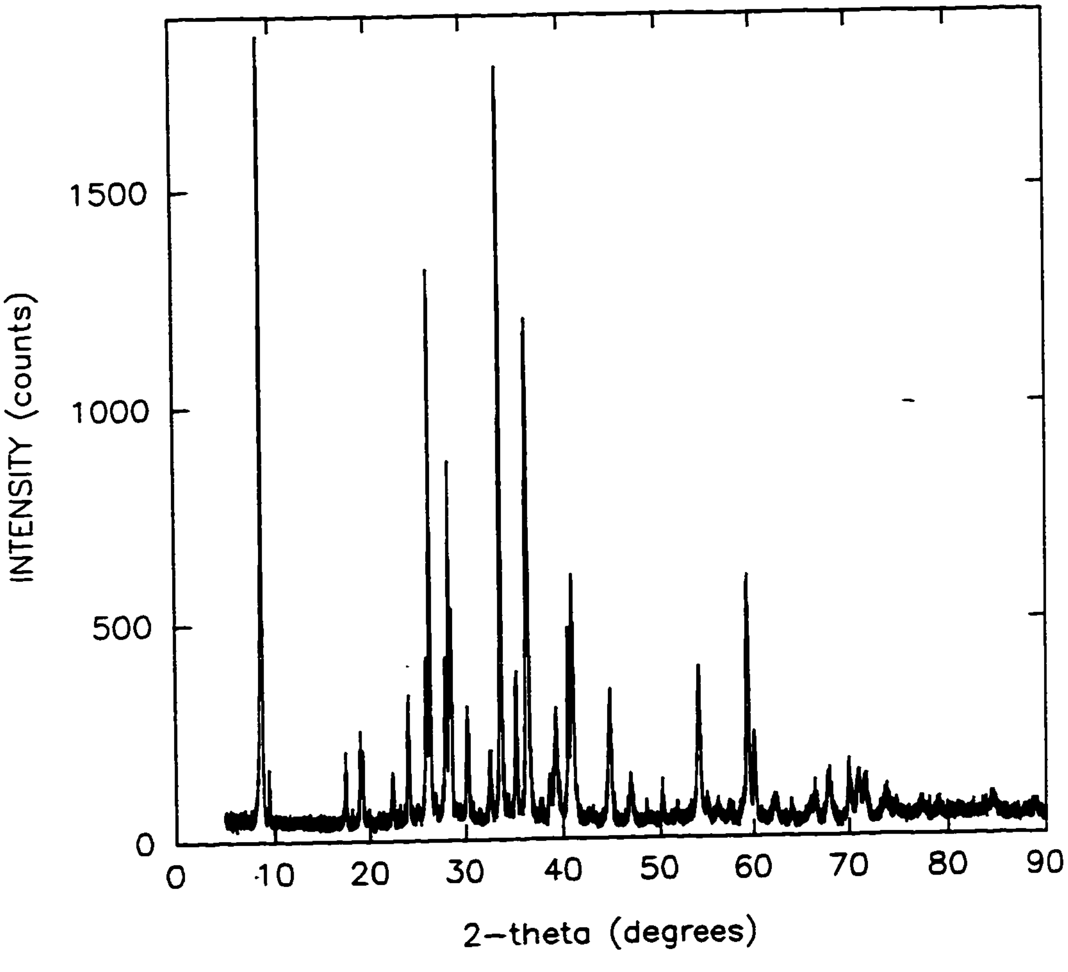

Figure 5.16: XRD powder diffractogram of sample HK-NNO.

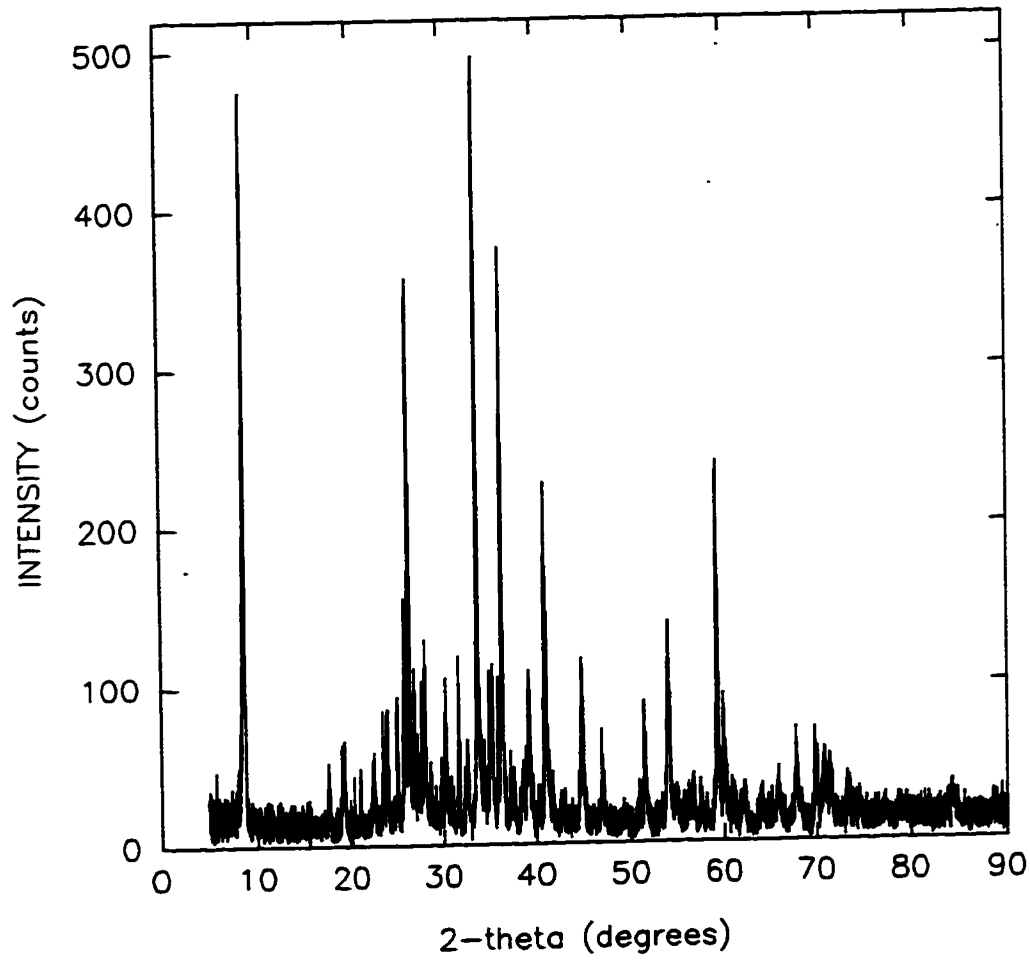

Figure 5.17: XRD powder diffractogram of sample RB-25.

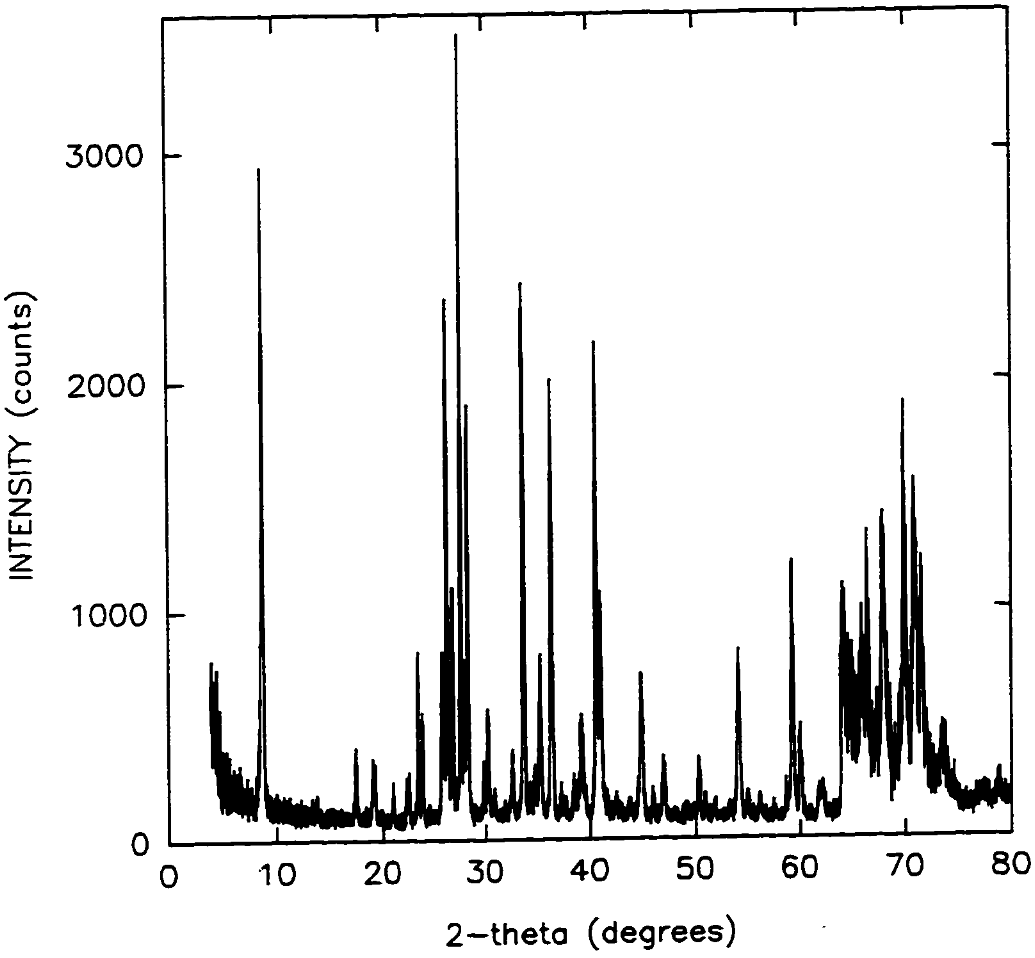

Figure 5.18: XRD powder diffractogram of sample RB-7.

(a)

Phase ICDD #	d-spacings (Å) and intensities of major reflections									
quartz 33-1161	3.34/X	4.26/2	1.82/1	1.54/1	2.46/1	2.28/1	1.37/1	1.38/1	2.13/1	2.24/1
magnetite 19-629	2.53/X	1.48/4	2.97/3	1.62/3	2.10/2	1.09/1	1.71/1	1.28/1	4.85/1	2.42/1
leucite 38-1423	3.27/X	3.44/7	2.84/4	5.38/4	2.92/3	2.81/2	2.37/2	3.51/1	2.64/1	2.07/1
kalsilite 11-579	3.12/X	2.58/5	3.97/5	2.18/2	2.47/2	4.35/1	2.43/1	2.22/1	1.57/1	1.49/1
hematite 13-534	2.69/X	1.69/6	2.51/5	1.84/4	1.48/4	1.45/4	2.20/3	3.66/3	0.91/3	1.31/2
clinoferrosil. 29-721	2.91/X	4.61/9	3.23/7	2.59/1	6.46/3	2.52/2	1.78/2	2.14/2	1.99/2	1.61/2
orthoferrosil. 17-547	4.62/X	2.91/9	6.48/7	3.24/7	3.34/4	2.75/2	2.60/2	2.51/2	2.30/2	2.13/2
hisingerite 26-1140	4.23/X	2.46/X	1.72/X	2.71/8	2.25/8	2.20/8	1.57/8	1.55/8	3.41/6	2.58/6
fayalite 34-178	2.50/X	2.83/9	1.78/8	1.77/7	3.56/6	2.57/5	2.63/3	1.52/3	2.41/3	2.62/2
sanidine 25-618	3.33/X	3.28/6	4.24/6	3.79/6	3.23/5	2.58/4	3.46/3	3.00/3	1.79/3	3.26/2
sylvite 4-587	3.15/X	2.22/6	1.82/2	1.41/2	1.28/1	1.57/1	1.05/1	0.84/1	0.95/1	1.11/1

(b)

Phase	Mineral symbol	Formula	Crystal system	Space group
quartz	Qtz	SiO_2	hexagonal	$P3_221$ or $P3_121$
magnetite	Mag	$Fe^{2+}Fe^{3+}_2O_4$	cubic	$F4/d\bar{3}2/m$
leucite	Lct	$KAlSi_2O_6$	tetragonal	$I4_1/a$
kalsilite	Kls	$KAlSiO_4$	hexagonal	$P6_3$
hematite	Hem	$Fe^{3+}_2O_3$	hexagonal	$R\bar{3}2/c$
clinoferrosil.	Fs	$Fe^{2+}Si_2O_6$	monoclinic	$P2_1$
orthoferrosil.	Fs (ortho)	$Fe^{2+}Si_2O_6$	orthorhombic	$P2_1/b\ 2_1/c\ 2_1/a$
hisingerite	?	$Fe^{3+}_2Si_2O_5(OH)_4\cdot 2H_2O$	monoclinic	?
fayalite	Fa	$Fe^{2+}_2SiO_4$	orthorhombic	$P2_1/b\ 2/n\ 2/m$
sanidine	Sa	$KAlSi_3O_8$	monoclinic	$C2/m$
sylvite	Syl	KCl	cubic	$F4/m\bar{3}2/m$

Table 5.2: (a) ICDD patterns of other phases which might have occurred in the run products. (b) Stoichiometric formulae of other possible phases.

the major conclusions that were drawn from the XRD analysis. Details concerning the experimental and analysis methods used for XRD are explained in Appendix B of the present work.

The XRD analysis revealed the presence of sylvite in all the HK-samples. Samples HK-550 and HK-750 also had sanidine. As for the RB-samples, they all contained minor amounts of fayalite and sanidine.

Sample	a (Å)	b (Å)	c (Å)	γ (degrees)	Volume (Å^3)	Content
HK-550	5.402(1)*	9.360(2)	10.325(2)	100.06(2)	514.0(1)	Ann; Sa (~40 %), Syl (<1 %)
HK-596	5.395(1)	9.346(2)	10.306(3)	100.07(3)	511.6(2)	Ann; Syl (<1%)
HK-650	5.398(1)	9.350(2)	10.311(3)	100.06(2)	512.5(1)	Ann; Syl (<1%)
HK-700	5.404(1)	9.362(2)	10.331(2)	100.05(2)	514.6(1)	Ann; Syl (<1%)
HK-750	5.403(1)	9.358(2)	10.317(3)	100.08(2)	513.6(2)	Ann; Sa (~30 %), Syl (<1%)
HK-NNO	5.399(1)	9.348(2)	10.329(2)	100.05(2)	513.3(1)	Ann; Syl (<1%)
RB-25	5.408(1)	9.366(1)	10.334(2)	100.05(2)	515.3(1)	Ann; Fa (~10 %), Sa (~10 %)
RB-22	5.405(2)	9.360(3)	10.344(3)	100.06(3)	515.3(2)	Ann; Fa (~30 %), Sa (~20 %)
RB-7	5.410(1)	9.369(2)	10.333(2)	100.05(5)	515.7(1)	Ann; Fa (~5 %), Sa (~5 %)

*Numbers in parentheses are standard errors and refer to the last digit.

Table 5.3: Summary of the XRD analysis.

Chapter 6. Experimental Methods for Mössbauer Spectroscopy

6.1 Equipment

In our experiments, RT (=22 °C) ^{57}Fe transmission Mössbauer spectra were collected using a 10 mCi ^{57}Co source in a rhodium matrix. During the decay process of ^{57}Co, ^{57}Fe nuclei in the first excited state are produced. These ^{57}Fe nuclei de-excite to produce the 14.4 keV γ-rays that may be absorbed by the ^{57}Fe nuclei present in our sample.

The spectrometer consisted of a Wissel DFG 1200 Mössbauer unit function generator operating in linear mode and a Wissel MDU Mössbauer drive unit connected to a Wissel MVT 1000 transducer. To input the required Doppler shift to the emitted γ-rays, the source was mounted on the MVT which covered a ±4 mm/s energy range.

A gas proportional counter was used to detect the γ-rays; the counter generates a signal proportional to the γ-ray energy. This signal is first amplified, then sent to a single channel analyser (SCA). The SCA acts as a filter, removing the pulses outside a certain energy window. Thus only pulses corresponding to the 14.4 keV Mössbauer transition were passed on to the multichannel scalar (MCS).

This MCS counted the pulses and placed these counts in 1024 channels, on a time basis. The MCS was synchronized to the transducer motion by means of the SYNC and CHannel ADVance from the DFG. In this way, we set the time base for the channel to cover a full period of the transducer with the 1024 channels.

The transducer operates in a constant acceleration mode and is driven by a symmetric saw-tooth velocity waveform. In this mode, the transducer moves toward the absorber with constant acceleration while the MCS accumulates counts over half the channels. Then, the transducer moves away from the absorber at constant acceleration, while the MCS counts over the other half of the channels.

Using this Mössbauer apparatus, we can acquire two 512-channel spectra during one Mössbauer experiment. These spectra are approximately mirror images of each others (one corresponding to increasing energy, the other to decreasing energy), except that their BGs are parabolic with opposite curvatures.

Because the distance between the transducer and absorber varies, there is a curvature in the BG of the two spectra. The closer are the transducer and the absorber, the higher is the BG. Alternatively, the farther are the transducer and the absorber, the lower is the BG. This effect is due to the fact that as the distance between the transducer and the absorber increases, there are proportionally fewer γ-rays that pass through the absorber. Thus, parabolic BGs are observed in the two halves of the spectrum.

These halves must be folded to obtain a flat background level and calibrated to obtain a precise energy (or velocity) scale. We used room temperature spectra on an ^{57}Fe enriched α-Fe foil for calibration. We will explain in further details the folding and calibration processes in section 7.1 of this thesis.

6.2 Absorber preparation

All the samples studied were powders. Uniform absorbers are required for thickness-effect corrections, so the following procedure was used. Approximately 20 mg of sample was spread evenly and sandwiched between two waxed paper sheets held with clear tape in aluminium holders with 5/16 inch diameter windows. The amounts of absorber that were used for each of the samples are given in Table 6.1.

Furthermore, because of the small particle size of these synthetic samples (see SEM photomicrographs, Section 5.2), such a procedure ensures that no texture is present in the absorbers [16].

Sample	Weight (±0.1 mg)	Area (cm^2)	Thickness (mg/cm^2)
HK-550	19.8	0.495	40.0
HK-596	20.0	0.495	40.4
HK-650	20.0	0.495	40.4
HK-700	20.0	0.495	40.4
HK-750	20.0	0.495	40.4
HK-NNO	19.7	0.495	39.8
RB-25	18.7	0.495	37.8
RB-22	19.7	0.495	39.8
RB-7	20.0	0.495	40.4

Table 6.1: Amounts of sample used for each of the holder and associated thicknesses.

Chapter 7. Data Treatment and Spectral Analysis Methods

7.1 Calibration and folding procedures

The experimental set-up used in our laboratory accumulates in 1024 channels of data two spectra that are approximately mirror images of each other, except that their backgrounds are parabolic with opposite curvatures. One spectrum corresponds to increasing energy; the other to decreasing energy. These spectra must be calibrated to obtain the precise energy (or velocity) scale and folded to obtain a flat background level.

Before and after each Mössbauer experiment, spectra of an ^{57}Fe enriched foil at room temperature (22 °C) were accumulated. These were used to calibrate the energy scale and to fold the mirror image spectra onto each other. Details concerning the calibration and folding procedures can be found in Appendix 1 of Royer's M.Sc. thesis [15].

7.2 Thickness corrections

7.2.1 Intrinsic resonant absorber cross section and the measured spectrum

In MS, the quantity that contains the desired (chemical, crystallographic, magnetic, morphological, etc.) information is the total normalized (and dimensionless, see below) resonant absorber cross section [25]:

$$\sigma_a' \equiv \sum_i \sigma_{a,i}'(E) \equiv \sum_i f_{a,i} n_{a,i} \sigma_{a,i}(E) \tag{7.1}$$

where i is an index that runs over the different sites in the absorber and $f_{a,i}$, $n_{a,i}$ and $\sigma_{a,i}(E)$ are site-specific absorber recoilless fractions (f-factors), ^{57}Fe/cm^2 thicknesses (in the Mössbauer sense), and intrinsic absorber resonant cross sections, respectively.

The latter intrinsic resonant cross sections are, by definition, normalized as

$$\int_{-\infty}^{+\infty} dE\, \sigma_{a,i}(E) = \frac{\pi}{2}\sigma_o\Gamma_o \qquad \forall i \tag{7.2}$$

where Γ_o is the natural FWHM of the Mössbauer transition, σ_o is the cross section at resonance for the Mössbauer transition, and $\forall i$ refers to all sites i. It follows that

$$\int_{-\infty}^{+\infty} dE\, \sigma'_{a,i}(E) = \frac{\pi}{2}\sigma_o\Gamma_o f_{a,i} n_{a,i} \qquad \forall i \tag{7.3}$$

and

$$\int_{-\infty}^{+\infty} dE\, \sigma'_{a}(E) = \frac{\pi}{2}\sigma_o\Gamma_o \sum_i f_{a,i} n_{a,i}. \tag{7.4}$$

We may now define a dimensionless thickness parameter, t_a, which will allow us to compare different absorbing samples. In the case of a single site material, the relevant normalized absorber cross section can be written as

$$\sigma'_a(E) = t_a\sigma_a(E)/\sigma_o = f_a n_a \sigma_a(E) \tag{7.5}$$

where

$$t_a = f_a n_a \sigma_o \tag{7.6}$$

is the thickness parameter. This factorization (Equation 7.5) is also possible in the case of multisite material, if we define $\sigma_a(E)$ as

$$\sigma_a(E) \equiv \frac{1}{\sum_i f_{a,i} n_{a,i}} \sum_j f_{a,j} n_{a,j} \sigma_{a,j}(E) \tag{7.7}$$

such that Equations 7.5 and 7.6 are valid where now

$$f_a \equiv \frac{1}{n_a} \sum_i n_{a,i} f_{a,i} \tag{7.8}$$

and, obviously, $n_a \equiv \sum_i n_{a,i}$.

One goal in applying MS is to obtain $\sigma'_a(E)$, to resolve it onto its site-specific components, $\sigma'_{a,i}(E)$, and, having the $f_{a,i}$, to obtain site populations from the areas (Equation 7.2).

The total resonant absorber cross section is, however, never observed directly. In absorption experiments, it gives rise to the measured absorption spectrum, $N(E)$. For uniform and nonpolarizing absorbers, $N(E)$ is given by the transmission integral [25]:

$$N(E) = BG + \eta_M f_s \frac{2}{\pi\Gamma_o} \int_{-\infty}^{+\infty} d\Psi \frac{\Gamma_o^2/4}{(\Psi + E)^2 + \Gamma_o^2/4} \cdot (e^{-\sigma_a'(\Psi)} - 1) \tag{7.9}$$

where BG is the measured background level, η_M is the part of the background that is both from recoilless and nonrecoilless Mössbauer γ-rays, and f_s is the recoilless fraction of the single-line thin source.

Few practitioners use the full transmission integral in analyzing their spectral data. Instead the thin absorber condition

$$\sigma_a'(E) \equiv \sum_i \sigma_{a,i}'(E) \equiv \sum_i f_{a,i} n_{a,i} \sigma_{a,i}(E) \ll 1 \qquad \forall E \tag{7.10}$$

is usually assumed. This assumption leads to the thin absorber expression for the measured spectrum

$$N_{th}(E) = BG - \eta_M f_s \frac{2}{\pi\Gamma_o} \int_{-\infty}^{+\infty} d\Psi \frac{\Gamma_o^2/4}{(\Psi + E)^2 + \Gamma_o^2/4} \cdot \sigma_a'(\Psi) \tag{7.11}$$

or

$$N_{th}(E) = BG - \eta_M f_s \frac{2}{\pi\Gamma_o} \sum_i f_{a,i} n_{a,i} \int_{-\infty}^{+\infty} d\Psi \frac{\Gamma_o^2/4}{(\Psi + E)^2 + \Gamma_o^2/4} \cdot \sigma_{a,i}(\Psi) \tag{7.12}$$

where one has performed a Taylor expansion of the exponential term in the integrand of the transmission integral.

This expression (Equation 7.12) has interesting properties that motivated its use. These are (1) each site-specific absorption (i.e., spectral area) is equal to $\pi\sigma_o\Gamma_o\eta_M f_s f_{a,i} n_{a,i}/2$ and is therefore directly proportional to the site population $n_{a,i}$, (2) subspectral areas are additive, such that the total spectral area is

$$\int_{-\infty}^{+\infty} dE[BG - N_{th}(E)] = \frac{\pi}{2}\sigma_o\Gamma_o\eta_M f_s \sum_i f_{a,i} n_{a,i} \tag{7.13}$$

and (3) if $\sigma_a^{'}(E)$ is a sum of Lorentzian lines (or a continuous distribution of Lorentzian lines, as in the case of the Voigt line shape) then the corresponding measured spectrum consists of the same sum (or distribution) but with each Lorentzian FWHM increased by the source line width Γ_o.

If the thin absorber condition (Equation 7.10) is not sufficiently satisfied, then one cannot take advantage of the thin absorber expression (Equations 7.11, 7.12) or make use of any of its properties. Instead, one must either fit directly with the transmission integral or deconvolute out $\sigma_a^{'}(E)$ from the measured data.

7.2.2 Obtaining the intrinsic resonant absorber cross section by deconvolution methods

To extract the intrinsic resonant absorber cross section from a spectrum in which line overlap occurs, Rancourt [14] argues that the measured spectrum must be deconvoluted since fitting with the transmission integral (Equation 7.9) is prohibitively inefficient.

To accomplish this task, Rancourt suggests a process by which a statistically perfect fit (i.e. where there are only small fluctuations of random sign between data and fit) of an arbitrary number of Voigt lines to a spectrum can be used to obtain the absorber cross section for that sample.

When fitting with k Voigt lines, the perfect fit result is expressed as:

$$N(\psi) = BG - \sum_k V(h_k, \gamma_k, \sigma_k, w_k; \psi) \tag{7.14}$$

where $h_k, \gamma_k, \sigma_k, w_k$ are, respectively, the Lorentzian height, the Lorentzian FWHM, the Gaussian width and the Voigt line position of the individual k-th Voigt line. The Voigt line shape corresponds to a Gaussian distribution of Lorentzian line positions and is able to reproduce intermediate shapes between the pure Lorentzian and Gaussian forms. It can be expressed as:

$$V(\psi) = \int_{-\infty}^{+\infty} dz G(z) L(\psi - z), \tag{7.15}$$

where

$$G(z) = \frac{1}{\sqrt{2\pi}\sigma} exp[-(z-w)^2/2\sigma^2] \tag{7.16}$$

and

$$L(\psi - z) = \frac{h\gamma^2/4}{(\psi - z)^2 + \gamma^2/4}. \tag{7.17}$$

The Gaussian is normalized to one such that the area of the k-th Voigt line is:

$$A_k = \frac{\pi h_k \gamma_k}{2} \tag{7.18}$$

No exact closed form analytic expression exists for $V(h_k, \gamma_k, \sigma_k, w_k; \psi)$, however analytic approximations [15] are sufficient.

The Fourier transform of the resulting sum of Voigt lines is known and the deconvolution follows immediately. The corresponding deconvolution result is expressed as [14]:

$$\sigma_a'(\Psi) = -\ln\left(1 - \sum_k \frac{\gamma_k}{\gamma_k - \Gamma_o} V(h_k/\eta_M f_s, \gamma_k - \Gamma_o, \sigma_k, w_k; \psi)\right). \tag{7.19}$$

A plot of $\sigma_a'(\Psi)$ versus ψ is essentially an emission spectrum corrected for the effects of sample thickness. Note that the normalization condition that the integral on both sides of Equation 7.19 be equal (i.e., that the total spectral area of both sides be equal) gives a relation between t_a and $\eta_M f_s$ such that only one needs to be known.

7.2.3 Generating a thin-limit spectrum

In the last subsection, we described how to perform a full thickness correction by the method of Rancourt [14] in order to obtain the intrinsic absorber cross section. We now use this cross section to generate a thin-limit spectrum with simulated Gaussian noise:

$$N_{th}(E) = BG - \eta_M f_s \frac{2}{\pi \Gamma_o} \int_{-\infty}^{+\infty} d\Psi \frac{\Gamma_o^2/4}{(\Psi + E)^2 + \Gamma_o^2/4} \cdot \sigma_a'(\Psi) + n_G(E) \tag{7.20}$$

and having the same background level as the original folded raw spectrum (i.e. the spectrum from which we extracted the cross section). The thin-limit spectrum, or thickness-corrected spectrum, is a simulation of what would be observed in the limit of zero absorber thickness. The Gaussian noise, $n_G(E)$, allows one to maintain the meaning of chi-squared in fitting the thin-limit spectrum.

7.3 Fitting model used for the determination of accurate site populations

7.3.1 Fitting model for arbitrary-shape quadrupole splitting distributions

Rancourt and Ping [13] have developed an approach for obtaining arbitrary-shape static hyperfine parameter distributions from thickness-corrected or raw Mössbauer spectra. The distributions are taken to be sums of Gaussian components and the corresponding spectra are shown analytically to be sums of Voigt lines.

In this work, we explained earlier (Section 3.2) that the three (generalized) sites present in micas each have their own quadrupole splitting distributions (QSDs). In this case, each QSD, $P(\Delta)$, is expressed as:

$$P(\Delta) = \sum_{i=1}^{N} p_i G_i(\Delta_{0i}, \sigma_{\Delta i}; \Delta), \tag{7.21}$$

where

- N is the chosen number of Gaussian components in the QSD
- Δ is the quadrupole splitting parameter as defined by Equation 2.16,
- p_i is the weight of the ith Gaussian component G_i,
- Δ_{0i} and $\sigma_{\Delta i}$ are, respectively, the center and Gaussian width of the ith Gaussian component of the QSD.

Each Gaussian component is defined by an expression similar to Equation 7.16 and

$$\int_{-\infty}^{+\infty} P(\Delta)d\Delta = \int_{-\infty}^{+\infty} G_i d\Delta = \sum_{i=1}^{N} p_i = 1, \quad \text{with } p_i > 0 \tag{7.22}$$

are the normalization conditions..

As stated earlier in Chapter 2, the elemental quadrupole doublet is the sum of two Lorentzian lines (Equation 2.17). Here we define it in a manner to include linear coupling between quadrupole splittings and center shifts, and the resulting expression for an elemental doublet is:

$$D(\nu) = \sum_{-1}^{+1} L_k(\delta_0 + \delta_1\Delta + k\Delta/2, \gamma, h_k; \nu), \tag{7.23}$$

where $k = -1$ labels the low energy line and $k = +1$ labels the high energy line. The arguments of the Lorentzian L_k are written in a manner similar as those in Equation 7.17.

Finally, δ_1 is the dimensionless coupling parameter of the center shift (CS), δ, to the quadrupole splitting (QS), Δ (i.e. $CS = \delta = \delta_0 + \delta_1\Delta$). Physically, the coupling arises through the effects of the crystal lattice on both the electronic density and EFG present at the nucleus.

The required Mössbauer lineshape is then formally given by:

$$Q(\nu) = \int_{-\infty}^{+\infty} D(\nu)P(\Delta)d\Delta \tag{7.24}$$

which, using Equations 7.23 and 7.24, can easily be shown to be equivalent to a sum of $2N$ Voigt lines:

$$Q(\nu) = \sum_{i=1}^{N} p_i \sum_{-1}^{+1} V_{ik}(\delta_0 + \delta_1\Delta_{0i} + k\Delta_{0i}/2, |\delta_1 + k/2|\sigma_{\Delta i}, \gamma, h_k; \nu). \tag{7.25}$$

where V_{ik} is represents the expression of a Voit line (see Equations 7.14 – 7.17). This expression requires $4 + 3N$ free parameters when fitting to the thickness-corrected spectra or $5 + 3N$ when fitting to the raw spectral data with unknown flat background level. EFG direction randomness reduces the fitting by 1 since $h_+ = h_-$, assuming an absence of asymmetry from the Goldanskii-Karyagin [14] effect. Note that Equation 7.22 reduces the number of required p_i by 1. In the case of thickness-corrected spectra, γ should not be considered a free parameter as its value is known from the uncertainty principle. This leaves $2 + 3N$ parameters for a perfect random absorber.

The resulting values of the $3N$ parameters p_i, Δ_{0i}, and $\sigma_{\Delta i}$ completely determines the arbitrary-shape QSD via Equation 7.21 for a coupling up to first order in Δ, between the CS and the QS (i.e., $CS = \delta = \delta_0 + \delta_1\Delta$). Taking this coupling to higher order does not allow a result in terms of Voigt functions and therefore represents one limit of the present method.

7.3.2 Relevance of a given fitting model

The potential correctness of a model for a spectrum or several spectra is judged by how well the theoretical lineshape can represent the experimental data. In this work, the quality of the fitting model is estimated by the value of the chi-squared (χ^2) function, which is given as [12]:

$$\chi^2 = \sum_k \left\{ \frac{[N(a_1, \ldots, a_j, \ldots, a_p; \Psi_k) - C_k]}{\sqrt{C_k}} \right\}^2 \tag{7.26}$$

where C_k is the number of γ-rays counted in the k-th velocity channel and $N(\vec{a}; \Psi_k)$ is the theoretical number of counts in channel k, which depends on the adjustable parameter vector $\vec{a}$. The experimental one-sigma error in absorption experiments is given as $\sqrt{C_k}$.

It is common practice to normalize the χ^2 such that we eliminate its dependance on the number of parameters fixed during the fitting process. The resulting number is called the reduced chi-squared (χ^2_{red}) and is defined by:

$$\chi^2_{red} = \frac{\chi^2}{v} \tag{7.27}$$

where v is the number of degrees of freedom for the model, equal to the number of channels of data less the number of free parameters.

A minimum value of χ^2 is found when the values of $N(\vec{a}; \Psi_k)$ and C_k are the closest together in the χ^2 sense. In general, an acceptable fit has a $\chi^2_{red} \approx 1$ (or $\chi^2 \approx v$), based on the idea that the χ^2_{red} is normally distributed about 1 with a standard deviation of $\sqrt{(2/v)}$ [26]. Consequently, a model having a χ^2_{red} value that is several standard deviations away from 1 implies that the particular model being tested is most probably incorrect.

7.3.3 Accurate site populations

In annite, we have three distinct iron sites: [Fe^{2+}], [Fe^{3+}], and <Fe^{3+}>. It has been shown that, in annite, the relevant recoilless fractions corresponding to each of these sites are equal within error and that, using the methods developed in this section, the [Fe^{2+}], [Fe^{3+}], and <Fe^{3+}> site populations can be evaluated with a precision of 0.2 % of Fe_{tot} [16].

To calculate a site population, we simply need to evaluate the subspectral area for that site. In the present work, both [Fe^{3+}] and <Fe^{3+}> required only $N = 1$ Gaussian component; however, the [Fe^{2+}] required $N = 3$ Gaussian components. The resulting fitting model is referred to as a 1-1-3 model.

As we mentioned earlier, this turns out to be a sum of Voigt lines. The subspectral area of each site is obtained from the Voigt lines that model that part of the spectrum. The area of a Voigt line is given by Equation 7.18. Assuming the γ_k is the same for all Voigts used in the model, the total area of the spectrum, A_{total}, is:

$$A_{total} = \frac{\pi}{2}\gamma \sum_{sites}^{3} \sum_{1}^{N} \sum_{k=\pm 1} h_k \tag{7.28}$$

and the subspectral area of ith site, A_i, is:

$$A_i = \frac{\pi}{2}\gamma \sum_{1}^{N} \sum_{k=\pm 1} h_k \tag{7.29}$$

where h_k is the height parameter of the kth Voigt line.

Through Equation 7.3, we may now relate the number of absorbing nuclei in the ith site, $n_{a,i}$, to the site-specific subspectral area, A_i. In annite, since the site-specific recoilless fractions are equal for all sites ($f_{a,i} = \bar{f} = 0.5$, [16]), the relative site populations are given by:

$$\frac{Fe_i}{Fe_{tot}} = \frac{n_{a,i}}{n_a} = \frac{\bar{f}}{f_{a,i}} \cdot \frac{A_i}{A_{total}} = \frac{A_i}{A_{total}} \tag{7.30}$$

where

$$n_a = \sum_i n_{a,i} \tag{7.31}$$

and the average recoilless fraction, $\bar{f}$, is equal to:

$$\bar{f} \equiv \frac{1}{n_a} \sum_i n_{a,i} f_{a,i}. \tag{7.32}$$

Equations 7.28, 7.29, and 7.30 are used to calculate the relative site populations of $[Fe^{2+}]$, $[Fe^{3+}]$, and $<Fe^{3+}>$.

Chapter 8. Results of the Mössbauer Analysis

8.1 QSD analysis of raw spectra

Even though raw spectra are altered by the line broadening associated to the effects of absorber thickness, we can still fit them with QSDs and extract meaningful information on the particular trends the data seem to have. We performed a QSD analysis (as described in section 7.3) of the raw spectra using a 1-1-3 model: one tetrahedral Fe^{3+} site having a QSD with one Gaussian component, an octahedral Fe^{3+} site also having one Gaussian component in its QSD, and an octahedral Fe^{2+} site with three Gaussian components in its QSD. The fit parameters for the raw spectra of all samples are given in Tables 8.1 and 8.2. Figures 8.1-8.5 present the spectra of all samples with fit and residual.

We characterize a given QSD by: the average QS, $\overline{QS}$; the QS value at which the probability is the largest, QS_{peak}; the difference $\mathrm{QS}_{peak} - \overline{QS}$; and the value of the standard deviation for the given QSD, σ_Δ. It is derived that the standard deviation is related to the component wise Gaussian width in such a way that if there are three Gaussian components used in the fit, as in the case of our Fe^{2+} QSDs, then the standard deviation is:

$$\sigma_\Delta = \sqrt{A_1(\Delta_{o1}^2 + \sigma_{\Delta_1}^2) + A_2(\Delta_{o2}^2 + \sigma_{\Delta_2}^2) + A_3(\Delta_{o3}^2 + \sigma_{\Delta_3}^2) - \overline{QS}^2} \qquad (8.1)$$

where A_k, Δ_{ok}, and σ_{Δ_k} are respectively the area, centroid, and Gaussian width of the kth Gaussian component. Also, $S_k \equiv \mathrm{QS}_{peak} - \overline{QS}$ is a measure of the skewness of the QSD: symmetric distributions have S_k=0 and highly skewed distributions have large (positive or negative) values of S_k.

Table 8.3 gives the characteristics for the Fe^{2+} QSDs for all raw spectra. When we compare the Fe^{2+} QSDs and characteristic parameters of the QSDs for all the samples, we cannot distinguish any particular trend in the QSDs. To illustrate this,

Sample $/BG$(MC/Ch)	Site	δ_0 (mm/s)	δ_1 (mm/s)	Δ (mm/s)	σ_Δ (mm/s)	h^+ (kC)	χ^2_{red}
HK-550	$< 3^+ >$	0.314	0.0^f	0.241	0.117	8.92	
	$[3^+]$	0.423	0.0^f	1.030	0.414	25.01	
	$[2^+]$-1			2.454	0.227	116.98	
	$[2^+]$-2			2.648	0.084	53.49	
0.585346	$[2^+]$-3	1.155	-.00960	2.157	0.851	48.22	1.17
HK-596	$< 3^+ >$	0.204	0.0^f	0.466	0.199	11.1	
	$[3^+]$	0.552	0.0^f	0.791	0.375	18.1	
	$[2^+]$-1			2.474	0.261	119.8	
	$[2^+]$-2			2.634	0.107	71.5	
0.624878	$[2^+]$-3	1.139	-.00326	2.194	1.020	48.4	1.28
HK-650	$< 3^+ >$	0.215	0.0^f	0.417	0.228	15.3	
	$[3^+]$	0.548	0.0^f	0.775	0.385	15.1	
	$[2^+]$-1			2.455	0.255	133.2	
	$[2^+]$-2			2.614	0.101	74.6	
0.752626	$[2^+]$-3	1.128	-.00151	2.142	1.027	54.1	1.47
HK-700	$< 3^+ >$	0.219	0.0^f	0.394	0.198	18.9	
	$[3^+]$	0.521	0.0^f	0.773	0.407	12.0	
	$[2^+]$-1			2.399	0.248	118.2	
	$[2^+]$-2			2.603	0.112	104.2	
0.852309	$[2^+]$-3	1.124	-.00085	2.098	1.025	58.3	1.40
HK-750	$< 3^+ >$	0.225	0.0^f	0.367	0.181	12.8	
	$[3^+]$	0.567	0.0^f	0.837	0.432	11.6	
	$[2^+]$-1			2.456	0.240	108.1	
	$[2^+]$-2			2.619	0.095	55.6	
0.634299	$[2^+]$-3	1.117	+.00216	2.208	0.776	51.6	1.10

^{f} This parameter was frozen during fit.
All fits impose Γ=0.2 mm/s and h_+/h_-=1.

Table 8.1: Fit parameters of raw ^{57}Fe Mössbauer spectra for the HK-NNO C-CH_4 annealed samples.

Sample $/BG$(MC/Ch)	Site	δ_0 (mm/s)	δ_1 (mm/s)	Δ (mm/s)	σ_Δ (mm/s)	h^+ (kC)	χ^2_{red}
HK-NNO	$< 3^+ >$	0.144	0.0^f	0.562	0.187	13.1	
	$[3^+]$	0.448	0.0^f	0.896	0.442	20.8	
	$[2^+]$-1			2.397	0.258	130.5	
	$[2^+]$-2			2.603	0.112	94.3	
0.725465	$[2^+]$-3	1.205	-.03042	2.208	1.132	60.6	1.50
RB-25	$< 3^+ >$	0.273	0.0^f	0.332	0.111	39.6	
	$[3^+]$	0.523	0.0^f	0.678	0.243	19.5	
	$[2^+]$-1			1.895	0.160	16.2	
	$[2^+]$-2			2.588	0.251	494.8	
1.456056	$[2^+]$-3	1.008	+.04485	2.095	1.242	122.6	12.43
RB-22	$< 3^+ >$	0.251	0.0^f	0.295	0.129	29.64	
	$[3^+]$	0.459	0.0^f	0.731	0.128	9.45	
	$[2^+]$-1			1.902	0.167	15.61	
	$[2^+]$-2			2.611	0.258	395.87	
1.259320	$[2^+]$-3	0.999	+.04435	2.000	1.265	73.17	8.15
RB-7	$< 3^+ >$	0.265	0.0^f	0.352	0.139	37.5	
	$[3^+]$	0.527	0.0^f	0.814	0.351	18.4	
	$[2^+]$-1			2.081	0.137	16.2	
	$[2^+]$-2			2.557	0.204	271.0	
0.858975	$[2^+]$-3	1.057	+0.02537	2.193	0.988	84.1	4.81

^{f} This parameter was frozen during fit.
All fits impose Γ=0.2 mm/s and h_+/h_-=1.

Table 8.2: Fit parameters of raw ^{57}Fe Mössbauer spectra for the samples synthesized straight from stoichiometric mixtures.

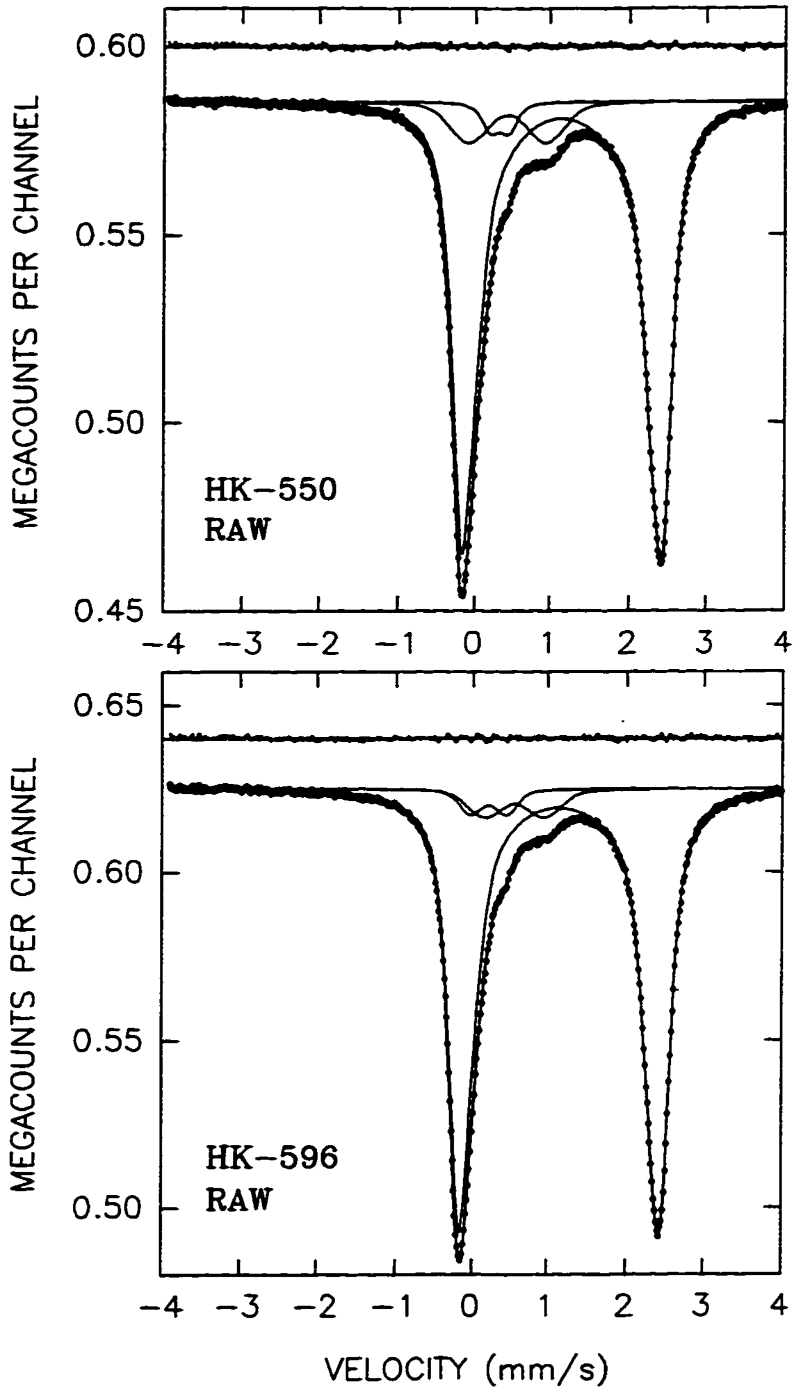

Figure 8.1: Raw spectra of synthetic annite HK-550 (top) and HK-596 (bottom) with fits and residuals.

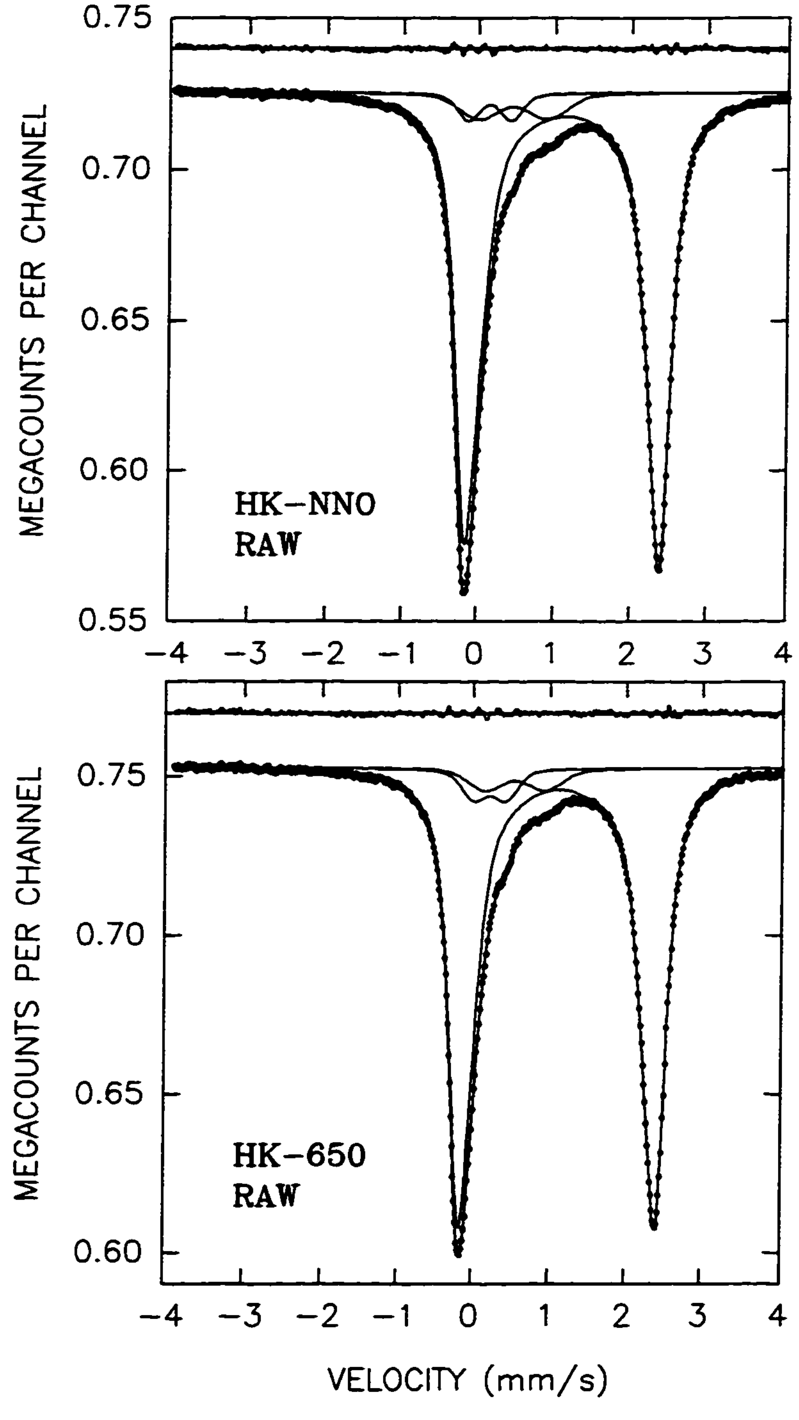

Figure 8.2: Raw spectra of synthetic annite HK-NNO (top) and HK-650 (bottom) with fits and residuals.

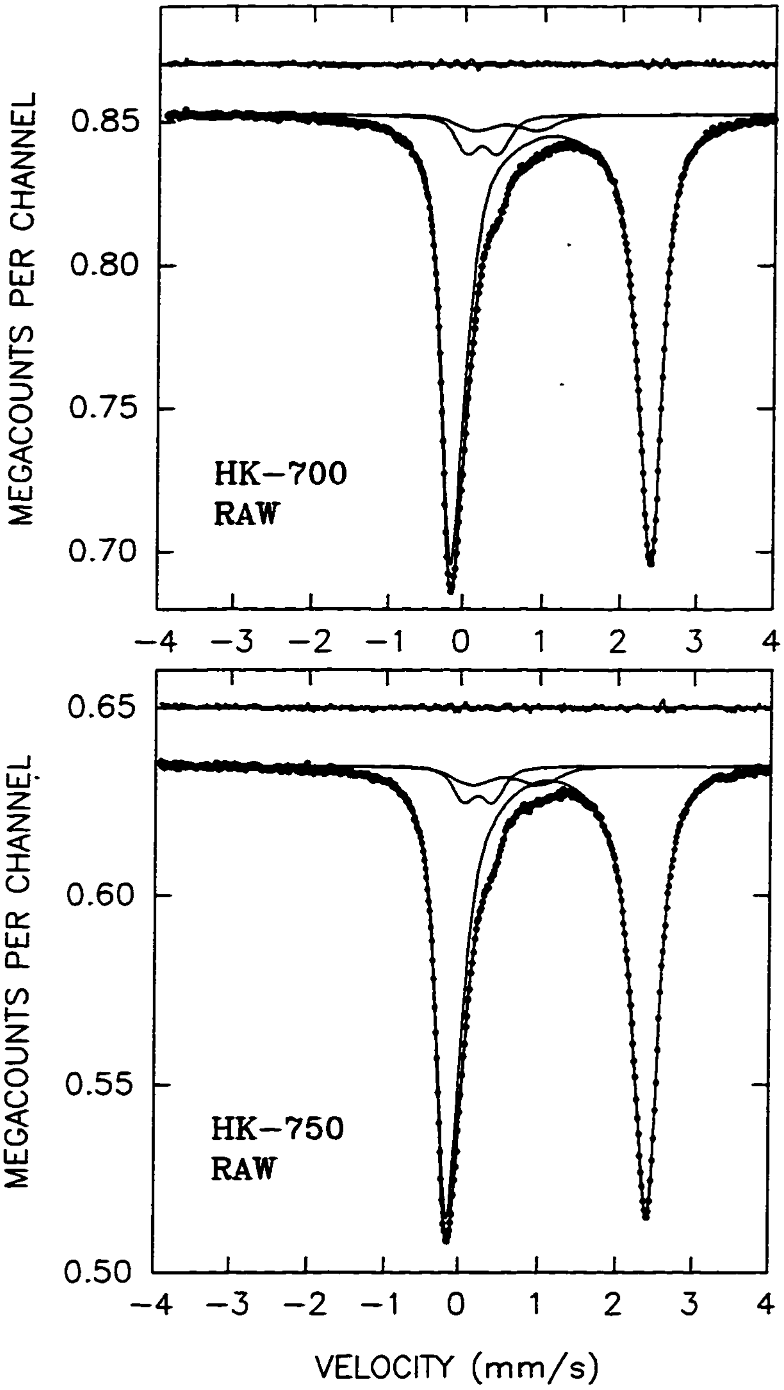

Figure 8.3: Raw spectra of synthetic annite HK-700 (top) and HK-750 (bottom) with fits and residuals.

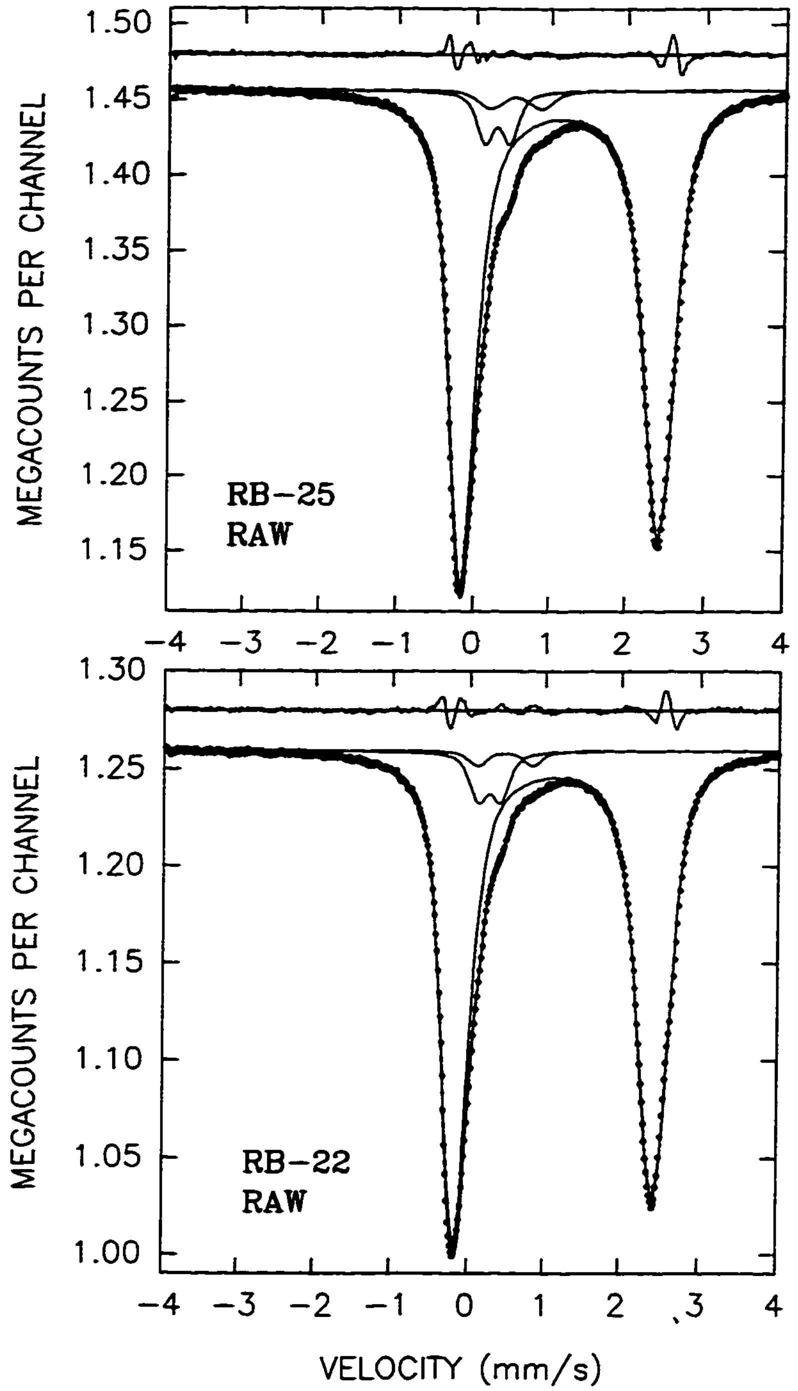

Figure 8.4: Raw spectra of synthetic annite RB-25 (top) and RB-22 (bottom) with fits and residuals.

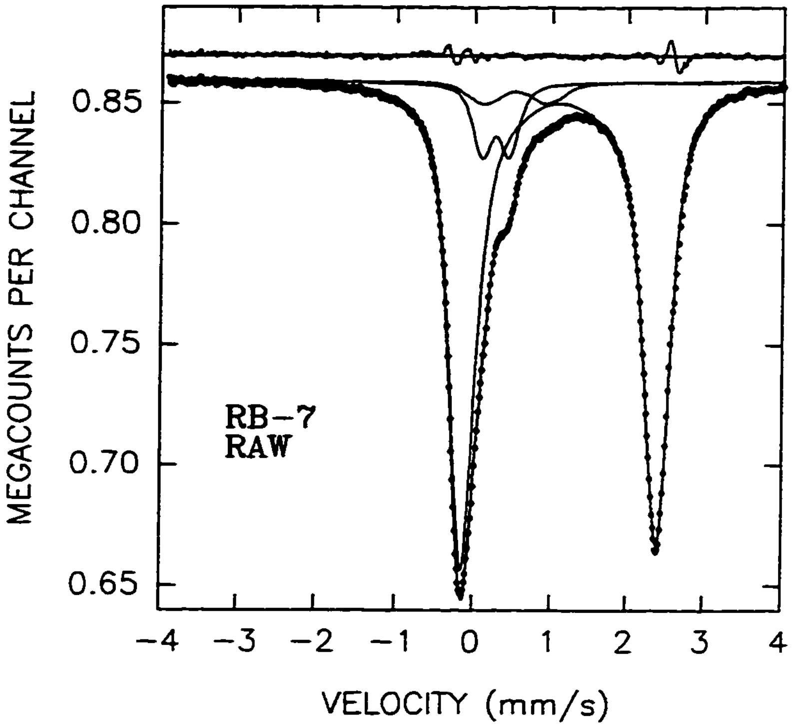

Figure 8.5: Raw spectrum of synthetic annite RB-7 with fit and residual.

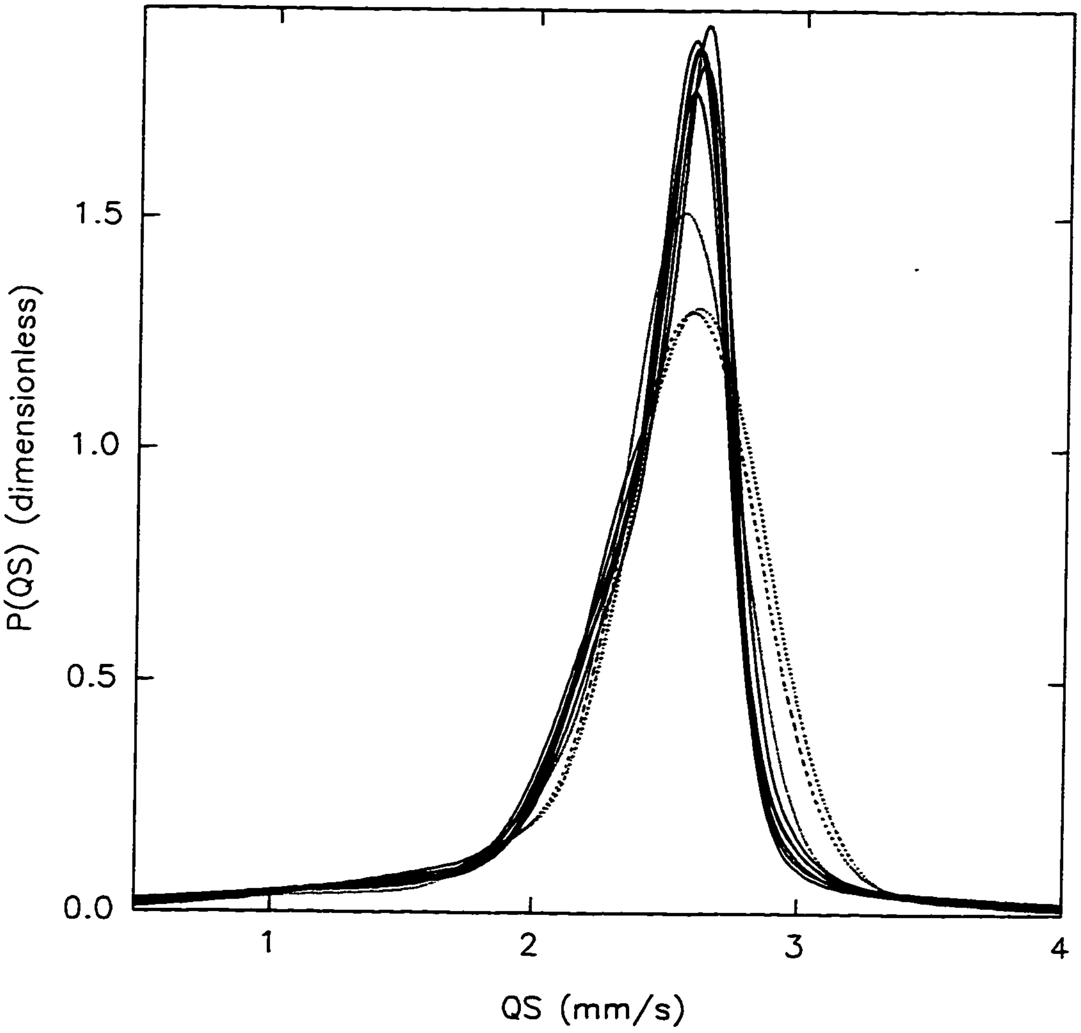

Figure 8.6: Fe^{2+} QSDs for all raw spectra: HK-samples, solid lines; RB-7, close-dots; RB-22, spaced-dots; and RB-25, dashes.

Spectra	QS_{peak}	$\overline{QS}$	S_k	σ_Δ
HK-550 RAW	2.630	2.436	0.194	0.466
HK-596 RAW	2.623	2.465	0.158	0.521
HK-650 RAW	2.596	2.436	0.160	0.593
HK-700 RAW	2.583	2.412	0.171	0.532
HK-750 RAW	2.607	2.439	0.168	0.444
HK-NNO RAW	2.589	2.425	0.164	0.572
RB-25 RAW	2.591	2.475	0.116	0.628
RB-22 RAW	2.607	2.496	0.111	0.597
RB-7 RAW	2.556	2.454	0.102	0.531

Table 8.3: QSD characteristic parameters for raw spectra.

Figure 8.6 shows the Fe^{2+} QSDs for all raw spectra.

However, we can distinguish the QSDs according to the stoichiometric mixes which they were synthesized from. The Fe^{2+} QSDs of the HK-samples are similar as they overlap one over the other. The same is not true for the RB-samples. Each of these has a distinct shape of its Fe^{2+} QSD, which is broader compared to those of the HK-samples. This may be due to the known presence of minor amounts of fayalite (section 5.3) which is an Fe-bearing mineral.

8.2 Obtaining thin-limit spectra

The primary aim in obtaining thin-limit spectra is to correct the spectra for the effects of absorber thickness. In order to treat the thickness effects correctly, we first fit each sample's spectrum with an arbitrary number of Voigt lines. We then extract the intrinsic absorber cross sections from the Voigt fits and use the cross sections to generate thin-limit spectra (as described in Section 7.2).

All the spectra were thickness-corrected such that to each raw spectrum there corresponds a simulated thin-limit spectrum. A representative average recoilless fraction of $\bar{f} = 0.5$ was used in thickness correcting. This is needed in order to obtain the parameter $\eta_M f_s$ from Equation 7.9. Thickness corrections using $\bar{f} = 0.7$

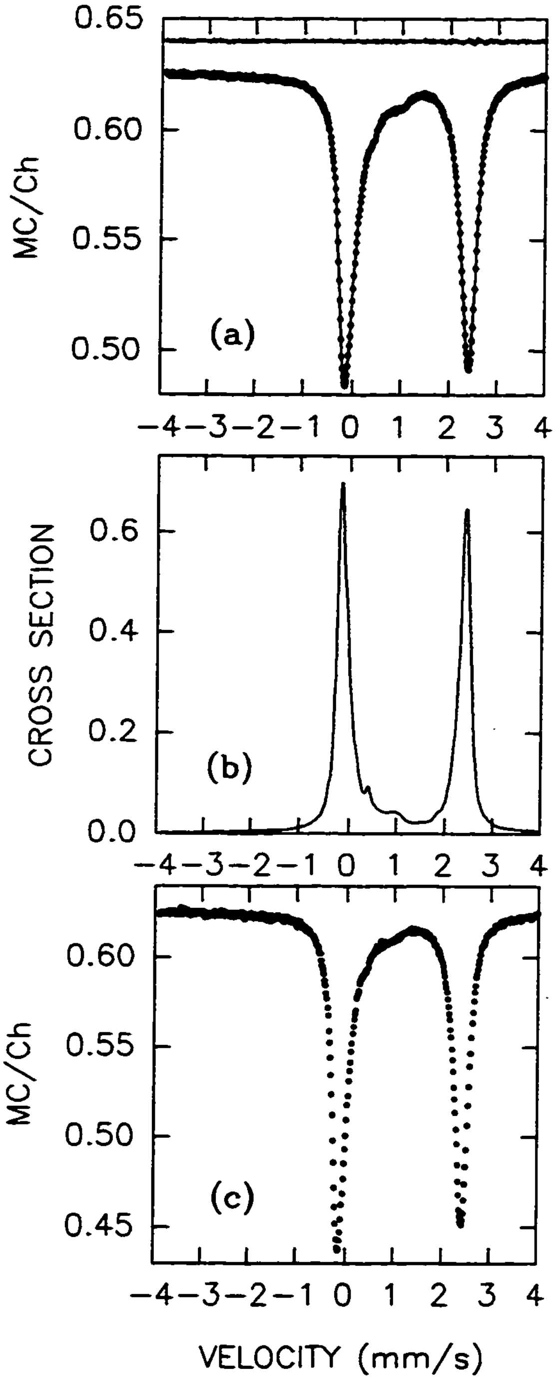

Figure 8.7: Thickness correction for the RT spectrum of annite HK-596. (a) Raw folded spectrum with ideal Voigt line fit and difference spectrum. (b) Extracted dimensionless intrinsic absorber resonance cross section. (c) Thin-limit spectrum with simulated Gaussian noise.

were also performed and confirmed that the results do not depend on the value of $\bar{f}$ between 0.5 and 0.7 for our spectra.

Our method is illustrated in Figure 8.7 where the Voigt fit of a raw folded spectrum, corresponding extracted absorber cross section, and the corresponding simulated thin-limit spectrum for the HK-596 sample are shown. The fitting parameters of the Voigt fits that were used to correct each of the raw spectra are tabulated in Appendix A.

8.3 QSD analysis of thin-limit spectra

We also performed a QSD analysis of the thin-limit spectra, using a 1-1-3 model. The fit parameters for the thin-limit spectra (TLS) of all samples are given in Tables 8.5 and 8.6. Figures 8.8-8.12 present the spectra of all samples with fits and residuals. The characteristic parameters for the Fe^{2+} QSDs of all thin-limit spectra are tabulated in Table 8.4.

Again, we conclude that the Fe^{2+} QSDs are distinguishable according to the stoichiometric mixes which they were synthesized from (see Figure 8.13). The Fe^{2+} QSDs of the HK-samples are similar as they overlap one over the other. The same is not true for the RB-samples. Each of these has a distinct shape of its Fe^{2+} QSD, which is broader compared to those of the HK-samples. This may be due to the known presence of minor amounts of fayalite (section 5.3) which is an Fe-bearing mineral.

Spectra	QS_{peak}	QS	S_k	σ_Δ
HK-550 TLS	2.610	2.458	0.152	0.417
HK-596 TLS	2.599	2.473	0.126	0.504
HK-650 TLS	2.593	2.448	0.145	0.478
HK-700 TLS	2.577	2.421	0.156	0.516
HK-750 TLS	2.592	2.445	0.147	0.421
HK-NNO TLS	2.579	2.438	0.141	0.232
RB-25 TLS	2.594	2.509	0.085	0.521
RB-22 TLS	2.622	2.530	0.092	0.460
RB-7 TLS	2.563	2.486	0.077	0.443

Table 8.4: Fe^{2+} QSD characteristic parameters for thin-limit spectra.

Sample $/BG$(MC/Ch)	Site	δ_0 (mm/s)	δ_1 (mm/s)	Δ (mm/s)	σ_Δ (mm/s)	h^+ (kC)	χ^2_{red}
HK-550	$<3^+>$	0.217	0.0^f	0.338	0.214	12.4	
	$[3^+]$	0.438	0.0^f	0.979	0.446	28.2	
	$[2^+]$-1			2.624	0.086	94.2	
	$[2^+]$-2			2.447	0.221	126.3	
0.585397	$[2^+]$-3	1.124	+.00148	2.150	0.835	45.9	1.06
HK-596	$<3^+>$	0.227	0.0^f	0.364	0.175	14.9	
	$[3^+]$	0.463	0.0^f	0.885	0.388	18.8	
	$[2^+]$-1			2.606	0.115	136.5	
	$[2^+]$-2			2.453	0.270	112.9	
0.624968	$[2^+]$-3	1.096	+.01300	2.117	1.125	44.6	1.30
HK-650	$<3^+>$	0.220	0.0^f	0.355	0.229	19.6	
	$[3^+]$	0.443	0.0^f	0.929	0.401	16.9	
	$[2^+]$-1			2.603	0.092	116.2	
	$[2^+]$-2			2.449	0.233	149.2	
0.752689	$[2^+]$-3	1.102	+.00877	2.114	1.021	54.3	1.32
HK-700	$<3^+>$	0.204	0.0^f	0.385	0.218	26.63	
	$[3^+]$	0.428	0.0^f	0.874	0.268	9.76	
	$[2^+]$-1			2.588	0.104	162.35	
	$[2^+]$-2			2.388	0.241	128.86	
0.852352	$[2^+]$-3	1.105	+.00676	2.005	1.113	54.25	1.13
HK-750	$<3^+>$	0.205	0.0^f	0.360	0.197	18.0	
	$[3^+]$	0.463	0.0^f	0.985	0.397	11.1	
	$[2^+]$-1			2.602	0.087	90.4	
	$[2^+]$-2			2.447	0.233	126.6	
0.634369	$[2^+]$-3	1.109	+.00530	2.144	0.825	47.7	1.17

^{f} This parameter was frozen during fit.

All fits impose Γ=0.194 mm/s ($2\Gamma_o$) and $h_+/h_-=1$.

Table 8.5: Fit parameters of thin-limit spectra for the HK-NNO C-CH_4 annealed samples.

Sample $/BG$(MC/Ch)	Site	δ_0 (mm/s)	δ_1 (mm/s)	Δ (mm/s)	σ_Δ (mm/s)	h^+ (kC)	χ^2_{red}
HK-NNO	$<3^+>$	0.231	0.0^f	0.329	0.214	16.6	
	$[3^+]$	0.370	0.0^f	1.008	0.423	21.8	
	$[2^+]$-1			2.590	0.106	155.3	
	$[2^+]$-2			2.390	0.229	134.0	
0.725487	$[2^+]$-3	1.128	-.00092	2.153	1.128	59.9	1.07
RB-25	$<3^+>$	0.258	0.0^f	0.348	0.139	50.1	
	$[3^+]$	0.496	0.0^f	0.783	0.222	29.9	
	$[2^+]$-1			2.593	0.221	583.3	
	$[2^+]$-2			2.221	1.041	138.6	
1.456051	$[2^+]$-3	0.976	+.05582	1.981	0.100	16.7	11.70
RB-22	$<3^+>$	0.209	0.0^f	0.279	0.124	34.6	
	$[3^+]$	0.428	0.0^f	0.824	0.450^f	24.0	
	$[2^+]$-1			2.627	0.172	258.2	
	$[2^+]$-2			2.561	0.353	256.9	
1.259102	$[2^+]$-3	0.959	+.06144	1.895	1.038	51.8	9.15
RB-7	$<3^+>$	0.255	0.0^f	0.369	0.157	47.2	
	$[3^+]$	0.487	0.0^f	0.944	0.359	27.0	
	$[2^+]$-1			2.561	0.173	324.7	
	$[2^+]$-2			2.128	0.111	23.4	
0.858979	$[2^+]$-3	1.048	+0.02871	2.309	0.817	91.3	4.99

[f] This parameter was frozen during fit.

All fits impose Γ=0.194 mm/s ($2\Gamma_o$) and h_+/h_-=1.

Table 8.6: Fit parameters of thin-limit spectra for the samples synthesized straight from stoichiometric mixtures.

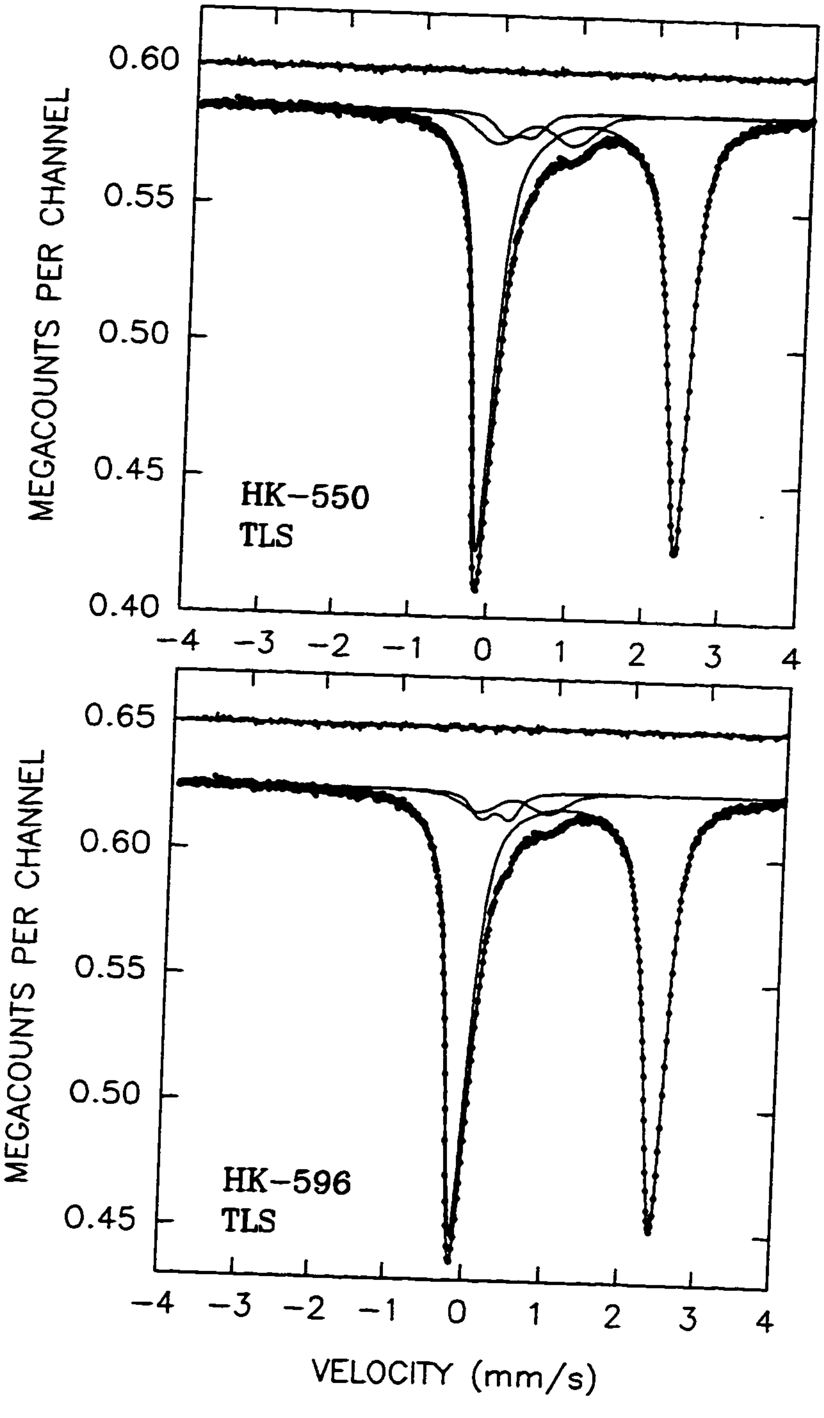

Figure 8.8: Thin-limit spectra of synthetic annite HK-550 (top) and HK-596 (bottom) with fits and residuals.

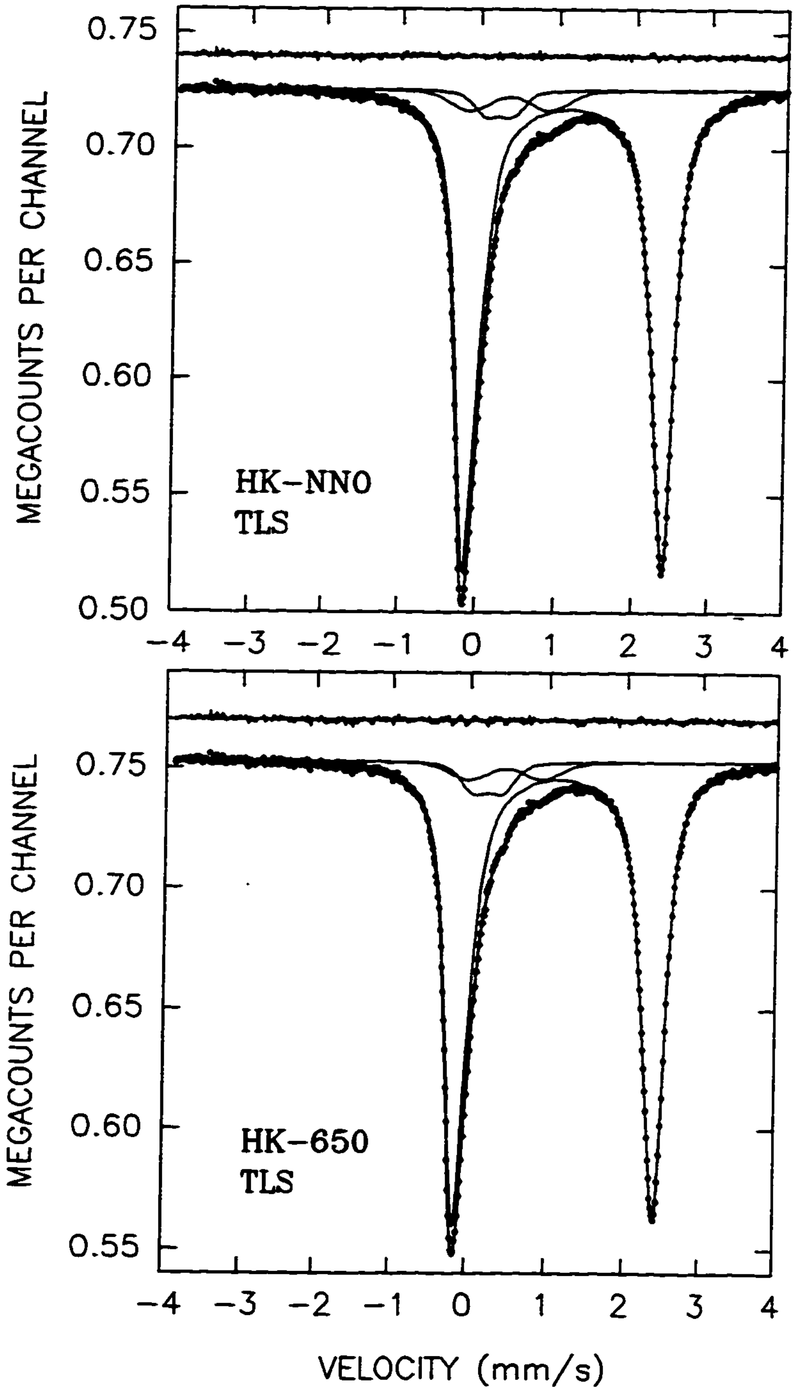

Figure 8.9: Thin-limit spectra of synthetic annite HK-NNO (top) and HK-650 (bottom) with fits and residuals.

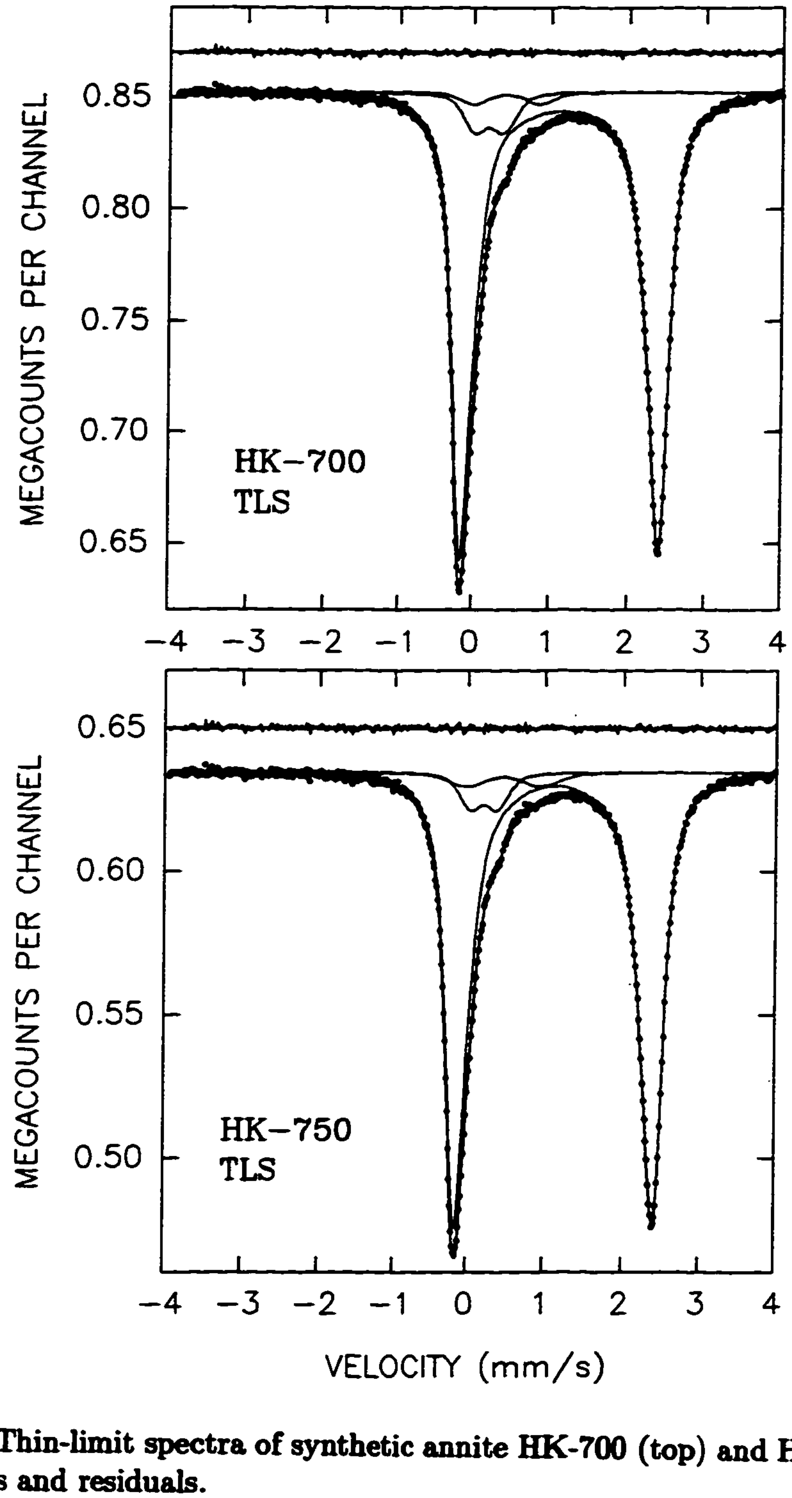

Figure 8.10: Thin-limit spectra of synthetic annite HK-700 (top) and HK-750 (bottom) with fits and residuals.

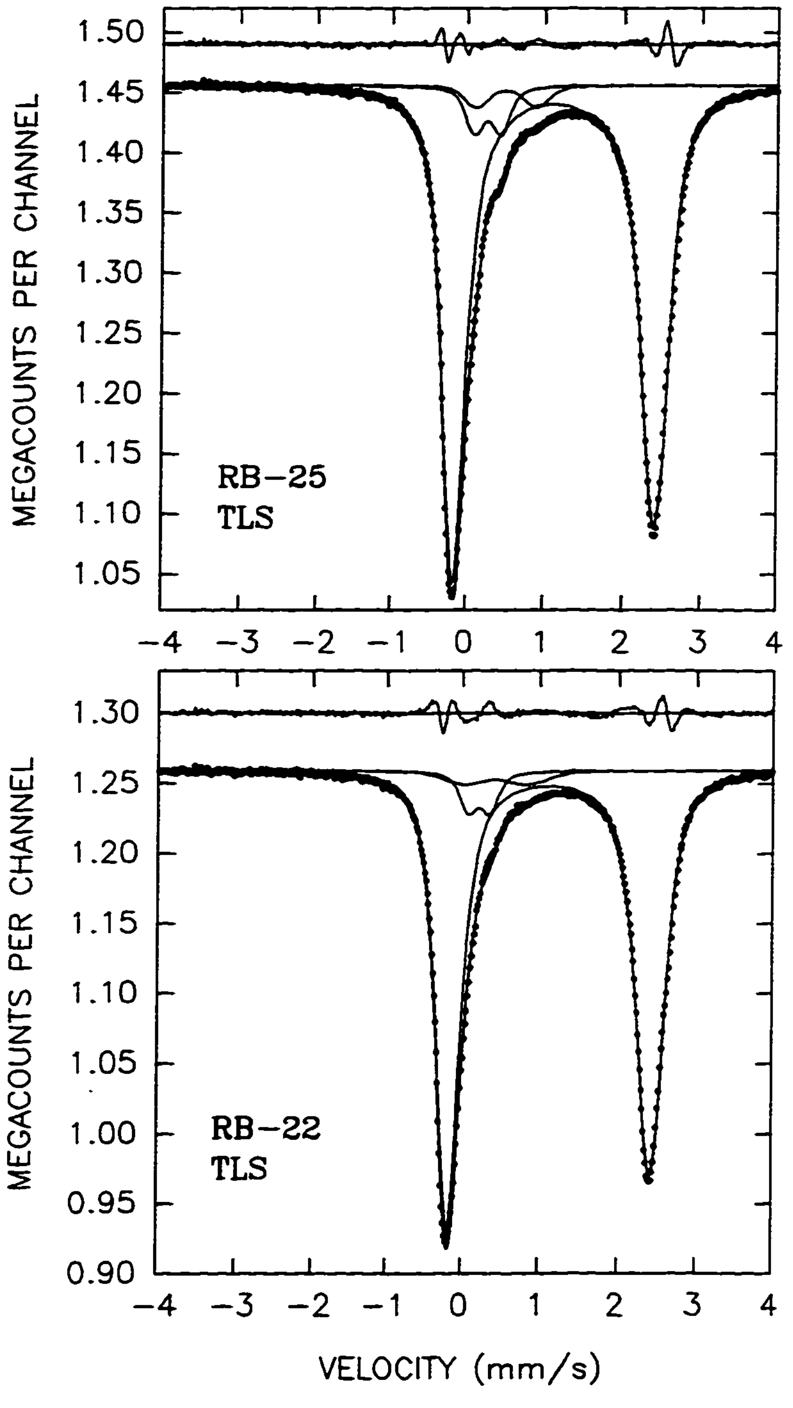

Figure 8.11: Thin-limit spectra of synthetic annite RB-25 (top) and RB-22 (bottom) with fits and residuals.

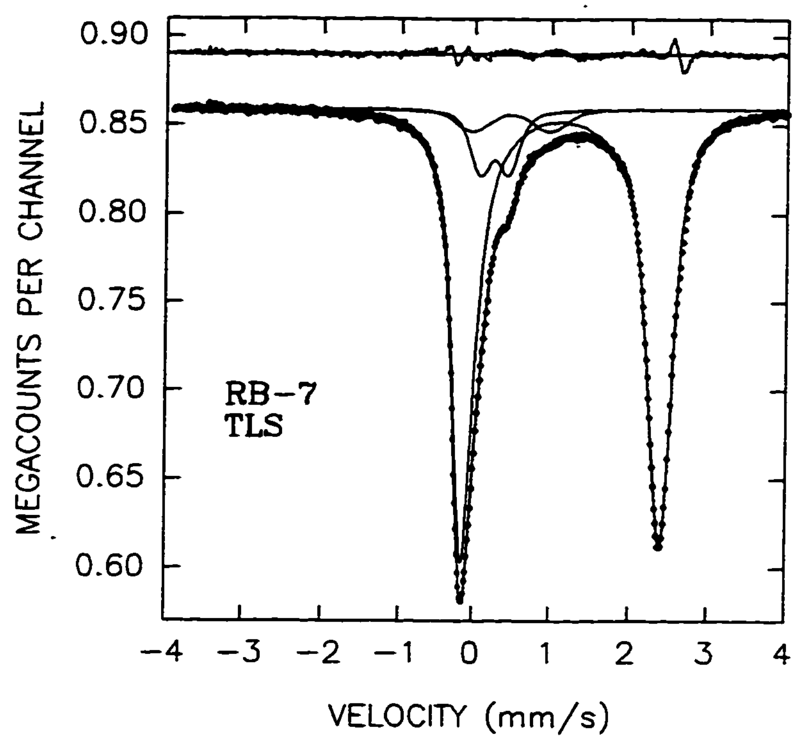

Figure 8.12: Thin-limit spectrum of synthetic annite RB-7 with fit and residual.

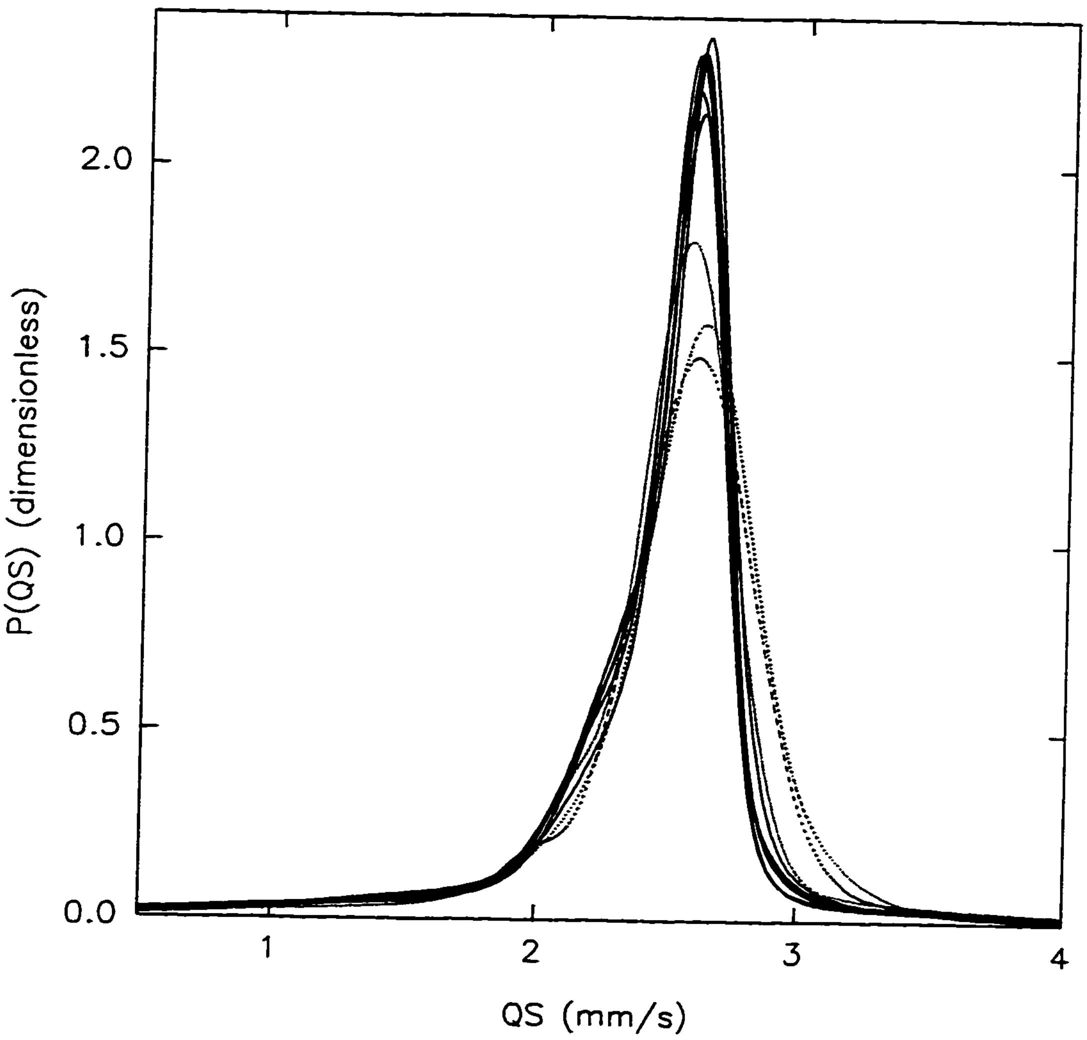

Figure 8.13: Fe^{2+} QSDs for all thin-limit spectra: HK-samples, solid lines; RB-7, close-dots; RB-22, spaced-dots; and RB-25, dashes.

8.4 Site populations

Site populations are of particular importance in annite because Fe^{3+} must, for structural reasons, exist in real annite. The QSD analysis that we performed enables us to determine the populations of the $<Fe^{3+}>$, $[Fe^{3+}]$, and $[Fe^{2+}]$ sites for both raw and thin-limit spectra.

On the basis of Equations 7.27, 7.28 and 7.29, we calculated the relative site populations in the following way. Since all fits impose $h_-/h_+ = 1$, we calculated the populations using only the h_+ values such that:

$$\frac{Fe_i}{Fe_{tot}} = \frac{\sum_1^{N_i} h_+}{\sum_{all} h_+}. \tag{8.2}$$

The top sum runs over the N_i Gaussian component h_+ values of a given i-th site and the bottom sum runs over all the h_+ values of all three sites.

The results are tabulated in Table 8.7 for both raw and thin-limit spectra. We also include the position of the high energy line for the $<Fe^{3+}>$ ($H_{tet} = \delta_{0_{tet}} + \frac{1}{2}\Delta_{tet}$), and $[Fe^{3+}]$ ($H_{oct} = \delta_{0_{oct}} + \frac{1}{2}\Delta_{oct}$) doublets. At room temperature, H_{tet} and H_{oct} are distinct spectral features occurring respectively at approximately +0.40 mm/s and +0.90 mm/s with respect to α-Fe. We use these values to assess the correctness of our fitting model in recognizing the Fe^{3+} tetrahedral and octahedral contributions.

As reported by Rancourt and al. [27], $H_{tet} < 0.35$ are suspicious because (1) in this case, both tetrahedral doublet lines are essentially hidden by the broad and mainly $[Fe^{2+}]$ absorption at ~-0.1 mm/s and (2) such values are significantly outside the true trioctahedral field which lies at 0.38-0.49 mm/s. All the fits we performed fall within that field except for RB-22 TLS, which still can be accepted as H_{tet} ~0.35.

In using QSD analysis, it is important to keep in mind that the χ^2 minimization does not usually produce a unique solution. One must admit the possibility for parameter trade-offs. Therefore, we need to map out the region, in the space of all the fitting parameters for our fitting model, that contains all the points corresponding to statistically equivalent fits of the particular measured spectrum. Such a region is called the solution domain in the Mössbauer parameter space. It represents the "Mössbauer solution": as much information as can be obtained from the measured

Spectra	$\frac{<Fe^{3+}>}{Fe_{tot}}$ %	H_{tet} mm/s	$\frac{\boxed{Fe^{3+}}}{Fe_{tot}}$ %	H_{oct} mm/s	$\frac{Fe^{3+}}{Fe_{tot}}$ %
HK-550 RAW	3.53	0.435	9.90	0.939	13.43
HK-596 RAW	4.13	0.437	6.73	0.948	10.86
HK-650 RAW	5.23	0.424	5.17	0.936	10.40
HK-700 RAW	6.07	0.416	3.85	0.908	9.92
HK-750 RAW	5.34	0.403	4.84	0.998	10.18
HK-NNO RAW	4.10	0.426	6.51	0.896	10.61
RB-25 RAW	5.72	0.439	2.82	0.862	8.54
RB-22 RAW	5.66	0.399	1.80	0.825	7.46
RB-7 RAW	8.78	0.441	4.30	0.934	13.08
HK-550 TLS	4.04	0.386	9.19	0.928	13.23
HK-596 TLS	4.55	0.409	5.74	0.906	10.29
HK-650 TLS	5.50	0.398	4.75	0.908	10.25
HK-700 TLS	6.97	0.397	2.56	0.865	9.53
HK-750 TLS	6.13	0.385	3.78	0.956	9.91
HK-NNO TLS	4.28	0.400	5.62	0.874	9.90
RB-25 TLS	6.12	0.432	3.65	0.888	9.77
RB-22 TLS	5.53	0.349	3.84	0.840	9.38
RB-7 TLS	9.19	0.440	5.26	0.959	14.45

Table 8.7: Site populations obtained from the QSD analysis of raw and thin-limit spectra.

spectrum by comparison with the chosen theoretical fitting lineshape model.

In the present work, we map out solution domains for all the thin-limit spectra. A relatively robust one-sigma (1σ) error is obtained by changing the value of the h_+ parameter for the tetrahedral Fe^{3+} (letting all other fit parameters adjust accordingly) until the value of χ^2 is increased by $\sqrt{2v}$ where v is the number of degrees of freedom. In our case, with 512 velocity channels and 19-20 free parameters; $v = 512 - 20 = 492$ and $\sqrt{2v} \simeq 31.4$. A 1σ change in the χ^2_{red} therefore corresponds to an increase $31.4/v = 0.064$.

In addition, to the extent that an ideal value of χ^2_{red} is not obtained, the above 1σ error is a considerable underestimate. That is, if we are willing to tolerate a fit with a $\chi^2_{red} = 4.99$ (as for RB-7 TLS) and accept it as a fair representation of the correct total lineshape, then we should also accept the fits that have similar residuals and are qualitatively equivalent on the scale of the difference between the accepted lowest χ^2_{red} and its ideal value of 1. That is, we should tolerate increases in the χ^2_{red} value ($\Delta\chi^2_{red}$) of

$$\Delta\chi^2_{red} = \frac{\chi^2_{red}(\text{accepted})}{\chi^2_{red}(\text{ideal})} \times 0.064 = \chi^2_{red}(\text{accepted}) \times 0.064, \tag{8.3}$$

or of χ^2_{red} ~5.3 in the case of fit RB-7 TLS.

The above constitutes the statistical limit that we used to establish the boundary of the solution domains. But sometimes the statistical limit would generate fitting parameters that were hard to believe from a physical point of view. In such cases, we imposed the physical limit $H_{tet} \geq 0.35$ as mentioned earlier in the text. We report the fit parameters that were used to establish the solution domains at the end of this section in Tables 8.10-8.13.

From these parameters, we calculated the "Mössbauer solution". It represents the range of populations possible for each of the sites assuming a QSD model; Table 8.8 presents the results. On examining these data, we realize that they give a relatively wide range of possible populations for the <Fe^{3+}> and [Fe^{3+}] sites. Figure 8.14 illustrates the upper and lower limits for the tetrahedral and octahedral Fe^{3+} site populations for each of the samples. Because of the small amount of Fe^{3+} present in our sample, our fitting model can systematically distribute the spectral

Spectra	$\frac{<Fe^{3+}>}{Fe_{tot}}$ %		$\frac{\boxed{Fe^{3+}}}{Fe_{tot}}$ %		$\frac{Fe^{3+}}{Fe_{tot}}$ %	
	lower	upper	lower	upper	lower	upper
HK-550 TLS	2.45	7.91	4.82	11.27	12.72	13.72
HK-596 TLS	2.82	6.44	3.25	8.38	9.69	11.20
HK-650 TLS	3.66	7.73	1.90	7.41	9.63	11.07
HK-700 TLS	5.33	8.29	1.27	4.80	9.56	10.13
HK-750 TLS	4.77	7.81	1.49	5.59	9.30	10.36
HK-NNO TLS	2.56	7.73	1.85	7.88	9.58	10.44
RB-25 TLS	4.09	7.80	1.93	6.49	9.73	10.78
RB-22 TLS	4.58	7.69	1.57	4.86	9.26	9.44
RB-7 TLS	7.79	10.67	3.26	6.78	13.93	14.57

Table 8.8: Lower and upper bounds on site populations obtained from the solution domains.

area corresponding to the total Fe^{3+} in either the tetrahedral or octahedral site, without significantly increasing the χ^2 value. As it turns out, the accuracy of these site populations are the order of ~5%. Nevertheless, systematic sample to sample differences are detected to better than ~1%.

According to our results, the site populations depend on the synthesis conditions. With the exception of sample HK-750, as the equilibration temperature increases there is a migration of Fe^{3+} ions from the octahedral towards the tetrahedral sites in the annite of the HK-samples (treated versions of annite HK-NNO equilibrated with the C-CH_4 buffer at 2 kbar and with different equilibration/synthesis temperatures).

Annite RB-25 and RB-22 —which were synthesized at 2 kbar with the C-CH_4 buffer and at respectively 700°C and 750°C— also seem to obey the same rule as their population ranges are comparable to those of annite HK-700 and HK-750. As for annite RB-7, synthesized at 700°C with the Ni-NiO buffer, it has a higher amount of Fe^{3+} in both tetrahedral and octahedral sites as compared to annite HK-700, consistent with the fact that at this temperature the Ni-NiO buffer is less reducing than the C-CH_4 buffer [21].

Besides that, samples HK-550 and HK-750 do not follow the same trend as

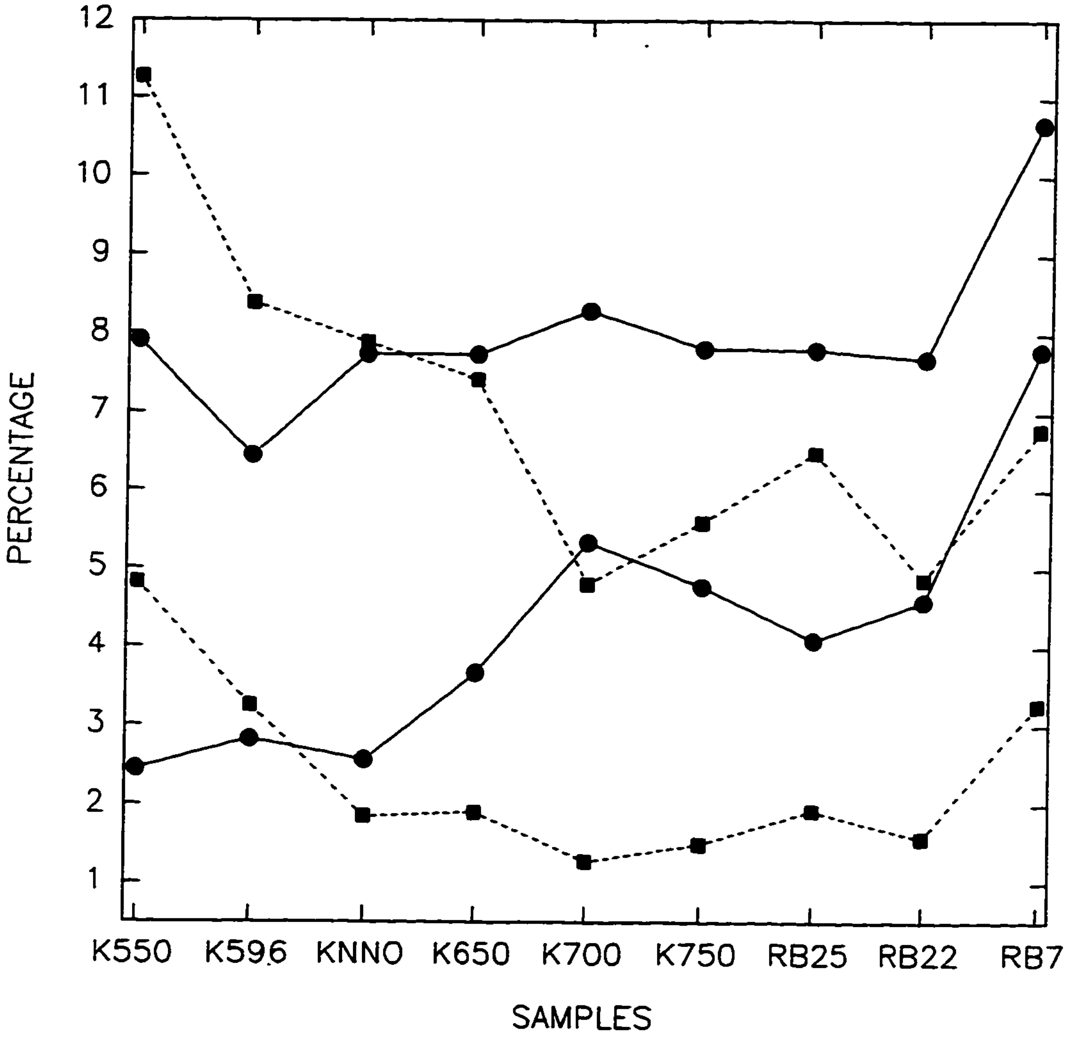

Figure 8.14: The <Fe^{3+}> (circles) and [Fe^{3+}] (squares) site populations. The upper and lower bounds of the acceptable range for each population are shown. The uncertainty of each measurement is a result of trade-off problems.

the other HK-samples. Sample HK-550 has a higher fraction of Fe^{3+} in both the octahedral and tetrahedral sites when compared to the other HK-samples. As for sample HK-750, it contains amounts of $[Fe^{3+}]$ and $<Fe^{3+}>$ which seem to be inverse with respect to the other HK-samples. As explained earlier in Section 5.3, this is probably due to the formation of a phase of sanidine in the equilibration/synthesis process. That is, these samples were most likely outside the stability range for single-phase annite.

At this point it is worth mentioning that the χ^2_{red} value we obtained for the fits of the RB-samples are significantly higher than those for the HK-samples. This is probably due to the presence of minor amounts of fayalite, an Fe-bearing phase, in the RB-samples.

Let's now consider the Fe^{3+} to Fe^{2+} populations tradeoff. In this case, we obtain a relatively narrow range of possible populations for the solution domain (see Table 8.8). Figure 8.15 demonstrates that our results for the total Fe^{3+} populations (considering only the results of the QSD analysis) are accurate within ~1%.

Furthermore, in Figure 8.15 we observe that in the low equilibration temperature range there is a higher concentration of Fe^{3+}. With the exception of sample HK-550 and RB-7, the sample to sample variations of $\frac{Fe^{3+}}{Fe_{tot}}$ are the order of ~0.2%.

In the case of sample HK-550, its deviation of $\frac{Fe^{3+}}{Fe_{tot}}$ is the order of ~3%. This is probably due to the considerable amount of sanidine, $K(Si_3Al)O_8$, that was produced through the equilibration process. With such a phase sanidine, the composition of the annite phase may be off stoichiometry. As for sample RB-7, it has the highest amount of Fe^{3+}; this is consistent with the fact that Ni-NiO buffer is less reducing than the C-CH_4 buffer.

We corroborate the latter observations by an independant measurement of the total Fe^{3+} amount. The method is described in detail by Rancourt et al. [16]. It relies on the intrinsic absorber cross sections (CRS) that we extracted from each of the raw spectra. Looking at a particular cross section, the level closest to the zero-resonance BG level located between the two major peaks clearly divides the cross section into two areas. These are a low-energy area, A_L, and a high-energy area, A_H. Considering that A_H arises most entirely from the high-energy line of the

Fe^{2+} doublet, we evaluate the Fe^{3+} contribution as

$$Fe^{3+}/Fe_{tot} = (A_L - A_H)/(A_L + A_H) \tag{8.4}$$

and, since the dividing energy for each of the cross sections has a maximum uncertainty of ~ ±0.07 mm/s, we evaluated the uncertainty of these measurements to be of ±0.5%.

The results of the CRS method are tabulated in Table 8.9. In Figure 8.15, we observe that the CRS method also presents a systematic variation of Fe^{3+}/Fe_{tot} with respect to the synthesis temperature.

But when we compare this line with the results of the QSD analysis, we realize that the cross section method always attributes a higher Fe^{3+}/Fe_{tot} concentration. One possible mechanism for this systematic difference is as follows. There might have been small amounts of texture present in our absorbers. Sometimes, the crystal grains of the powder align themselves along the cleavage planes. This in turn results in asymmetric quadrupole doublets with greater low-energy line area. Since all the QSD fits impose $h_-/h_+ = 1$, our fitting model resolves the spectra with doublets having their low-energy line area equal to their high-energy line area. In the perspective of small amounts of texture present in our absorbers A_L is enhanced

Cross section	dividing energy (mm/s)	$\frac{Fe^{3+}}{Fe_{tot}}$ ±0.50%
HK-550	1.431	14.12
HK-596	1.374	12.08
HK-650	1.383	12.09
HK-700	1.354	11.44
HK-750	1.351	10.72
HK-NNO	1.417	11.94
RB-25	1.343	11.51
RB-22	1.319	10.33
RB-7	1.354	14.74

Table 8.9: Results of the cross section method.

and then, the cross section method attributes a slightly higher Fe^{3+} concentration when compared to the results of the QSD analysis.

Another mechanism is related to the cross section method. In the choice of the dividing energy, one ideally has to ensure that this energy corresponds to an equal area tradeoff between the tails of the [Fe^{3+}] and [Fe^{2+}] high-energy lines. When the dividing energy is too high, the assumed area of the tail of the [Fe^{3+}] high-energy line is greater than that assumed for the [Fe^{2+}] high-energy line. In this case, the cross section method systematically attributes an amount of Fe^{3+} which is higher than what is present in reality.

In the present work, we chose the level closest to the zero-resonance BG level as the dividing energy. We did not establish that this energy indeed corresponds to an equal area tradeoff between the tails of the [Fe^{3+}] and [Fe^{2+}] high-energy lines; this task being practically impossible. Instead, we used the uncertainty in the zero-resonance BG level to evaluate the uncertainty in the cross section measurements.

In view of the above discussion and considering the nature of both mechanisms, we believe the QSD analysis gave results which are the closest to the true values. In any case, the QSD analysis corresponds to the solution which minimizes the effects associated to either of these features.

Finally, considering that we have used synthesis temperatures over the entire stability range for annite, we conclude that we have obtained an experimental lower bound on Fe^{3+}/Fe_{tot} of 9.26%. It corresponds to the value of annite sample RB-22, which we found by mapping the solution domains for the QSD analyses of the thin-limit RT spectra of all the samples.

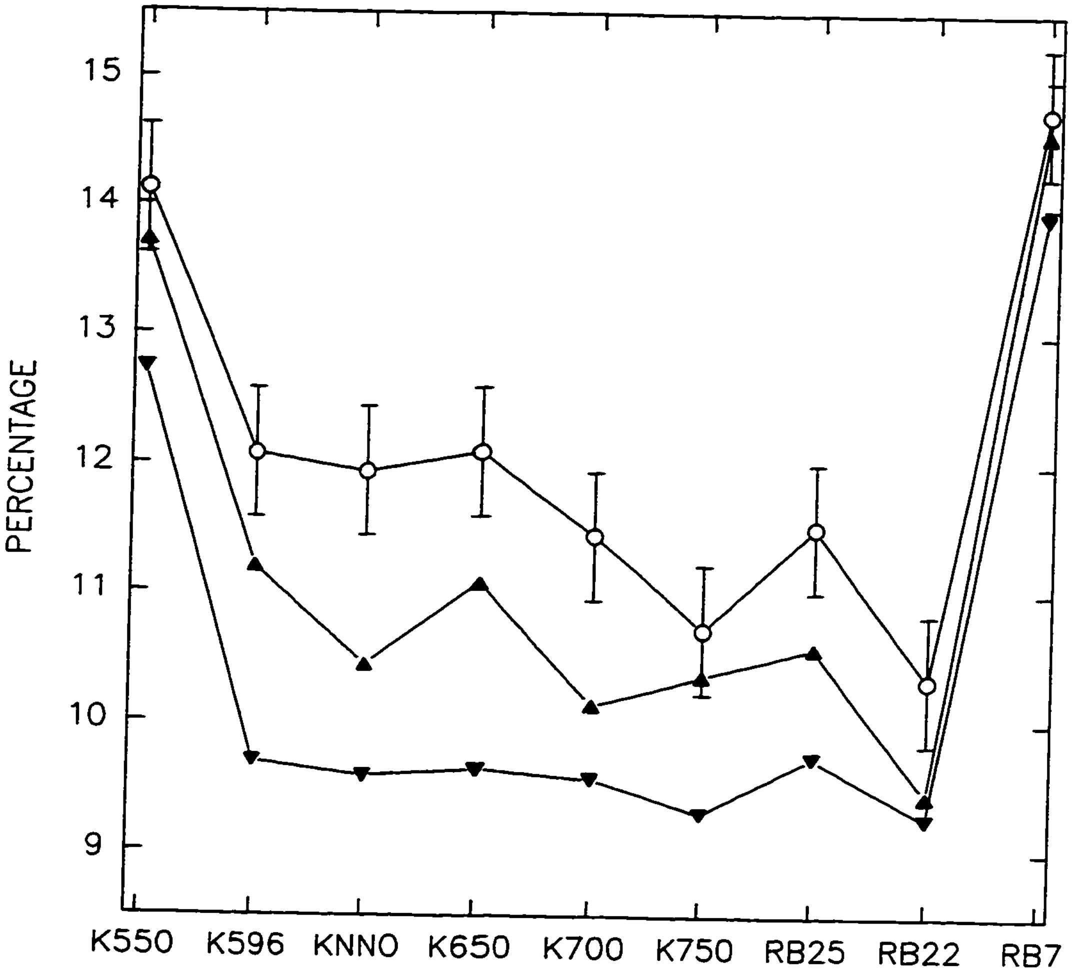

Figure 8.15: The total Fe^{3+} contribution. The QSD analysis gives an upper-limit (triangle-up) and a lower-limit (triangle-down) for the Fe^{3+}/Fe_{tot}, as a result of trade-off problems. The line made of hollow circles represents the results of the cross section method.

Sample $/BG$(MC/Ch)	Site	δ_0 (mm/s)	δ_1 (mm/s)	Δ (mm/s)	σ_Δ (mm/s)	h^+ (kC)	χ^2_{red}
HK-550	$<3^+>$	0.218	0.0^f	0.302	0.134	7.50^f	
	$[3^+]$	0.445	0.0^f	0.922	0.519	34.46	
	$[2^+]$-1			2.623	0.087	96.35	
	$[2^+]$-2			2.442	0.211	120.85	
0.585381	$[2^+]$-3	1.107	+.00816	2.218	0.735	46.67	1.13^s
HK-596	$<3^+>$	0.233	0.0^f	0.341	0.113	9.20^f	
	$[3^+]$	0.469	0.0^f	0.869	0.499	27.36	
	$[2^+]$-1			2.608	0.118	140.61	
	$[2^+]$-2			2.437	0.251	102.34	
0.624877	$[2^+]$-3	1.092	+.01527	2.246	0.897	46.99	1.37^s
HK-650	$<3^+>$	0.240	0.0^f	0.319	0.163	13.0^f	
	$[3^+]$	0.451	0.0^f	0.893	0.522	26.3	
	$[2^+]$-1			2.608	0.091	114.4	
	$[2^+]$-2			2.447	0.217	145.0	
0.752603	$[2^+]$-3	1.086	+.00877	2.216	0.841	56.3	1.39^s
HK-700	$<3^+>$	0.222	0.0^f	0.349	0.171	20.3^f	
	$[3^+]$	0.422	0.0^f	0.891	0.451	18.3	
	$[2^+]$-1			2.588	0.106	171.3	
	$[2^+]$-2			2.370	0.222	115.3	
0.852269	$[2^+]$-3	1.087	+.01408	2.101	0.943	55.7	1.20^s
HK-750	$<3^+>$	0.222	0.0^f	0.334	0.157	14.0^f	
	$[3^+]$	0.465	0.0^f	0.932	0.527	16.4	
	$[2^+]$-1			2.606	0.086	88.5	
	$[2^+]$-2			2.448	0.218	122.6	
0.634354	$[2^+]$-3	1.090	+.01304	2.218	0.714	52.1	1.24^s

^{f} This parameter was frozen during fit.

^{s} Statistical limit imposed.

All fits impose Γ=0.194 mm/s ($2\Gamma_o$) and h_+/h_-=1.

Table 8.10: Fit parameters of thin-limit spectra (HK-550,..., HK-750) in which we impose a minimum <Fe^{3+} > contribution.

Sample $/BG$(MC/Ch)	Site	δ_0 (mm/s)	δ_1 (mm/s)	Δ (mm/s)	σ_Δ (mm/s)	h^+ (kC)	χ^2_{red}
HK-NNO	$< 3^+ >$	0.228	0.0^f	0.307	0.152	9.90^f	
	$[3^+]$	0.404	0.0^f	0.901	0.535	30.45	
	$[2^+]$-1			2.590	0.109	155.3	
	$[2^+]$-2			2.374	0.219	122.69	
0.725414	$[2^+]$-3	1.116	+.00348	2.222	1.004	59.19	1.14^s
RB-25	$< 3^+ >$	0.261	0.0^f	0.343	0.081	33.4	
	$[3^+]$	0.499	0.0^f	0.752	0.391	53.0	
	$[2^+]$-1			2.593	0.215	556.9	
	$[2^+]$-2			2.330	0.819	158.6	
1.455892	$[2^+]$-3	0.982	+.05406	2.024	0.099	14.6	12.51^s
RB-22	$< 3^+ >$	0.209^f	0.0^f	0.279^f	0.109	28.6^f	
	$[3^+]$	0.428^f	0.0^f	0.824^f	0.336	30.4	
	$[2^+]$-1			2.626	0.094	86.5	
	$[2^+]$-2			2.606	0.276	398.9	
1.259066	$[2^+]$-3	0.963	+.06144	2.085	0.781	80.7	$8.83^{s,p}$
RB-7	$< 3^+ >$	0.256	0.0^f	0.360	0.127	40.0^f	
	$[3^+]$	0.481	0.0^f	0.892	0.445	34.8	
	$[2^+]$-1			2.561	0.169	316.4	
	$[2^+]$-2			2.154	0.109	23.3	
0.858960	$[2^+]$-3	1.040	+0.03252	2.332	0.734	98.9	5.27^s

^{f} This parameter was frozen during fit.

^{s} Statistical limit imposed.

^{s,p} Both statistical and physical limit imposed.

All fits impose Γ=0.194 mm/s ($2\Gamma_o$) and h_+/h_-=1.

Table 8.11: Fit parameters of thin-limit spectra (HK-NNO, RB-...) in which we impose a minimum $<Fe^{3+}>$ contribution.

Sample $/BG$(MC/Ch)	Site	δ_0 (mm/s)	δ_1 (mm/s)	Δ (mm/s)	σ_Δ (mm/s)	h^+ (kC)	χ^2_{red}
HK-550	$< 3^+ >$	0.236	0.0^f	0.329	0.342	18.0^f	
	$[3^+]$	0.410	0.0^f	1.101	0.345	21.4	
	$[2^+]$-1			2.623	0.084	92.2	
	$[2^+]$-2			2.444	0.226	131.3	
0.585425	$[2^+]$-3	1.138	-.00350	2.081	0.930	44.6	1.08^p
HK-596	$< 3^+ >$	0.220	0.0^f	0.402	0.264	21.2	
	$[3^+]$	0.472	0.0^f	0.910	0.226	10.7	
	$[2^+]$-1			2.605	0.114	134.5	
	$[2^+]$-2			2.458	0.282	119.5	
0.625060	$[2^+]$-3	1.104	+.00969	1.968	1.373	43.2	1.37^s
HK-650	$< 3^+ >$	0.205	0.0^f	0.389	0.384	27.60^f	
	$[3^+]$	0.458	0.0^f	0.958	0.156	6.80	
	$[2^+]$-1			2.601	0.091	116.10	
	$[2^+]$-2			2.449	0.243	154.02	
0.752773	$[2^+]$-3	1.110	+.00552	1.988	1.211	52.28	1.39^s
HK-700	$< 3^+ >$	0.181	0.0^f	0.431	0.289	31.70^f	
	$[3^+]$	0.446	0.0^f	0.867	0.103	4.84	
	$[2^+]$-1			2.587	0.102	158.09	
	$[2^+]$-2			2.389	0.244	134.78	
0.852392	$[2^+]$-3	1.120	+.00130	1.935	1.216	52.99	1.20^s
HK-750	$< 3^+ >$	0.175	0.0^f	0.394	0.245	23.00^f	
	$[3^+]$	0.456	0.0^f	0.952	0.157	4.40	
	$[2^+]$-1			2.599	0.087	91.64	
	$[2^+]$-2			2.444	0.253	133.30	
0.634415	$[2^+]$-3	1.129	-.00241	1.991	1.024	42.09	1.24^s

[f] This parameter was frozen during fit.

[p] Physical limit imposed.

[s] Statistical limit imposed.

All fits impose Γ=0.194 mm/s ($2\Gamma_o$) and $h_+/h_-=1$.

Table 8.12: Fit parameters of thin-limit spectra (HK-550,...,HK-750) in which we impose a maximum <Fe^{3+} > contribution.

Sample $/BG$(MC/Ch)	Site	δ_0 (mm/s)	δ_1 (mm/s)	Δ (mm/s)	σ_Δ (mm/s)	h^+ (kC)	χ^2_{red}
HK-NNO	$<3^+>$	0.207	0.0[f]	0.449	0.607	30.00[f]	
	$[3^+]$	0.491	0.0[f]	0.949	0.183	7.19	
	$[2^+]$-1			2.590	0.103	148.73	
	$[2^+]$-2			2.402	0.234	143.61	
0.725528	$[2^+]$-3	1.125	-.00014	2.065	1.233	58.59	1.14[s]
RB-25	$<3^+>$	0.255	0.0[f]	0.341	0.193	64.0	
	$[3^+]$	0.477	0.0[f]	0.833	0.086	15.8	
	$[2^+]$-1			2.593	0.225	600.1	
	$[2^+]$-2			2.128	1.300	119.5	
1.456189	$[2^+]$-3	0.978	+.05513	1.944	0.099	21.2	12.49[s]
RB-22	$<3^+>$	0.209[f]	0.0[f]	0.279[f]	0.217	48.00[f]	
	$[3^+]$	0.428[f]	0.0[f]	0.824[f]	0.013	9.78	
	$[2^+]$-1			2.631	0.125	146.42	
	$[2^+]$-2			2.590	0.311	- 369.03	
1.259005	$[2^+]$-3	0.953	+.06314	1.656	1.177	50.96	8.75[s,p]
RB-7	$<3^+>$	0.242	0.0[f]	0.383	0.201	55.0[f]	
	$[3^+]$	0.504	0.0[f]	0.913	0.196	16.8	
	$[2^+]$-1			2.562	0.178	336.9	
	$[2^+]$-2			2.093	0.111	24.7	
0.859092	$[2^+]$-3	1.051	+0.02714	2.243	0.996	81.9	5.32[s]

[f] This parameter was frozen during fit.

[s] Statistical limit imposed.

[s,p] Both statistical and physical limit imposed.

All fits impose Γ=0.194 mm/s ($2\Gamma_o$) and h_+/h_-=1.

Table 8.13: Fit parameters of thin-limit spectra (HK-NNO, RB-...) in which we impose a maximum <Fe^{3+} > contribution.

8.5 Summary

In this chapter, we have obtained site populations in nine annites synthesized using the highly reducing C-CH_4 buffer and the less reducing Ni-NiO buffer, with various equilibration temperatures. The Mössbauer data analysis involved full thickness effect corrections and quadrupole splitting distribution analysis.

In examining the extracted Fe^{2+} QSDs of all the spectra, we concluded that the Fe^{2+} QSDs are distinguishable according to the stoichiometric mixes which they were synthesized from (see Figure 8.13). The Fe^{2+} QSDs of the HK-samples are similar whereas the same is not true for the RB-samples. Each of these has a distinct shape for in its Fe^{2+} QSD, which is broader compared to those of the HK-samples. This is probably due to the presence of minor amounts of fayalite, an Fe-bearing mineral, in the RB-samples.

By using synthesis temperatures over the entire stability range for annite, we traced the evolution of $[Fe^{3+}]$ and $<Fe^{3+}>$, and have obtained an experimental lower bound on Fe^{3+}/Fe_{tot}. In the light of our results, temperature has a systematic effect. As the synthesis temperature increases, there is a migration of the Fe^{3+} ions from the octahedral sites towards the tetrahedral sites. Also, we observe that at the lowest and highest equilibration temperature there is a higher concentration of Fe^{3+}, related to non-stoichiometry of the annite phase.

In the next chapter, we will compare our site population measurements with the structural misfit model that we elaborated in Chapter 4.

Chapter 9. Comparison of Population Results with the Misfit Model

In Chapter 4, we proposed a structural misfit model for the observed stoichiometry of real annite. In this chapter, we compare this model with our site population measurements.

The structural misfit model predicts a linear relationship (Equation 4.6) between the [Fe^{3+}] and <Fe^{3+}> site populations (x and y), that must be satisfied to achieve octahedral/tetrahedral sheet matching and bond sharing. This x-y relationship depends on the equilibration (or synthesis) temperature T, the tetrahedral rotation angle α (at T), and the thermal expansion coefficients α_o and α_t.

Since tetrahedral rotation requires very little energy, with the highly reducing conditions α is expected to be zero at synthesis. The main uncertainties in the model then arise from the measured values of A and B (which determines the value of γ and β; A and B are values established experimentally through the measurement of the in-plane b lattice parameter) and the measured values of α_o and α_t.

The best values of A and B reported by Hazen and Wones [17] are 7.64 Å and 2.19, respectively. However, their data is consistent with values in an (A,B) range from (7.39 Å, 2.52) to (8.17 Å, 1.46). The latter arises considering only the data for Ni, Mg, Cu, and Co end-members. We will illustrate the range of (A,B) values that is consistent with Hazen and Wones' data later in this chapter[1].

Commonly accepted values for the thermal expansion coefficients are $\alpha_t = 0$ and $\alpha_o = 14\times10^{-6}$ °C^{-1} [28]. It has been pointed out that such values do not generally include thermal corrections [29]. For example, when full corrections are applied to the tetrahedral bond data, one more typically obtains $\alpha_t = 10\times10^{-6}$ °C^{-1} [29]. As for α_o, it can range from 10×10^{-6} to 50×10^{-6} °C^{-1} [28].

---

[1] See note added in proof.

Our site population results (Table 8.7) are shown in Figure 9.1 along with the $\cos(\alpha) = 1$ theoretical predictions using the common estimates of α_o and α_t and a middle (i.e. best) and limiting values of (A,B). One sees that the structural misfit model has potential to explain our observations. We will explore the possibilities of the model in the rest of the chapter.

Before going any further, there are questions which may arise if we carefully consider Figure 9.1. First, we note that samples HK-700 and HK-750 seem to be inversed with respect to the other HK-samples. Besides that, sample HK-550 also does not follow the same trend as the other HK-samples. As explained earlier in Section 5.3, this is probably due to the formation of a phase of sanidine in the equilibration/synthesis process. That is, these samples (HK-550 and HK-750) were most likely outside the stability range for single-phase annite.

Let's now have a look at what happens in the model when we impose various values for the A, B, α_o and α_t parameters. In Figure 9.2, using $\alpha_t = 0$ and various coefficients for α_o, we present the predictions corresponding to a middle (i.e. best) and a limiting value of (A,B). As we can see, changing the (A,B) values greatly affects the positions of the x-y lines for a given α_o. As well, the distance between the lines corresponding to the T=550°C and T=750°C theoretical predictions also displays small variations. In Figure 9.3, we illustrate the effect of having various differences $(\alpha_o - \alpha_t)$ for the same value of (A,B). We observe that the relative positions of the x-y lines changes and that the distances between the lines corresponding to the T=550°C and T=750°C theoretical predictions are not constants for a given difference $(\alpha_o - \alpha_t)$.

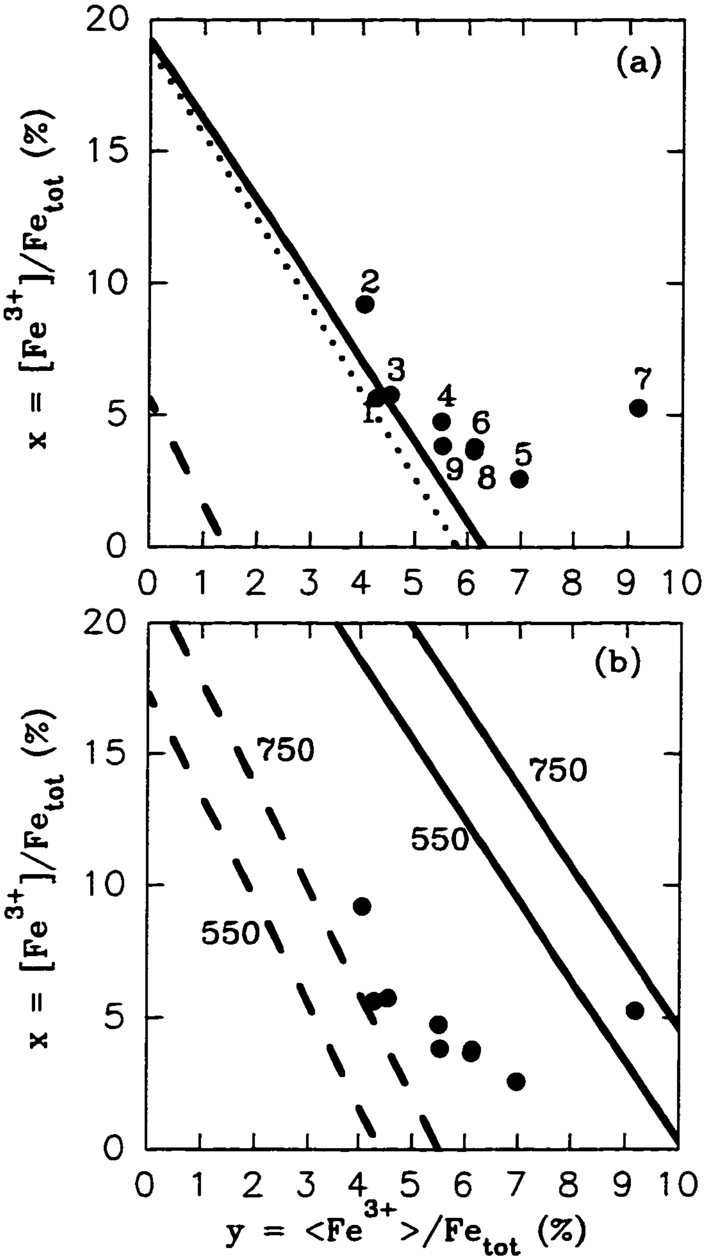

Figure 9.1: Measured [Fe^{3+}] and <Fe^{3+}> site populations compared to the structural misfit model: (a) $T = RT$ and (A, B) = (8.17Å, 1.46) (dashed line), (7.64Å, 2.19) (dotted line), (7.39Å, 2.52) (solid line); (b) T = 550 and 750°C with (A,B) = (8.17Å, 1.46) (dashed lines), (7.39Å, 2.52) (solid lines). Samples are 1=HK-NNO, 2-6=HK-550-750, 7=RB-7, 8=RB-25, 9=RB-22.

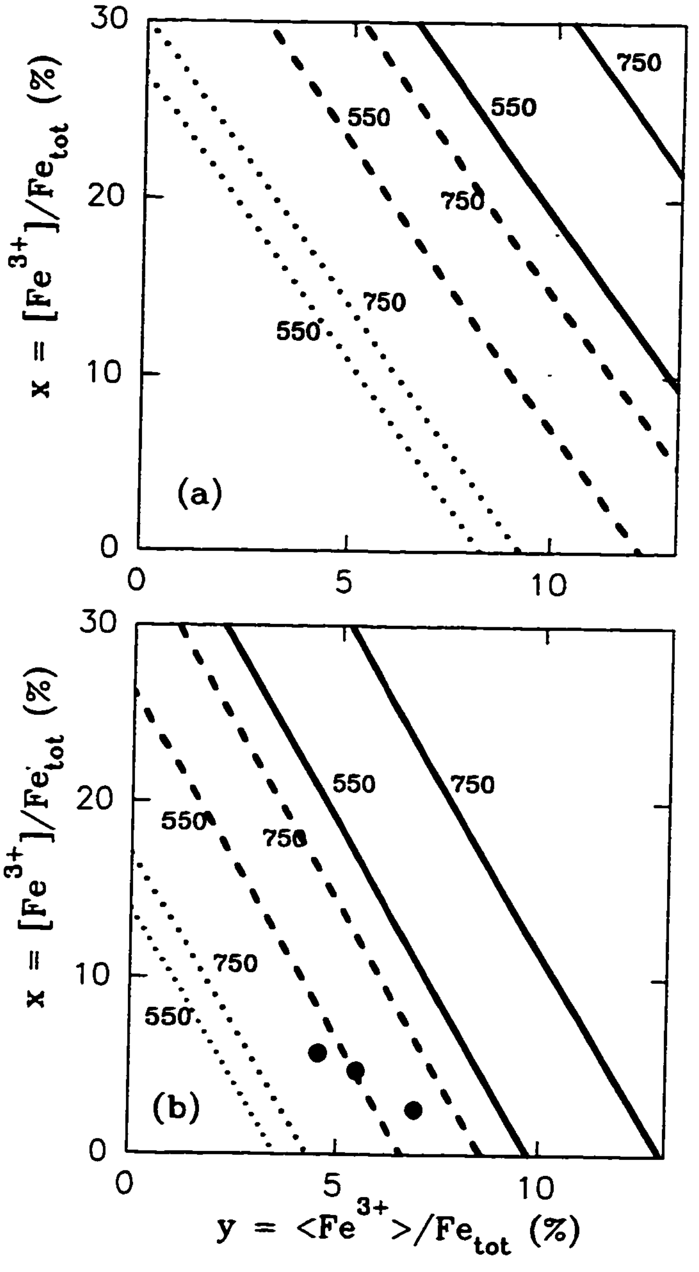

Figure 9.2: The effect of changing the (A,B) parameters: (a) (A,B) = (7.640 Å, 2.188), and (b) (A,B) = (8.166 Å, 1.457). The values of the other parameters are as follows: $\alpha_t=0$ and $\alpha_o = 10\times10^{-6}$ °C^{-1} (dotted lines), 25×10^{-6} °C^{-1} (dashed lines), 40×10^{-6} °C^{-1} (solid lines).

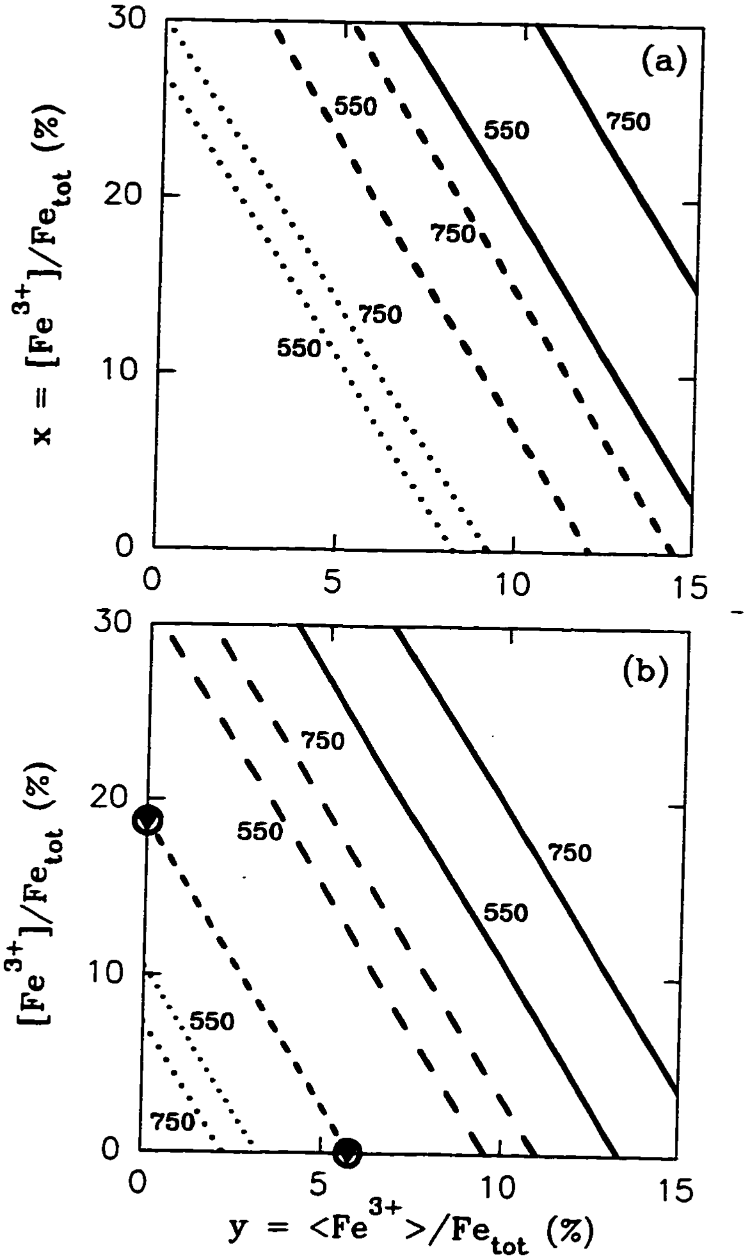

Figure 9.3: The effect of changing the α_o and α_t parameters (A = 7.640 Å, B = 2.188): (a) α_t=0 and α_o= 10×10^{-6} °C^{-1} (dotted lines), 25×10^{-6} °C^{-1} (dashed lines), 40×10^{-6} °C^{-1} (solid lines); (b) α_t=10×10^{-6} °C^{-1} and α_o = 10×10^{-6} °C^{-1} (dotted lines), 20×10^{-6} °C^{-1} (short-dashed lines: T=550 °C, filled triangles; T=750 °C, open circles), 35×10^{-6} °C^{-1} (dashed lines), 50×10^{-6} °C^{-1} (solid lines).

Having investigated the effect of various values for A, B, α_o and α_t, we now compare our site population measurements with the structural misfit model. In order to do so, we utilize MINUIT, a CERN-produced minimization package [30], in conjunction with a user-defined subroutine. The program minimizes a χ^2 by treating A, B, and α_o as fitting parameters and α_t as an imposed parameter. The χ^2 is defined as:

$$\chi^2 = \sum_i \left\{ [Fe^{3+}]_i(\text{theo}) - [Fe^{3+}]_i(\text{meas}) \right\} \tag{9.1}$$

where $[Fe^{3+}]_i$(theo) and $[Fe^{3+}]_i$(meas) are respectively the theoretical and measured [Fe^{3+}] site populations corresponding to a measured <Fe^{3+}> site population for a given sample (i refers to a particular sample). We covered the range of all acceptable α_t coefficients by imposing values between -5×10^{-6} and 20×10^{-6} °C^{-1}.

We only considered samples HK-596, HK-650, and HK-700. These samples were single-phase annite produced through equilibrations/syntheses with the same oxygen-fugacity buffer (C-CH$_4$). More importantly, these samples all have the same stoichiometry since no other phases occurred in the run products of these equilibrations.

Because we have the same number of experimental points and fitting parameters, we cannot use the above fitting process to assess the validity of our misfit model. Thus, the fitting process is only meant to compare our experimental data with our misfit model.

Results of the fitting process are tabulated in Table 9.1. When we compare the results associated to the different fits, we realize that as α_t increases, A and α_o increase and B decreases. This is, of course, consistent with the behaviour we established earlier for the model. Also, for imposed value of $\alpha_t >$ 10×10^{-6} °C^{-1}, the α_o parameters obtained are outside the accepted range for this expansion coefficient. Finally, we illustrate in Figure 9.4 that the (A,B) parameters deduced for each fit correspond to a very small region inside the range of acceptable (A,B) values that are consistent with the data of Hazen and Wones [17]. If we are ready to accept the misfit model as a fair representation of the reality, then the model suggests more precise values for (A,B). On the other end, we need a better measurement of the

(A,B) values to ascertain the validity of (or invalidate) the structural misfit model[2].

α_t ($\times10^{-6}\,{}^\circ C^{-1}$)	A (Å)	B (dimensionless)	α_o ($\times10^{-6}\,{}^\circ C^{-1}$)	$(\alpha_o - \alpha_t)$ ($\times10^{-6}\,{}^\circ C^{-1}$)	χ^2 ($\times10^{-6}$)
-5.0	7.626	2.117	18.1	23.1	8.827
0.0	7.634	2.102	29.5	29.5	8.271
5.0	7.644	2.091	39.9	34.9	8.258
10.0	7.654	2.085	48.3	38.3	16.880
15.0	7.666	2.065	60.9	45.9	10.120
20.0	7.677	2.048	72.6	50.6	9.206

Table 9.1: Results of the fitting process used to compare the site population measurements with the structural misfit model.

In Figure 9.5, we present the theoretical predictions corresponding to the fitted parameters of the lowest and highest value of χ^2. The agreement between the data and our structural misfit model is excellent. In addition, the precise position of a particular synthesis on its $\alpha = 0^\circ$ x-y line depends on secondary effects which are not elucidated by the present model.

In short, differential thermal expansion effects are significant and show potential for geothermometry in that they seem to explain our observations.

---

[2] See note added in proof.

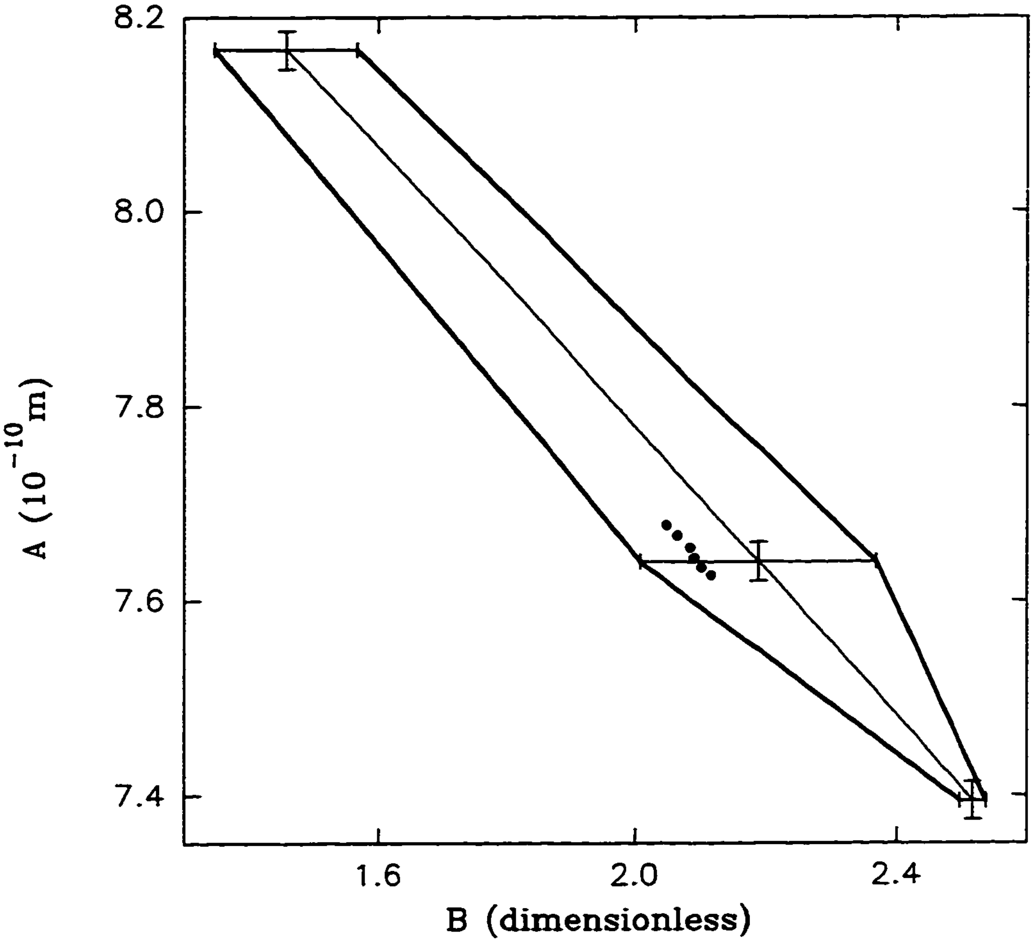

Figure 9.4: Range of acceptable (A,B) values (see note added in proof) that are consistent with the data of Hazen and Wones [17]. Dots are fitted (A,B) values obtained for the various imposed α_t coefficients.

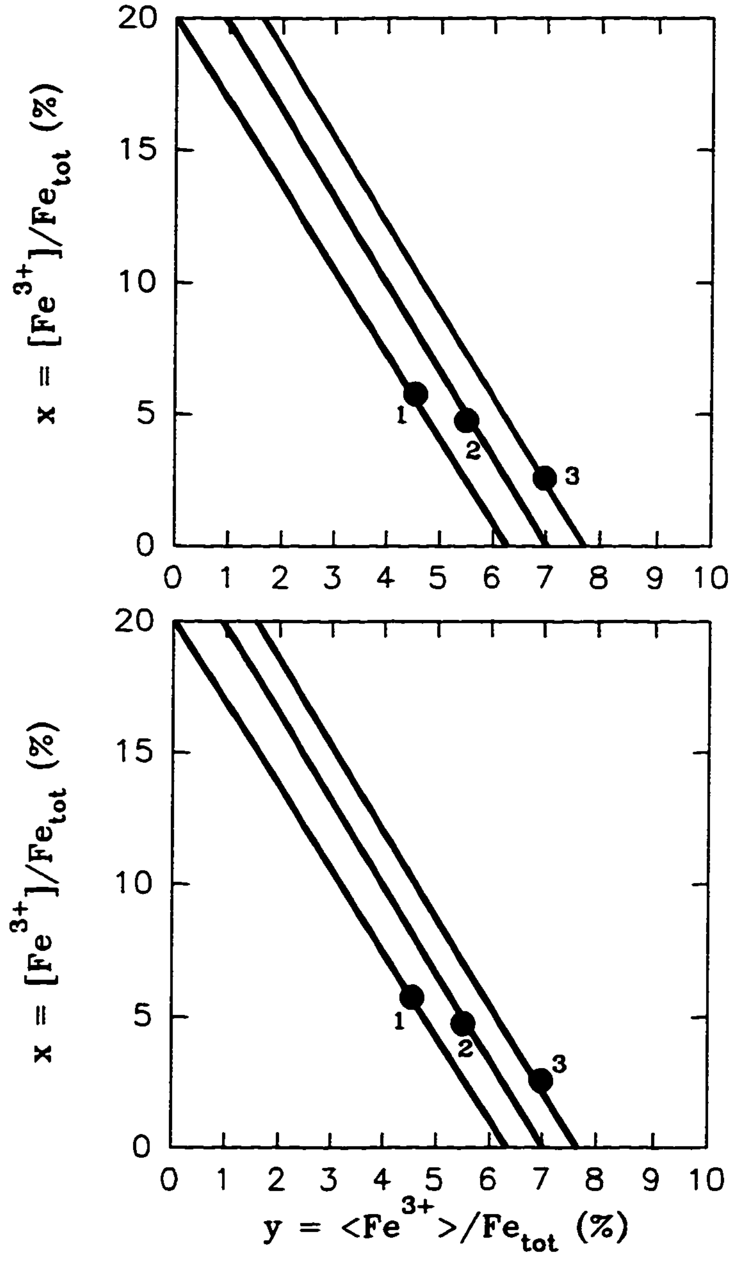

Figure 9.5: Theoretical predictions corresponding to fitted values of (A,B) and α_o for the lowest (top) and highest (bottom) χ^2 values obtained (see note added to proof). Samples are: 1 = HK-596, 2 = HK-650, 3 = HK-700.

Chapter 10. Conclusion

10.1 Summary

We measured the Fe^{3+} and Fe^{2+} site populations in nine annite samples synthesized using the C-CH_4 and Ni-NiO buffers, and various equilibration temperatures. By using temperatures over the entire stability range for annite, we have traced the evolution of $[Fe^{3+}]$ and $<Fe^{3+}>$ site populations and have obtained an experimental lowerbound on $\frac{Fe^{3+}}{Fe_{tot}}$.

The measurements were performed using the most recent MS data treatment and spectral analysis methods. These include (1) analytic methods for removing the spectral distortions associated with the effects of absorber thickness and (2) a powerful Voigt-based fitting method that allows arbitrary shape quadrupole splitting distributions for each site. We obtained site populations with precisions of 0.2–1% of Fe_{tot}, whereas the generally accepted limit is 1–5% of Fe_{tot}. This allows simple crystal chemical models to be tested accurately.

In light of the experimental results, temperature is seen to have a systematic effect that is understood in terms of differential thermal expansion between the octahedral and tetrahedral sheets. To explain this effect, we proposed a structural misfit model for annite mica that includes: definite predictions on the $[Fe^{3+}]$ and $<Fe^{3+}>$ site populations, cation size dependant octahedral flattening, and the effect of octahedral/tetrahedral sheet differential thermal expansion.

In the development of our structural misfit model, we made the assumption that the conditions at synthesis were such as to produce no vacancies in the octahedral sites. We supposed that the oxydation of Fe^{2+} to Fe^{3+} occurred via loss of structural H:

$$Fe^{2+}(OH)_2^- \Rightarrow Fe^{3+}O^{2-}(OH)^- + H\nearrow.$$

This is one of the preferred scenarios to account for the formation of Fe^{3+}, as it is predominant during oxydation in air [31, 32]. We also considered the intracrystalline exchange reaction:

$$[\mathrm{Fe}^{3+}] + <\mathrm{Al}^{3+}> \rightleftharpoons [\mathrm{Al}^{3+}] + <\mathrm{Fe}^{3+}> .$$

Through these mechanisms, we were able to construct our structural misfit model such that it establishes a link between the measured values of the $[\mathrm{Fe}^{3+}]$ and $<\mathrm{Fe}^{3+}>$ site populations, and the effect of differential thermal expansion between the octahedral and tetrahedral layers[1].

10.2 Suggestions for future work

Another mechanism to achieve the charge balance necessary for the substitution of Fe^{2+} by Fe^{3+} involves the formation of octahedral vacancies:

$$3[\mathrm{Fe}^{2+}] \Rightarrow 2[\mathrm{Fe}^{3+}] + [\quad]_{vacancy}.$$

According to Redhammer et al. [33] and Rebbert et al. [34], this mechanism plays an important role for charge balance.

If we knew the effective radius of an octahedral vacancy, we could incorporate this parameter into our structural misfit model. A study of the impact of this mechanism in addition to the differential thermal expansion effects could then be made. To measure the effective size of an octahedral vacancy, we propose the synthesis of samples with known amounts of octahedral vacancies.

On another perspective, we can also extend our structural misfit model to investigate other micas such as the annite–phlogopite and annite–siderophyllite solid solutions. We then have to modify the present version of the model to include parameters such as the Fe-Mg and Fe-Al ratios. In this line of research, we use the structural misfit model as a starting point for understanding the crystal chemistry of micas. However, as suggested by Lalonde et al. [35], local distortions may play an important role in addition to uniform lateral expansion.

---

[1] See note added in proof.

Note added in proof

After the submission of this thesis, we performed a self-consistency check of our theoretical model and found that we made a mistake in the determination of the range of acceptable (A,B) values. In fact, the (A,B) values are much more correlated. On Figure 10.1, we present a revised version for the range of acceptable (A,B) values that are consistent with the data of Hazen and Wones [17]. Squares represent examples of (A,B) values that give acceptable fits to the data of Hazen and Wones. Dots are fitted (A,B) values obtained from our structural misfit model.

As we can see from Figure 10.1, the (A,B) values obtained from our misfit model do not lie within the range of acceptable (A,B) values. On Figure 10.2, we illustrate this by showing the lines which correspond to the fitted (A,B) values along with Hazen and Wones' data (filled circles). The filled triangles represent the three single phase annite samples which were compared to our misfit model (HK-596, HK-650, and HK-700).

Considering Figure 10.2, we realize that our misfit model does not explain our experimental observations as well as we originally concluded. The fitted (A,B) values do not correspond to either Hazen and Wones' data or our evaluation of the lattice parameter b and average octahedral cation radius $[R]$ for our annite specimens. Nevertheless, we believe our misfit model still has potential and that we need to investigate further in order to understand the more subtle effects pertaining to the crystal chemistry involved.

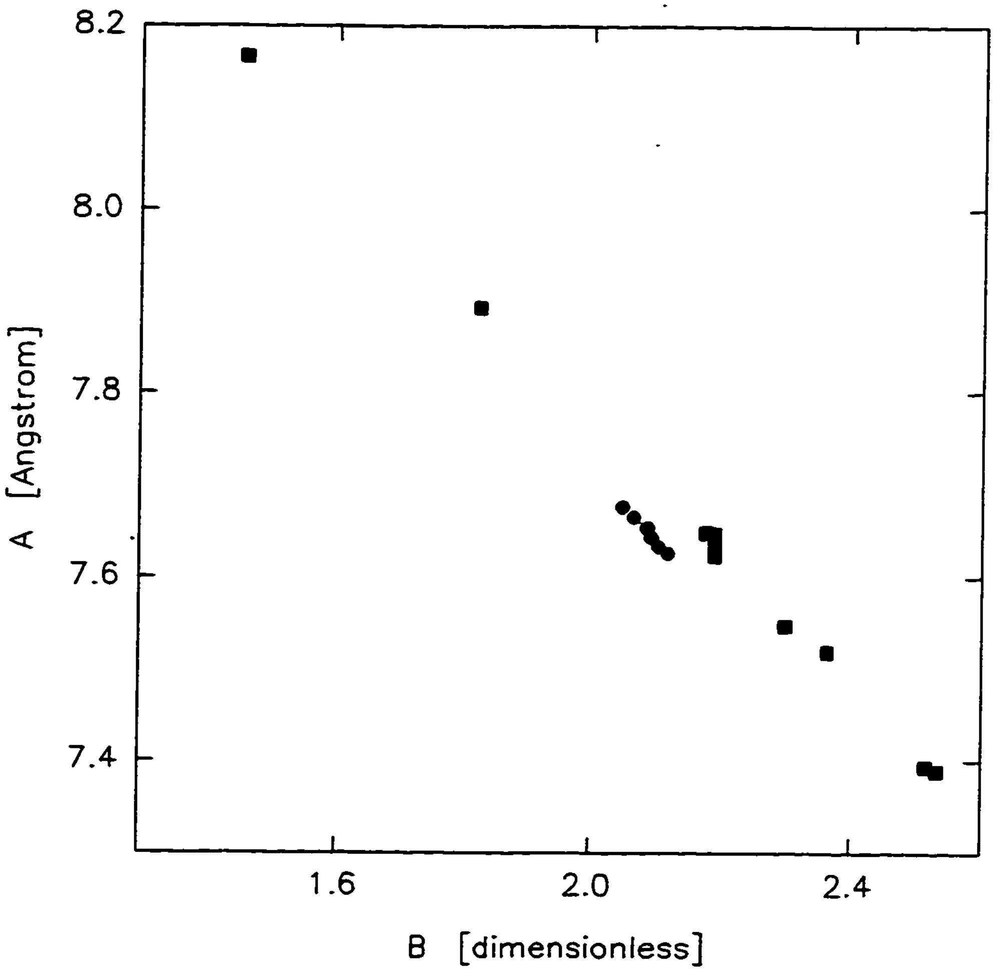

Figure 10.1: Revised range of acceptable (A,B) values that are consistent with the data of Hazen and Wones [17]. Squares represent examples of (A,B) values that give acceptable fits to the data of Hazen and Wones. Dots are fitted (A,B) values obtained from our structural misfit model.

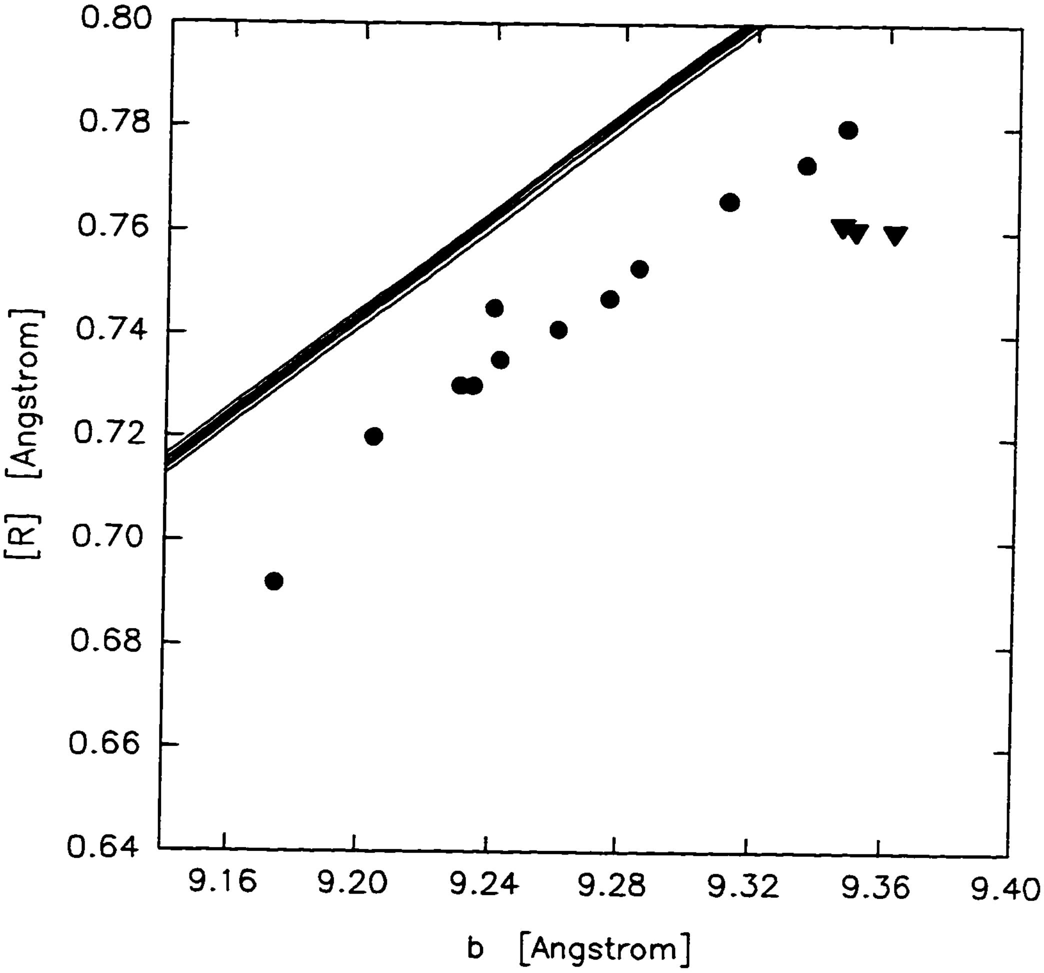

Figure 10.2: Reproduction of Hazen and Wones' data [17] (filled circles) along with our evaluation of the lattice parameter b and average octahedral cation radius $[R]$ for our annite specimens (filled triangles). The solid lines arise from the fitted values of (A,B) from our structural misfit model.

Appendix A. Parameters of the Voigt Fits Used for Thickness-corrections

Sample /BG(MC/Ch)	Line	Height (Counts)	σ (mm/s)	Center (mm/s)	χ^2_{red} /Lorentzian HWHM (mm/s)
HK-550	1	120660	0.12041	-0.09840	1.104
	2	53958	0.04392	-0.19323	
	3	85479	0.36080	0.09209	
	4	58609	0.04428	2.45246	
	5	37973	0.51312	2.19534	
	6	8755	0.11715	0.98121	
	7	104397	0.10535	2.35353	
	8	11273	0.17198	2.44800	
	9	11592	0.25871	0.95953	
	10	8879	0.13578	2.10616	
	11	1209	0.16329	-1.71448	
	12	1518	0.00035	0.41330	
	13	3847	0.33853	0.72763	
0.585517	14	1641	0.31284	-1.01413	0.100^f

^{f} This parameter was frozen during fit.

Table A.1: Voigt fit parameters for sample HK-550.

Sample /BG(MC/Ch)	Line	Height (Counts)	σ (mm/s)	Center (mm/s)	χ^2_{red} /Lorentzian HWHM (mm/s)
HK-596	1	138829	0.06921	-0.18112	1.052
	2	84038	0.55951	0.24625	
	3	92743	0.16077	2.31380	
	4	124077	0.07745	2.43524	
	5	5624	0.06653	1.85442	
	6	4794	0.12356	1.06943	
	7	6214	0.15619	1.55754	
	8	58290	0.11005	0.00789	
	9	11006	0.00091	-0.02666	
	10	9620	0.40969	2.53013	
	11	3830	0.00005	-0.42984	
	12	3596	0.10479	0.96148	
	13	5984	0.01006	0.41340	
	14	6350	0.49356	3.35846	
	15	4944	0.14938	2.77147	
	16	2617	0.00128	0.19170	
0.625397	17	6150	0.68822	-1.69752	0.100^f
HK-650	1	64677	0.03580	-0.20362	1.020
	2	142868	0.20333	-0.05223	
	3	119301	0.10246	2.36729	
	4	52334	0.04016	2.44142	
	5	2544	0.54763	-2.01745	
	6	77502	1.37481	1.17095	
	7	1733	0.03586	-0.73818	
	8	10501	0.03915	0.43243	
	9	63809	0.06417	-0.09782	
	10	7800	0.11659	0.92302	
	11	7871	0.11179	0.60231	
0.753196	12	67825	0.23906	2.32232	0.097^f

^{f} This parameter was frozen during fit.

Table A.2: Voigt fit parameters for samples HK-596 and HK-650.

Sample /BG(MC/Ch)	Line	Height (Counts)	σ (mm/s)	Center (mm/s)	χ^2_{red} /Lorentzian HWHM (mm/s)
HK-700	1	132832	0.06067	-0.17811	1.216
	2	105224	0.13488	-0.01901	
	3	136490	0.12155	2.33833	
	4	87681	0.05138	2.42560	
	5	1831	0.24437	0.87028	
	6	15399	0.06043	0.43192	
	7	4661	0.09445	2.00030	
	8	1386	0.05119	0.23064	
	9	68779	0.56602	0.14842	
	10	51272	0.53667	2.18048	
	11	11357	0.00005	-0.03448	
	12	571	0.04741	0.74941	
	13	2608	0.10694	0.82055	
	14	2080	0.16557	1.11651	
	15	1299	0.14779	-1.58161	
	16	1685	0.08753	-0.03383	
0.852401	17	802	0.09336	0.98061	0.100[f]
HK-750	1	20774	0.65589	0.04041	0.974
	2	48974	0.06392	-0.10686	
	3	44950	0.03124	-0.20713	
	4	122642	0.18395	-0.05726	
	5	15653	0.07126	0.42378	
	6	12026	0.24282	0.89039	
	7	38170	0.44339	2.17318	
	8	57029	0.09085	2.32600	
	9	67502	0.04903	2.43450	
0.634365	10	53540	0.19099	2.34637	0.100[f]

[f] This parameter was frozen during fit.

Table A.3: Voigt fit parameters for samples HK-700 and HK-750.

Sample /BG(MC/Ch)	Line	Height (Counts)	σ (mm/s)	Center (mm/s)	χ^2_{red} /Lorentzian HWHM (mm/s)
HK-NNO	1	95241	0.05633	-0.18018	1.378
	2	68272	0.10640	2.26990	
	3	94273	0.39473	0.12012	
	4	131412	0.06019	2.43163	
	5	130211	0.12114	-0.07341	
	6	64326	0.51627	2.24916	
	7	12228	0.65397	-0.76509	
	8	860	0.00026	-0.46230	
	9	3628	0.01877	0.46765	
	10	8369	0.18066	1.12088	
	11	11214	0.14403	0.87673	
0.725601	12	22101	0.04688	2.31957	0.100^f
RB-22	1	50174	0.00050	-0.26850	0.924
	2	43353	0.02314	2.66235	
	3	166506	0.08306	2.43769	
	4	323443	0.18883	-0.10007	
	5	116555	0.07155	-0.18239	
	6	36458	0.69422	-0.16949	
	7	181237	0.14378	2.35554	
	8	99378	0.47646	2.22749	
	9	20288	0.06367	0.41706	
1.259313	10	41344	0.33564	0.73612	0.097^f

^{f} This parameter was frozen during fit.

Table A.4: Voigt fit parameters for samples HK-NNO and RB-22.

Sample /BG(MC/Ch)	Line	Height (Counts)	σ (mm/s)	Center (mm/s)	χ^2_{red} /Lorentzian HWHM (mm/s)
RB-25	1	54747	0.07879	0.42844	0.948
	2	13259	0.00500	2.49420	
	3	154511	0.26096	2.35238	
	4	54352	0.00700	2.64601	
	5	88090	0.00600	-0.27736	
	6	134693	1.53234	1.03772	
	7	134938	0.14559	-0.01562	
	8	276429	0.06644	-0.16846	
	9	3069	0.00709	0.66720	
	10	159081	0.06791	2.43501	
	11	8976	0.00040	0.26534	
	12	22452	0.00500	-0.43242	
	13	15632	0.14845	-0.58466	
	14	27030	0.17927	0.84871	
	15	178185	0.10398	2.34610	
	16	51009	0.00600	-0.01054	
	17	36557	0.00688	0.12735	
1.456788	18	36360	0.57497	2.12380	0.097^f
RB-7	1	170528	0.08355	-0.05493	0.900
	2	30571	0.00400	2.48910	
	3	102486	0.03840	-0.24030	
	4	89798	1.37663	1.11434	
	5	8298	0.02338	0.45971	
	6	3727	0.08197	0.95937	
	7	7817	0.00050	-0.43443	
	8	71943	0.31020	2.29475	
	9	67751	0.46072	0.15833	
	10	118058	0.10083	2.31502	
	11	41379	0.00400	-0.15107	
	12	100665	0.05105	2.40568	
	13	31480	0.10081	0.39474	
	14	23645	0.00281	0.13741	
0.859379	15	244410	0.00500	2.63367	0.097^f

^{f} This parameter was frozen during fit.

Table A.5: Voigt fit parameters for samples RB-25 and RB-7.

Appendix B. Analysis of the XRD diffractograms

Powder XRD patterns were obtained for all samples using a Philips X'Pert PW3710 automated powder diffractometer (CuK_α radiation), except for sample RB-22 which was collected with a Gandolfi camera that used CoK_α radiation. The calculations of d-spacings were computed using wavelenghts of 1.5418Å for the CuK_α radiation, 1.79021Å for CoK_α, 1.54056Å and 1.54439Å for CuK_{α_1} and CuK_{α_2}, respectively. As for the unit cell refinements, they were calculated with a version of the least-squares program of Appleman and Evans [36]. The refinements are given in Table 5.3.

For calculation of the lattice parameters (a, b ,c, and γ) between 25 and 35 reflections were used for each sample. The indexing of the annite peaks was done on the basis of XRD powder patterns of micas reported by Bailey [37] (Synthetic annite (Eugster and Wones [38]), Ferrian biotite-1M (lepidomelane), Manganoan phlogopite-1M), single crystal XRD measurement of a natural annite done by Guggenheim (unpublished), and an XRD powder pattern of annite HK-NNO obtained by Murad (unpublished) using a CoK_{α_1} Guinier LP-corrected camera. In this manner, we were able to assign between 40 and 55 hkl values in each of the XRD patterns.

We identified other phases by comparing our XRD powder diffractograms with the ICDD patterns reported in Table 5.2 of the present work. If there were many of the lines of these phases present in our diffractograms, we then could established the presence of a particular phase and used its ICDD card to identify other peaks that might have been recorded in our powder XRD measurements.

The quantification of impurity phases is a severe problem that we adressed in the following manner. In the case of sylvite, we estimated its relative amount with the EDS picture obtained on the SEM. Since this phase has a higher crystal symmetry than annite, its diffractive power is much higher. Hence we could not use the XRD intensities recorded to calculate its relative amount. We quantified the sanidine and fayalite amount by dividing the intensity corresponding to their highest peak by the intensity recorded for the annite 001 reflection. The intensities were evaluated with the PC-APD software package provided on the Philips diffractometer.

Angle (°2Θ)	d-spacing (Å)	Intensity (counts)	Peak designation	Comments
8.740	10.1172	3376	Ann 001	
13.625	6.4989	37	Sa	
17.475	5.0748	182	Ann 002	
19.020	4.6659	117	Ann 020	
19.225	4.6166	83	Ann 110	
19.885	4.4649	14	(R)Ann 012	
21.005	4.2292	69	Sa	
22.315	3.9838	94	Ann 111	
22.575	3.9385	66	Sa	
23.515	3.7832	320	Sa	
23.970	3.7124	207	Ann $11\bar{2}$	
24.585	3.6209	21	Sa	
25.895	3.4406	310	Ann 022	
26.305	3.3879	949	Ann 003	
26.825	3.3234	412	Sa	
27.175	3.2814	64	Sa	
27.675	3.2232	1362	Sa	
28.020	3.1843	266	Ann 112	
28.385	3.1442	681	Syl	
29.090	3.0696	18	?	
29.835	2.9946	88	Sa	
30.225	2.9569	180	Ann $11\bar{3}$	
30.765	2.9062	21	Sa	
30.960	2.8883	45	Sa	
31.955	2.8006	14	Sa	
32.655	2.7422	94	Ann 023	
33.695	2.6599	751	Ann 200,$13\bar{1}$	
34.345	2.6110	41	Sa	
34.820	2.5765	71	Sa	
35.315	2.5415	207	Ann 004,131,$20\bar{2}$	

(R) Tentative indice assigned, based on the unit cell refinement. This reflection was observed for a natural annite single crystal measurement (Guggenheim; unpublished).

Table B.1: XRD peaks observed for annite HK-550.

Angle (°2Θ)	d-spacing (Å)	Intensity (counts)	Peak designation	Comments
36.375	2.4698	576	Ann 201,$13\bar{2}$	
37.325	2.4091	41	?Sa	
37.710	2.3854	21	(R)Ann 211,$\bar{1}14$	
38.635	2.3304	42	Ann $22\bar{1}$	
39.260	2.2947	123	Ann 132,$20\bar{3}$	
40.585	2.2228	548	Syl	
40.970	2.2028	269	Ann 202,$13\bar{3}$	
42.500	2.1270	22	(R)Ann $\bar{1}41$,042	
43.680	2.0722	18	Sa	
44.820	2.0221	146	Ann $20\bar{4}$,133	
45.970	1.9742	29	Sa	
46.950	1.9352	56	Ann 203,$13\bar{4}$	
49.145	1.8538	10	?	
49.730	1.8334	10	?	
50.245	1.8158	53	Syl	
50.850	1.7956	19	Sa	
51.800	1.7649	15	(R)Ann 115	
53.145	1.7233	10	(R)Ann 151,044	
54.090	1.6954	146	Ann 006,204,$13\bar{5}$	
54.975	1.6702	18	Ann 311,$31\bar{3}$	
56.120	1.6388	17	Ann 152,$24\bar{3}$	
57.430	1.6045	11	An 242,$15\bar{3}$	
58.655	1.5739	25	Syl	
59.235	1.5599	202	Ann $20\bar{6}$,135,$33\bar{1}$,060	
59.990	1.5420	72	Ann 330,061,$33\bar{2}$	
61.800	1.5011	18	?	
62.215	1.4921	25	Ann 062,331	

(R) Tentative indice assigned, based on the unit cell refinement. This reflection was observed for a natural annite single crystal measurement (Guggenheim; unpublished).

Table B.2: (cont'd) XRD peaks observed for annite HK-550.

Angle (°2Θ)	d-spacing (Å)	Intensity (counts)	Peak designation	Comments
8.775	10.0769	3069	Ann 001	
17.505	5.0662	172	Ann 002	
19.040	4.6611	94	Ann 020	
19.255	4.6095	128	Ann 110	
19.930	4.4549	26	(R)Ann 012	
20.925	4.2452	10	?Sa	
22.375	3.9733	98	Ann 111	
24.010	3.7063	196	Ann $11\bar{2}$	
25.970	3.4309	272	Ann 022	
26.355	3.3816	812	Ann 003	
26.855	3.3198	102	?Sa	
28.065	3.1793	250	Ann 112	
28.450	3.1372	1239	Syl	
30.290	2.9507	166	Ann $11\bar{3}$	
32.695	2.7389	90	Ann 023	
33.770	2.6541	906	Ann 200,$13\bar{1}$	
34.430	2.6048	32	?Sa	
35.345	2.5394	196	Ann 004,131,$20\bar{2}$	
36.460	2.4643	645	Ann 201,$13\bar{2}$	
37.830	2.3781	21	(R)Ann 211,$\bar{1}14$	
38.695	2.3269	61	Ann $22\bar{1}$	
39.325	2.2911	132	Ann 132,$20\bar{3}$	
40.580	2.2231	240	Syl	
41.000	2.2013	279	Ann 202,$13\bar{3}$	
42.580	2.1232	14	(R)Ann 042	
42.900	2.1081	17	?	
44.850	2.0208	125	Ann 133,$20\bar{4}$	
47.020	1.9325	50	Ann 203,$13\bar{4}$	
49.180	1.8526	6	?	
50.215	1.8168	59	Syl	

(R) Tentative indice assigned, based on the unit cell refinement. This reflection was observed for a natural annite single crystal measurement (Guggenheim; unpublished).

Table B.3: XRD peaks observed for annite HK-596.

Angle (°2Θ)	d-spacing (Å)	Intensity (counts)	Peak designation	Comments
50.350	1.8122	2	Syl	
51.305	1.7807	9	?Sa	
51.795	1.7650	14	(R)Ann 115	
53.130	1.7238	13	(R)Ann 151	
54.100	1.6952	164	Ann $006,204,13\bar{5}$	
55.110	1.6665	22	Ann $311,31\bar{3}$	
56.225	1.6360	18	Ann $152,24\bar{3}$	
57.500	1.6027	19	Ann $242,15\bar{3}$	
58.700	1.5715	96	Syl	$CuK_{\alpha 1}$ radiation.
58.840	1.5620	128	Syl	$CuK_{\alpha 2}$ radiation.
59.305	1.5582	225	Ann $060,135,33\bar{1},20\bar{6}$	
60.065	1.5403	132	Ann $330,061,33\bar{2}$	
62.435	1.4874	22	Ann 062,331	
64.305	1.4486	11	Ann 007	
66.030	1.4149	15	Ann $063,332,33\bar{4}$	
66.430	1.4062	45	Syl	$CuK_{\alpha 1}$ radiation.
66.660	1.4054	53	Syl	$CuK_{\alpha 2}$ radiation.
67.920	1.3800	35	Ann $20\bar{7}$	
68.140	1.3761	30	Ann 136	
70.020	1.3437	36	Ann $40\bar{2},260$	
70.900	1.3292	27	?	
71.625	1.3175	26	?	
73.485	1.2887	19	?	
73.715	1.2852	59	Syl	
74.690	1.2708	13	?	

(R) Tentative indice assigned, based on the unit cell refinement. This reflection was observed for a natural annite single crystal measurement (Guggenheim; unpuplished).

Table B.4: (cont'd) XRD peaks observed for annite HK-596.

Angle (°2Θ)	d-spacing (Å)	Intensity (counts)	Peak designation	Comments
8.765	10.0884	2788	Ann 001	
17.495	5.0690	139	Ann 002	
19.030	4.6635	110	Ann 020	
19.265	4.6071	135	Ann 110	
19.930	4.4549	29	(R)Ann 012	
21.000	4.2302	8	?Sa	
22.390	3.9707	83	Ann 111	
23.075	3.8543	7	?Sa	
23.505	3.7848	71	?Sa	
24.030	3.7033	202	Ann $11\bar{2}$	
25.955	3.4328	276	Ann 022	
26.340	3.3835	829	Ann 003	
26.840	3.3216	49	?Sa	
27.665	3.2244	50	?Sa	
28.075	3.1782	259	Ann 112	
28.415	3.1410	906	Syl	
29.160	3.0624	18	?	
29.865	2.9917	28	?Sa	
30.245	2.9550	169	Ann $11\bar{3}$	
32.715	2.7373	88	Ann 023	
33.750	2.6557	967	Ann 200,$13\bar{1}$	
34.440	2.6040	20	?Sa	
35.325	2.5408	185	Ann 004,131,$20\bar{2}$	
36.430	2.4662	676	Ann 201,$13\bar{2}$	
37.760	2.3824	21	(R)Ann 211,$\bar{1}14$	
38.645	2.3298	53	Ann $22\bar{1}$	
39.280	2.2936	142	Ann 132,$20\bar{3}$	
40.580	2.2231	313	Syl	
40.975	2.2026	282	Ann 202,$13\bar{3}$	
42.815	2.1121	8	(R)Ann 042	
44.875	2.0198	142	Ann 133,$20\bar{4}$	

(R) Tentative indice assigned, based on the unit cell refinement. This reflection was observed for a natural annite single crystal measurement (Guggenheim; unpublished).

Table B.5: XRD peaks observed for annite HK-650.

Angle (°2Θ)	d-spacing (Å)	Intensity (counts)	Peak designation	Comments
46.980	1.9341	50	Ann 203,$13\bar{4}$	
48.010	1.8950	2	?Sa	
49.170	1.8529	6	?	
50.215	1.8168	67	Syl	
51.820	1.7642	13	(R)Ann 115	
53.245	1.7203	8	(R)Ann 151,044	
54.150	1.6937	154	Ann 006,204,$13\bar{5}$	
55.020	1.6690	19	Ann 311,$31\bar{3}$	
56.195	1.6368	18	Ann 152,$24\bar{3}$	
57.455	1.6039	12	Ann 242,$15\bar{3}$	
58.660	1.5725	30	Syl	CuK$_{\alpha_1}$ radiation.
58.840	1.5720	61	Syl	CuK$_{\alpha_2}$ radiation.
59.310	1.5581	219	Ann 060,135,$20\bar{6}$,$33\bar{1}$	
60.040	1.5409	72	Ann 330,061,$33\bar{2}$	
61.025	1.5183	0	?	
62.305	1.4902	24	Ann 062,331	
64.110	1.4525	11	Ann 007	
66.000	1.4154	20	Ann 063,332,$33\bar{4}$	
66.405	1.4066	110	Syl	CuK$_{\alpha_1}$ radiation.
66.620	1.4061	67	Syl	CuK$_{\alpha_2}$ radiation.
67.950	1.3795	41	Ann $20\bar{7}$	
68.070	1.3773	35	Ann 136	
69.975	1.3444	50	Ann $40\bar{2}$,260	
70.865	1.3297	32	?	
71.545	1.3188	31	?	
73.710	1.2853	31	Syl	
74.645	1.2715	13	?	
76.655	1.2431	7	?	
77.300	1.2343	12	?	
78.945	1.2127	9	?	

(R) Tentative indice assigned, based on the unit cell refinement. This reflection was observed for a natural annite single crystal measurement (Guggenheim; unpublished).

Table B.6: (cont'd) XRD peaks observed for annite HK-650.

Angle (°2Θ)	d-spacing (Å)	Intensity (counts)	Peak designation	Comments
8.700	10.1636	412	An 001	
17.430	5.0878	14	An 002	
19.000	4.6708	6	An 020	
19.190	4.6250	12	An 110	
22.305	3.9856	8	An 111	
23.945	3.7162	17	An $11\bar{2}$	
25.880	3.4426	21	An 022	
26.285	3.3905	71	An 003	
27.035	3.2981	0	?Sa	
28.000	3.1866	18	An 112	
28.355	3.1475	61	Syl	
29.285	3.0496	3	?	
30.220	2.9573	11	An $11\bar{3}$	
32.580	2.7483	6	An 023	
33.685	2.6606	71	An $200,13\bar{1}$	
34.320	2.6129	0	?Sa	
35.285	2.5436	14	An $004,131,20\bar{2}$	
36.345	2.4718	45	An $201,13\bar{2}$	
38.500	2.3383	14	An $22\bar{1}$	
39.255	2.2950	9	An $132,20\bar{3}$	
40.520	2.2262	14	Syl	
40.920	2.2054	18	An $202, 13\bar{3}$	

N.B. A very small amount of sample (<5 mg) was used in the acetone smear.

Table B.7: XRD peaks observed for annite HK-700.

Angle (°2Θ)	d-spacing (Å)	Intensity (counts)	Peak designation	Comments
42.450	2.1294	3	(R)Ann 042	
43.700	2.0713	2	?	
44.495	2.0361	12	Ann 005	
44.785	2.0236	12	Ann 133,20$\bar{4}$	
46.970	1.9344	3	Ann 203,13$\bar{4}$	
50.240	1.8160	2	Syl	
51.395	1.7778	1	(R)Ann 223	
54.080	1.6957	11	Ann 006,204,13$\bar{5}$	
55.005	1.6694	2	Ann 311,31$\bar{3}$	
56.100	1.6394	1	Ann 152,24$\bar{3}$	
57.495	1.6029	0	Ann 242,15$\bar{3}$	
59.215	1.5604	18	Ann 060,135,33$\bar{1}$,20$\bar{6}$	
59.965	1.5426	6	Ann 330,061,33$\bar{2}$	
62.215	1.4921	1	Ann 062,331	
64.310	1.4485	3	Ann 007	
65.875	1.4178	1	Ann 063,332,33$\bar{4}$	
66.380	1.4083	5	Syl	
67.885	1.3806	3	Ann 20$\bar{7}$,136	
69.875	1.3461	4	Ann 40$\bar{2}$,260	
70.935	1.3286	3	?	
71.575	1.3183	2	?	
73.400	1.2899	0	?	
73.695	1.2855	18	Syl	
74.695	1.2708	0	?	
77.620	1.2300	4	?	

(R) Tentative indice assigned, based on the unit cell refinement. This reflection was observed for a natural annite single crystal measurement (Guggenheim; unpublished).
N.B. A very small amount of sample (<5 mg) was used in the acetone smear.

Table B.8: (cont'd)XRD peaks observed for annite HK-700.

Angle (°2Θ)	d-spacing (Å)	Intensity (counts)	Peak designation	Comments
8.715	10.1462	3709	Ann 001	
13.290	6.6619	139	Sa	
17.495	5.0690	269	Ann 002	
18.980	4.6757	213	Ann 020	
19.240	4.6130	144	Ann 110	
22.290	3.9883	92	Ann 111	
22.575	3.9385	85	Sa	
23.495	3.7864	980	Sa	
23.985	3.7101	259	Ann $11\bar{2}$	
25.885	3.4419	216	Ann 022	
26.315	3.3867	620	Ann 003	
26.770	3.3301	169	Sa	
27.360	3.2596	132	Sa	
27.575	3.2347	202	Sa	
28.000	3.1866	231	Ann 112	
28.400	3.1426	1296	Syl	
28.660	3.1147	346	Ann	Annite peak as observed by Eugster and Wones [38]
30.240	2.9554	137	Ann $11\bar{3}$	
32.565	2.7495	79	Ann 023	
33.295	2.6909	58	?	
33.705	2.6591	392	Ann $200,13\bar{1}$	
34.385	2.6081	69	Sa	
34.770	2.5801	72	Sa	
35.330	2.5404	96	Ann $004,131,20\bar{2}$	
36.390	2.4688	250	Ann $201,13\bar{2}$	
37.670	2.3878	36	(R)Ann $211,\bar{1}14$	
39.260	2.2947	77	Ann $132,20\bar{3}$	
39.535	2.2794	48	Ann 041	
40.580	2.2231	55	Syl	
40.995	2.2015	114	Ann $202,13\bar{3}$	
42.920	2.1071	48	(R)Ann $\bar{1}41,042$	

(R) Tentative indice assigned, based on the unit cell refinement. This reflection was observed for a natural annite single crystal measurement (Guggenheim; unpublished).

Table B.9: XRD peaks observed for annite HK-750.

Angle (°2Θ)	d-spacing (Å)	Intensity (counts)	Peak designation	Comments
43.505	2.0802	34	Sa	
44.785	2.0236	56	Ann 133,20$\bar{4}$	
45.970	1.9742	27	Sa	
46.890	1.9376	31	Ann 203,13$\bar{4}$	
49.180	1.8526	20	?	
50.210	1.8170	40	Syl	
50.770	1.7982	20	Sa	
51.685	1.7685	21	(R)Ann 115	
52.555	1.7413	27	?	
54.105	1.6950	53	Ann 006,204,13$\bar{5}$	
55.040	1.6684	18	Ann 311,31$\bar{3}$	
58.745	1.5704	37	Syl	CuK$_{\alpha_1}$ radiation.
58.825	1.5724	30	Syl	CuK$_{\alpha_2}$ radiation.
59.215	1.5604	74	Ann 060,33$\bar{1}$	
59.400	1.5559	100	Ann 135,20$\bar{6}$	
59.985	1.5422	19	Ann 330,061,33$\bar{2}$	
62.320	1.4899	3	Ann 062,331	
63.955	1.4557	3	Ann 007	
66.425	1.4074	19	Syl	
67.930	1.3798	15	Ann 20$\bar{7}$	
68.080	1.3772	15	Ann 136	
69.885	1.3460	21	Ann 260,40$\bar{2}$	
71.535	1.3189	23	?	

(R) Tentative indice assigned, based on the unit cell refinement. This reflection was observed for a natural annite single crystal measurement (Guggenheim; unpublished).

Table B.10: (cont'd) XRD peaks observed for annite HK-750.

Angle (°2Θ)	d-spacing (Å)	Intensity (counts)	Peak designation	Comments
8.715	10.1462	1739	Ann 001	
9.460	9.3487	76	?	
17.455	5.0806	74	Ann 002	
19.040	4.6611	52	Ann 020	
19.270	4.6059	71	Ann 110	
19.880	4.4660	12	(R)Ann 012	
20.885	4.2533	6	?	
22.330	3.9812	42	Ann 111	
23.970	3.7124	98	Ann 11$\bar{2}$	
24.945	3.5695	11	?	
25.885	3.4419	123	Ann 022	
26.295	3.3892	420	Ann 003	
26.950	3.3083	15	?	
28.025	3.1834	114	Ann 112	
28.375	3.1453	250	Syl	
28.625	3.1184	144	Ann	Annite peak as observed by Eugster and Wones [38].
30.255	2.9540	72	Ann 11$\bar{3}$	
32.655	2.7422	44	Ann 023	
33.735	2.6568	428	Ann 200,13$\bar{1}$	
34.360	2.6099	14	?	
35.280	2.5439	81	Ann 004,131,20$\bar{2}$	
36.405	2.4679	276	Ann 201,13$\bar{2}$	
37.750	2.3830	10	(R)Ann 211,$\bar{1}$14	
38.590	2.3330	21	Ann 22$\bar{1}$	
39.285	2.2933	53	Ann 132,20$\bar{3}$	
40.560	2.2241	88	Syl	
40.985	2.2020	114	Ann 202,13$\bar{3}$	
42.675	2.1187	4	(R)Ann 042	

(R) Tentative indice assigned, based on the unit cell refinement. This reflection was observed for a natural annite single crystal measurement (Guggenheim; unpublished).

Table B.11: XRD peaks observed for annite HK-NNO.

Angle (°2Θ)	d-sapcing (Å)	Intensity (counts)	Peak designation	Comments
44.860	2.0204	53	Ann 133,20$\bar{4}$	
46.920	1.9364	16	Ann 203,13$\bar{4}$	
48.610	1.8730	4	?	
50.215	1.8168	14	Syl	
51.840	1.7636	4	(R)Ann 115	
54.085	1.6956	55	Ann 006,204,13$\bar{5}$	
54.975	1.6702	7	Ann 311,31$\bar{3}$	
56.235	1.6358	7	Ann 152,24$\bar{3}$	
57.560	1.6012	4	Ann 242,15$\bar{3}$	
59.280	1.5588	77	Ann 060,33$\bar{1}$	
59.440	1.5550	56	Ann 135,20$\bar{6}$	
60.060	1.5404	28	Ann 330,061,33$\bar{2}$	
62.305	1.4902	8	Ann 062,331	
64.015	1.4544	5	Ann 007	
66.080	1.4139	6	Ann 063,332,33$\bar{4}$	
66.390	1.4081	11	Syl	
67.860	1.3811	14	Ann 136,20$\bar{7}$	
69.980	1.3444	15	Ann 40$\bar{2}$,260	
70.990	1.3277	12	?	
71.570	1.3184	10	?	
73.585	1.2872	6	Syl	
74.585	1.2724	4	?	
77.205	1.2356	3	?	
79.010	1.2118	2	?	
84.480	1.1467	3	?	
88.935	1.1005	2	?	

(R) Tentative indice assigned, based on the unit cell refinement. This reflection was observed for a natural annite single crystal measurement (Guggenheim; unpublished).

Table B.12: (cont'd) XRD peaks observed for annite HK-NNO.

Angle (°2Θ)	d-spacing (Å)	Intensity (counts)	Peak designation	Comments
8.730	10.1288	480	Ann 001	
17.495	5.0690	19	Ann 002	
19.005	4.6696	26	Ann 020	
19.225	4.6166	23	Ann 110	
20.985	4.2332	17	Sa	
22.340	3.9794	15	Ann 111	
23.485	3.7880	25	Sa	
23.990	3.7093	28	Ann 11$\bar{2}$	
25.070	3.5519	30	Fa	
25.875	3.4432	45	Ann 022	
26.280	3.3911	132	Ann 003	
26.840	3.3216	37	Sa	
27.160	3.2832	14	Sa	
27.670	3.2238	34	Sa	
27.995	3.1871	42	Ann 112	
28.655	3.1152	14	Ann	Annite peak as observed by Eugster and Wones [38].
29.820	2.9961	14	Sa	
30.215	2.9578	31	Ann 11$\bar{3}$	
30.805	2.9025	9	Sa	
31.635	2.8282	34	Fa	
32.630	2.7442	14	Ann 023	
33.675	2.6614	154	Ann 200,13$\bar{1}$	
34.440	2.6040	10	Sa	
34.770	2.5801	14	Sa	
35.005	2.5633	34	Fa	
35.290	2.5432	31	Ann 004,131,20$\bar{2}$	
36.000	2.4947	29	Fa	
36.335	2.4725	96	Ann 201,13$\bar{2}$	
37.325	2.4091	11	Fa	
37.670	2.3878	7	(R)Ann 211,$\bar{1}$14	
38.505	2.3380	6	Ann 22$\bar{1}$	
39.235	2.2961	25	Ann 132,20$\bar{3}$	

(R) Tentative indice assigned, based on the unit cell refinement. This reflection was observed for a natural annite single crystal measurement (Guggenheim; unpublished).

Table B.13: XRD peaks observed for annite RB-25.

Angle (°2Θ)	d-spacing (Å)	Intensity (counts)	Peak designation	Comments
40.305	2.2376	4	?	
40.900	2.2064	45	Ann 202,13$\bar{3}$	
41.635	2.1692	4	Sa	
42.645	2.1201	3	(R)Ann 042	
43.705	2.0711	3	Sa	
44.500	2.0360	22	Ann 005	
46.040	1.9713	2	Sa	
46.915	1.9366	10	Ann 203,13$\bar{4}$	
50.865	1.7951	4	Sa	
51.380	1.7783	14	Fa	
54.040	1.6969	25	Ann 006,204,13$\bar{5}$	
54.880	1.6729	4	?	
56.100	1.6393	5	Ann 152,24$\bar{3}$	
57.375	1.6059	3	Ann 242,15$\bar{3}$	
58.050	1.5889	3	Fa	
59.195	1.5608	40	Ann 060,33$\bar{1}$	
59.940	1.5432	14	Ann 330,061,33$\bar{2}$	
60.815	1.5231	4	Fa	
61.150	1.5155	4	Fa	
61.875	1.4995	2	Fa	
62.265	1.4910	3	Ann 062,331	
63.985	1.4551	3	Ann 007	
65.865	1.4180	4	Ann 063,332,33$\bar{4}$	
67.835	1.3815	8	Ann 20$\bar{7}$	
68.330	1.3727	3	Ann 136	
69.825	1.3470	8	Ann 40$\bar{2}$,260	
70.060	1.3430	6	Fa	
70.780	1.3311	5	?	
71.545	1.3188	4	?	
73.390	1.2901	2	?Fa	
74.530	1.2732	2	?	
84.230	1.1495	2	?	
88.775	1.1021	1	?	
89.430	1.0957	1	?	

(R) Tentative indice assigned, based on the unit cell refinement. This reflection was observed for a natural annite single crystal measurement (Guggenheim; unpublished).

Table B.14: (cont'd) XRD peaks observed for annite RB-25.

Angle (°2Θ)	d-spacing (Å)	Intensity (counts)	Peak designation	Comments
8.735	10.1230	3181	Ann 001	
16.610	6.5060	0	?Sa	
15.150	5.8480	0	?Sa	
16.945	5.2323	19	?Fa	
17.480	5.0734	108	Ann 002	
18.960	4.6805	81	Ann 020	
19.240	4.6130	76	Ann 110	
19.840	4.4749	15	(R)Ann 012	
20.995	4.2312	67	Sa	
22.265	3.9927	61	Ann 111	
22.560	3.9411	27	Sa	
23.055	3.8576	6	Sa	
23.495	3.7863	100	Sa	
23.955	3.7147	128	Ann $11\bar{2}$	
24.555	3.6253	18	Sa	
25.060	3.5533	81	Fa	
25.880	3.4426	156	Ann 022	
26.290	3.3898	605	Ann 003	
26.805	3.3259	137	Sa	
27.145	3.2850	69	Sa	
27.395	3.2555	49	Sa	
27.665	3.2244	106	Sa	
27.970	3.1899	123	Ann 112	
28.670	3.1136	36	Ann	Annite peak as observed by Eugster and Wones [38].
29.170	3.0614	24	?	
29.830	2.9951	55	Sa	

(R) Tentative indice assigned, based on the unit cell refinement. This reflection was observed for a natural annite single crystal measurement (Guggenheim; unpublished).

Table B.15: XRD peaks observed for annite RB-7.

Angle (°2Θ)	d-spacing (Å)	Intensity (counts)	Peak designation	Comments
30.210	2.9583	90	Ann $11\bar{3}$	
30.775	2.9053	28	Sa	
31.635	2.8282	85	Fa	
32.600	2.7467	44	Ann 023	
33.655	2.6629	467	Ann $200,13\bar{1}$	
34.365	2.6095	38	Sa	
34.750	2.5815	42	Sa	
34.990	2.5643	58	Fa	
35.295	2.5429	110	Ann $004,131,20\bar{2}$	
35.910	2.5007	69	Fa	
36.330	2.4728	303	Ann $201,13\bar{2}$	
37.330	2.4088	21	Fa	
37.655	2.3888	28	(R)Ann $211,\bar{1}14$	
38.555	2.3350	28	Ann $22\bar{1}$	
39.190	2.2987	72	Ann $132,20\bar{3}$	
40.290	2.2384	15	?Sa	
40.880	2.2075	128	Ann $202,13\bar{3}$	
41.580	2.1719	20	Sa	
42.470	2.1284	20	?Sa	
42.775	2.1139	18	(R)Ann $042,\bar{1}41$	
43.735	2.0697	8	Fa	
44.750	2.0251	62	Ann $133,20\bar{4}$	
45.970	1.9742	7	?Fa	
46.900	1.9372	27	Ann $203,13\bar{4}$	
49.155	1.8535	8	?	
49.475	1.8422	6	Fa	
50.820	1.7966	14	Sa	
51.380	1.7783	32	Fa	
51.510	1.7741	34	Fa	
54.020	1.6975	67	Ann $006,204,13\bar{5}$	
54.890	1.6726	12	Ann $311,31\bar{3}$	

(R) Tentative indice assigned, based on the unit cell refinement. This reflection was observed for a natural annite single crystal measurement (Guggenheim; unpublished).

Table B.16: (cont'd) XRD peaks observed for annite RB-7.

Angle (°2Θ)	d-spacing (Å)	Intensity (counts)	Peak designation	Comments
56.090	1.6396	10	Ann 152,$24\bar{3}$	
56.565	1.6270	10	?Fa	
57.380	1.6058	9	Ann 242,$15\bar{3}$	
59.150	1.5619	112	Ann 060,$33\bar{1}$	
59.310	1.5581	76	Ann 135,$20\bar{6}$	
59.930	1.5434	45	Ann 330,061,$33\bar{2}$	
60.085	1.5398	21	Fa	
60.810	1.5232	7	Fa	
61.150	1.5155	10	Fa	
62.065	1.4954	34	Ann 062,331	
64.015	1.4544	10	Ann 007	
65.780	1.4196	9	Ann 063,332,$33\bar{4}$	
66.280	1.4101	6	Fa	
67.825	1.3817	25	Ann $20\bar{7}$,136	
68.325	1.3728	13	?	
69.795	1.3475	24	Ann 260,$40\bar{2}$	
70.715	1.3322	17	?	
71.400	1.3211	18	?	

Table B.17: (cont'd) XRD peaks observed for annite RB-7.

Angle (°2Θ)	d-spacing	Intensity	Peak designation	Comments
6.690	15.3408	2	?	
10.174	10.1738	10	Ann 001	
16.715	6.1583	1	?	
17.550	5.8674	1	Sa	
19.745	5.2206	1	?	
20.300	5.0793	1	Ann 002	
22.200	4.6494	2	Ann 020	
24.385	4.2382	3	Sa	
26.055	3.9708	3	Ann 111	
27.320	3.7903	4	Sa	
27.900	3.7130	4	Ann $11\bar{2}$	
28.595	3.6245	0.5	Sa	
29.170	3.5546	4	Fa,Sa	
30.050	3.4528	4	Ann 022	
30.615	3.3906	7	Ann 003	
31.230	3.3254	3	Sa	
31.600	3.2874	1	Sa	
32.185	3.2292	3	Sa	
32.630	3.1863	3	Ann 112	
34.765	2.9962	2	Sa	
35.230	2.9579	3	Ann $11\bar{3}$	
36.000	2.8966	1	Sa	
36.905	2.8280	4	Fa	
37.795	2.7511	2	Ann 023	
39.335	2.6596	9	Ann 200,$13\bar{1}$	
40.035	2.6149	1	Fa	
40.925	2.5604	3	An 004,131,$20\bar{2}$	
41.980	2.4989	4	Fa	
42.485	2.4705	8	Ann 201,$13\bar{2}$	
43.610	2.4098	1	Fa	
44.040	2.3874	1	(R)Ann 211,$\bar{1}14$	
45.025	2.3378	1	Ann $22\bar{1}$	

(R) Tentative indice assigned, based on the unit cell refinement. This reflection was observed for a natural annite single crystal measurement (Guggenheim; unpublished).

Table B.18: XRD peaks observed for annite RB-22. The intensities were estimated visually from the film produced by the Gandolfi camera.

Angle (°2Θ)	d-spacing (Å)	Intensity	Peak designation	Comments
45.775	2.3015	3	Ann $132,20\bar{3}$	
47.130	2.2389	0.5	?Sa	
47.915	2.2044	4	Ann $202,13\bar{3}$	
48.650	2.1730	1	?	
49.810	2.1256	1	(R)Ann $\bar{1}41,042$	
51.275	2.0688	0.5	Fa	
52.545	2.0222	3	Ann $133,20\bar{4}$	
53.835	1.9772	1	Fa	
55.140	1.9340	2	Ann $203,13\bar{4}$	
57.775	1.8529	1	?	
58.375	1.8355	1	Fa	
59.775	1.7963	2	Sa	
60.475	1.7775	4	Fa	
63.645	1.6976	4	Ann $006,204,13\bar{5}$	
64.595	1.6752	1	Ann $311,31\bar{3}$	
65.610	1.6522	1	Fa	
66.225	1.6385	1	Ann $152,24\bar{3}$	
66.770	1.6267	1	Fa	
67.765	1.6056	1	Ann $242,15\bar{3}$	
70.020	1.5602	8	Ann $060,135,33\bar{1},20\bar{6}$	
70.970	1.5420	2	Ann $330,061,33\bar{2}$	
72.155	1.5200	1	Fa	
73.740	1.4917	0.5	Ann 062,331	
75.805	1.4571	0.5	Ann 007	
77.230	1.4343	0.5	Fa	
78.200	1.4193	1	Ann $063,332,33\bar{4}$	
78.840	1.4096	1	Fa	
80.710	1.3824	2	Ann $20\bar{7},136$	
81.445	1.3720	1	Fa	
83.395	1.3456	2	Ann $40\bar{2},260$	
84.605	1.3299	2	?	
85.410	1.3198	2	?	

(R) Tentative indice assigned, based on the unit cell refinement. This reflection was observed for a natural annite single crystal measurement (Guggenheim; unpublished).

Table B.19: (cont'd) XRD peaks observed for annite RB-22. The intensities were estimated visually from the film produced by the Gandolfi camera.

References

[1] D.G. Rancourt. *Mössbauer Spectroscopy of Minerals. I. Inadequacy of Lorentzian-line Doublets in fitting Spectra Arising from Quadrupole Splitting Distributions.* Physics and Chemistry of Minerals. Vol.21, pp. 244–249, 1994.

[2] D.G. Rancourt. *Mössbauer Spectroscopy of Minerals. II. Problem of Resolving cis and trans Octahedral Fe^{2+} Sites.* Physics and Chemistry of Minerals. Vol. 21, pp.250–257, 1994.

[3] D.G. Rancourt, J.Y. Ping, and R.G. Berman. *Mössbauer Spectroscopy of Minerals. III. Octahedral-site Fe^{2+} Quadrupole Splitting Distributions in the Phlogopite-annite Series.* Physics and Chemistry of Minerals. Vol. 21, pp. 258–267, 1994.

[4] H.P. Eugster and D.R. Wones. *Stability of biotite: Experiment, theory and application.* Physics and Chemistry of Minerals. Vol. 50, pp. 1228–1272, 1965.

[5] A. Vértes, L. Korecz and K. Burger. *Mössbauer spectroscopy.* Studies in physical and theoretical chemistry. Vol. 5. Elsevier Scientific Publishing Company, 1979.

[6] R.V. Pound and G.A. Rebka. *Variation with temperature of the energy of recoil-free gamma-rays from solids.* Physical Review Letters. Vol. 4, pp. 274–275, 1960.

[7] B.D. Josephson. *Temperature dependent shift of γ-rays emitted by a solid.* Physical Review Letters. Vol. 4, p. 41, 1960.

[8] I.A.D. Christie. *The Magnetic Properties of Annite: a SQUID Magnetometry and* ^{57}Fe *Mössbauer Spectroscopy Study.* Ph.D. Thesis. University of Ottawa. Ottawa, Canada. 1994.

[9] *Mössbauer Effect Data Index 1989.* Ed. J.G.Stevens et al. 1989.

[10] N.N. Greenwood and T.C. Gibb. *Mössbauer Spectroscopy.* Chapman and Hall Ltd. 1971.

[11] P. Gütlich, R. Link and A. Trautwein. *Mössbauer Spectroscopy and Transition Metal Chemistry.* Inorganic Chemistry Concepts, vol. 3. Springer-Verlag, 1978.

[12] P.D. Tume. *A* ^{57}Fe *Mössbauer study on the thermal oxydation of iron in biotite mica.* M.Sc. Thesis. University of Ottawa. Ottawa, Canada. 1992.

[13] D.G. Rancourt and J.Y. Ping. *Voigt-based methods for arbitrary-shape static hyperfine parameter distributions in Mössbauer spectroscopy.* Nuclear Instruments and Methods in Physics Research. Vol. 8, pp. 85–97, 1991.

[14] D.G. Rancourt. *Accurate site populations from Mössbauer spectroscopy.* Nuclear Instruments and Methods in Physics Research. Vol. B44, pp. 199–210, 1989.

[15] M. Royer. *Site-specific* ^{57}Fe *Mössbauer recoilless fractions in true trioctahedral micas.* M.Sc. Thesis. University of Ottawa. Ottawa, Canada. 1991.

[16] D.G. Rancourt, I.A.D. Christie, M. Royer, H. Kodama, J.-L. Robert, A.E. Lalonde and E. Murad. *Determination of accurate* $^{[4]}Fe^{3+}$, $^{[6]}Fe^{3+}$, *and* $^{[6]}Fe^{2+}$ *site populations in synthetic annite by Mössbauer spectroscopy.* American Mineralogist. Vol. 79, pp. 51–62, 1994.

[17] R.M. Hazen and D.R. Wones. *The effect of cation substitutions on the physical properties of trioctahedral micas.* American Mineralogist. Vol. 57, pp. 103–129, 1972.

[18] R.D. Shannon. *Revised effective ionic radii and systemetic studies of interatomic distances in halides and chalcogenides.* Acta Crystallographica. Vol. A32, p. 751, 1976.

[19] J.F. Schairer and N.L. Bowen. *The system* $K_2O\text{-}Al_2O_3\text{-}SiO_2$. American Journal of Science. Vol. 253, pp. 681–746, 1955.

[20] D.L. Hamilton and C.M.B. Henderson. *The preparation of silicate compositions by gelling method.* Mineralogical Magazine. Vol. 36, pp. 832–838, 1968.

[21] H.P. Eugster and G.B. Skippen. *Igneous and metamorphic reactions involving gas equilibria,* in Researches in Geochemistry. P.H. Abelson (ed.). John Wiley and Sons, pp. 377–396, 1967.

[22] J.S. Huebner and M. Sato. *The oxygen fugacity–temperature relationships of manganese oxyde and nickel–nickel oxyde buffers.* American Mineralogist. Vol. 55, pp. 943–952, 1970.

[23] H.P. Eugster. *Heterogeneous reactions involving oxydation and reduction at high pressures and temperatures.* Journal of Chemical Physics. Vol. 26, pp. 1760–1761, 1957.

[24] I.-M. Chou and G.L. Cygan. *Quantitative redox control and measurements in hydrothermal experiments,* in Fluid-mineral interactions: a tribute to H.P. Eugster. J. Spencer and I.-M. Chou (ed.). The Geochemical Society, Special Publication no.2, pp. 3–15, 1990.

[25] D.G. Rancourt, A.M. McDonald, A.E. Lalonde and J.Y. Ping. *Mössbauer absorber thickness for accurate site populations in Fe-bearing minerals.* American Mineralogist. Vol. 78, pp. 1–7, 1993.

[26] W.H. Press, B.P. Flannery, S.A. Teukolsky and W.T. Vetterling. *Numerical Recipes.* Cambridge University Press. 1986.

[27] D.G. Rancourt, M.-Z. Dang and A.E. Lalonde. *Mössbauer spectroscopy of tetrahedral Fe^{3+} in trioctahedral micas.* American Mineralogist. Vol. 77, pp. 34–43, 1992.

[28] R.M. Hazen and L.W. Finger. *Comparative Crystal Chemistry.* Wiley. 1982.

[29] R.T. Downs. *Variations of bond lengths and volumes of silicate tetrahedra with temperature.* American Mineralogist. Vol. 77, pp. 751–757, 1992.

[30] F. James and M. Ross. *MINUIT — A system for function minimization and analysis of the parameter errors and correlations.* Computer Physics Communications. Vol. 10, pp. 343–367, 1975.

[31] D.G. Rancourt, P. Tume, and A.E. Lalonde. *Kinetics of the* $(Fe^{2+} + OH^{-})_{mica} \rightarrow (Fe^{3+} + O^{2-})_{mica} + H$ *Oxydation Reaction in Bulk Single-Crystal Biotite Studied by Mössbauer Spectroscopy.* Physics and Chemistry of Minerals. Vol.20, pp. 276–284, 1993.

[32] C.S. Hogg and R.E. Meads. *A Mössbauer study of thermal decomposition of biotites.* Mineralogical Magazine. Vol.40, pp. 79–88, 1975.

[33] G.J.R. Redhammer, E. Beran, E. Dachs, and G.Amthauer. *A Mössbauer and X-ray diffaction study of annites synthesized at different oxygen fugacities and crystal chemical implications.* Physics and Chemistry of Minerals. Vol.20, pp. 382–394, 1993.

[34] C.R. Rebbert, E. Partin, and D.A. Hewitt. *Synthetic biotite oxydation under hydrothermal conditions.* American Mineralogist. Vol. 80, pp. 345–354, 1995.

[35] A.E. Lalonde, D.G. Rancourt, and G.Y. Chao. *Fe-bearing trioctahedral micas from Mont Saint-Hilaire, Québec, Canada.* Mineralogical Magazine. Vol. 60, pp. 447–460, 1996.

[36] D.E. Appleman and H.T. Evans. *Indexing and leat-squares refinements of powder diffraction data.* US Geol Surv Comput Contrib 20.

[37] S.W. Bailey (ed.) *Micas.* Reviews in Mineralogy. Vol. 13. Mineralogical Society of America. 1984.

[38] H.P. Eugster and D.R. Wones. *Stability Relations of the Ferruginous Biotite, Annite.* Journal of Petrology. Vol. 3, pp. 82–125, 1962.